Title
An optogenetic investigation of the control and development of the spinal central pattern generator in zebrafish

Author
Warp, Erica Kirsten

Publication Date
2012

Peer reviewed|Thesis/dissertation

An optogenetic investigation of the control and development of the spinal central pattern generator in zebrafish

by

Erica Kirsten Warp

A dissertation submitted in partial satisfaction of the

requirements for the degree of

Doctor of Philosophy

in

Neuroscience

in the

Graduate Division

of the

University of California, Berkeley

Committee in Charge:

Professor Ehud Isacoff, Chair
Professor Mu-ming Poo
Associate Professor Marla Feller
Associate Professor Sharon Amacher

Spring 2012

An optogenetic investigation of the control and development of the spinal central pattern generator in zebrafish

By Erica Kirsten Warp

Abstract

An optogenetic investigation of the control and development of the spinal central pattern generator in zebrafish

by Erica Kirsten Warp

Doctor of Philosophy in Neuroscience

University of California, Berkeley

Professor Ehud Isacoff, Chair

The nervous system directly controls the muscles of the body, and thus, the behavior of the animal. An understanding of the neural circuits and cell types that mediate and control behavior would give us insight into the mechanisms by which the nervous system operates and would also contribute to the development of therapies and treatments for neurological disorders and diseases that result in locomotor deficits. Some behaviors are organized by constant voluntary drive, while others, which require regular and repeated patterns of activity, are organized by pattern generators. These central patterns generators (CPGs) include neural networks that generate the rhythmic patterns for basic behaviors like walking, swimming and breathing. Extensive research spanning decades in lamprey, *Xenopus* larvae, chick and mouse have provided great insight into the function and mechanisms of these circuits, but these models are poor for genetic studies or, in the case of the mouse, circuit complexity makes a cellular breakdown of the network challenging. As such, we know little about the specific cell types that are involved in the development and control of locomotor circuits. Using optogenetic tools, which allow for the manipulation and recording of neural activity with light in genetically-defined populations of cells, we investigated the cellular components that control the CPG in the spinal cord and the cells that mediate its proper formation during development. We applied these tools to the genetically-accessible and transparent zebrafish which permitted these studies in an intact and sometimes even behaving animal.

It was previously known that drivers exist in the brain that trigger the activation of the spinal CPG and induce behavior, but it was unknown whether similar such drivers exist in the spinal cord itself. To investigate spinal cell types that control the spinal CPG and mediate distinct behavioral programs, I, in collaboration with others, activated a variety of defined populations of spinal cord neurons and observed any consequent behavior. To activate neurons we targeted the light-gated ionotropic glutamate receptor LiGluR and targeted it to genetically-defined populations of cells in the zebrafish spinal cord using a variety of *Gal4* driver lines. Through these experiments we were able to identify a specific cell type, the Kolmer-Agduhr cerebrospinal-contacting interneuron,

which drives the CPG during forward swimming and whose function had been previously unknown. To investigate the development of the spinal CPG, I, in collaboration with others, used the genetically-encoded calcium indicator GCaMP to watch how patterns of neural activity evolve during development across the spinal cord and how this relates to the formation of a functional CPG. We found that early spontaneous neural activity progresses from sporadic to CPG-like rapidly in less than three hours, through the coalescence of local microcircuits. I next asked whether the early, uncorrelated activity is required for the acquisition of the later coordinated CPG-like activity. We applied the light-driven chloride pump Halorhodopsin to inhibit this early sporadic activity and found that activity is required for the proper integration of maturing neurons into the coordinated CPG network, which had not been known before. My work also included the application of the photoactivatable fluorophore *Dronpa* to the zebrafish and the identification of *Gal4* driver lines that have targeted cell type specific expression advantageous for studies of the spinal CPG, both of which advanced our ability to perform effective optogenetic studies of the spinal CPG circuitry, function and development.

Dedication

To my family and friends:
Thank you for your continued support.

Table of Contents

Acknowledgements

I have been supported by so many amazing and talented people during the course of my PhD.

I would first like to thank my advisor, Ehud Isacoff, for taking me into his lab and being an outstanding mentor throughout the last five years. Udi encouraged me to define my own ideas and research project in the early stages of my PhD and gave me the freedom that not all advisors would to explore techniques and topics that were particularly interesting to me. Though this freedom was certainly frightening at times, I thank him for his trust and support and for helping me grow this project from the ground up. His insights and suggestions were always spot on and I enjoyed our many discussions about the data and what it suggested and could not have asked for a better collaborator to write my paper with. Finally, Udi has been so supportive in my plans for the future of which I am very appreciative.

I would like to give a huge thank you to Claire Wyart. Claire was a post-doc in the Isacoff lab when I joined, started the zebrafish project in the lab, and was my collaborator on two projects for my dissertation and my day-to-day mentor. Claire taught me so much about how to do good science, but also how to be a strong woman in science. I will take many of her lessons with me and I know I will continue to use them throughout my life and career.

I also had the privilege of working closely with Gautam Agarwal, a graduate student in the Isacoff lab at the time, on the analysis for the spontaneous activity project. I could not have asked for a better partner on this and look forward to seeing what Gautam's work becomes in the future. The spontaneous activity project also involved working with three other graduate students in our lab - Drew Friedmann, Claire Oldfield, and Alden Conner – who were all such a joy to work with and whose hard work and creativity contributed significantly to the project.

I would like to thank other members of the Isacoff lab: Orapim Tulyathan who mentored me as a rotation student when I started in the lab, Sandra Wiese who keeps the lab running so smoothly, and Keely McDaniel who assisted me with many zebrafish experiments. I would like to also thank Holly Aaron who runs the Molecular Imaging Center at Berkeley and who has answered I bet 1000 questions of mine about microscopes. She has been invaluable to my lab work and has also been a great source of support for me during my PhD. The rest of the fish group – Carlos Pantoja, Elizabeth Carroll and Jessica Maxfield – as well as the other members of the Isacoff lab: it has been such a pleasure to work amidst such smart and dedicated and lovely people. You made coming to work every day an easy thing to do!

For several years, our lab worked very closely with Herwig Baier's lab at UCSF. I would like to thank Herwig for his invaluable mentoring and support of my project and other members of his lab such as Filippo Del Bene, Aristides Arrenberg, Wendy Staub,

Lindsey Mason and Karin Finger-Baier for teaching me so much about working with zebrafish and getting us on our feet as a zebrafish lab.

I would like to give a huge thanks to my thesis committee – Mu-ming Poo, Marla Feller, and Sharon Amacher – who have given me such great advice and encouragement over the years that we have worked together. My project certainly was made better by our many meetings and discussions. And I would like to thank Jack Gallant and Yang Dan for taking me on as a rotation student during my first year and giving me the opportunity to learn about such different areas in neuroscience. During my PhD, I also had the opportunity and privilege to be a Graduate Student Instructor for Professor Jeffery Winer and Professor Marian Diamond. I thank them both for being such strong role models for me in their love for teaching and the brain, and I speak for many when I say "Professor Winer, you have been dearly missed!"

I would like to thank John Ngai and Kati Markowitz and the rest of the neuroscience graduate students and neuroscience community at Berkeley for being such a great group of people to share ideas and time with and for creating such a vibrant and collaborative environment. I hope that we all stay in touch.

I would like to especially thank my parents Rick and Sherry Warp, my sister Lindsey Warp, her fiancé Joel Young, and my dear friends for being so supportive during this time. I could not have done it without you!

Finally, I cannot thank my husband Richard Warp enough. PhDs most certainly have their ups and downs and he has been there for each and every one of them. Rich has no doubt spent hundreds of hours listening to me talk about problems with the microscope software or how my data is not converging – always taking an interest and so often understanding all the science behind our conversations. He has been my emotional support as well as a platform to bounce ideas off of. I think he deserves an honorary PhD for his efforts. And I most certainly could not have done this without him.

Chapter 1:

Introduction: Applying optogenetic tools to an investigation of the development and control of locomotor circuits

The spinal central pattern generator: a building block for locomotion

Central pattern generators (CPGs) are neural networks that generate oscillatory output for rhythmic behaviors[1]. In the head, CPGs mediate rhythmicity for breathing, swallowing and chewing. In the spinal cord of vertebrates, the CPG produces rhythmic output for basic behaviors like walking and swimming, on top of which more complex behaviors are composed[2,3]. CPGs are, therefore, fundamental building blocks of the output of the nervous system and contribute to essential behaviors in animals. An understanding of the control and development of neural CPGs would, therefore, provide elementary insights into how the nervous system functions and organizes during maturation.

The spinal CPG of vertebrates, which mediates locomotion, is comprised of a network of neurons with the following relationships (Fig. 1): 1) there are inhibitory commissural neurons which mediate alternation between the two sides of the spinal cord, 2) there are descending excitatory interneurons that activate ipsilateral neurons and provide positive drive to maintain motion, and 3) in limbed animals, there are inhibitory connections between neuron pools that control opposing flexor and extensor muscles[4,1]. Much of what we have learned about the spinal CPG comes from a long history of investigation in the lamprey and *Xenopus* larvae[2,4]. Though we have gained great insights from these studies, lamprey and *Xenopus* are poor genetic models, and therefore, we know little about the specific cell types that control the spinal CPG or are involved in its development.

During locomotion, the spinal CPG is activated via excitatory input from neurons either in the brain or the spinal cord itself[5,6]. Some of these locomotor circuits have been well characterized. For example, in lamprey, teleost fish and amphibians, the large paired Mauthner cells in the hindbrain are activated by sensory circuits during the escape response, and provide di-synaptic excitation to motoneurons - via one descending glutamatergic interneuron – to initiate the fast escape response[7,8]. Knowledge of and accessibility to the specific cell types in this circuit have enabled studies revealing insights in processes such as plasticity[9], sensorimotor gating[10], and decision-making[11], leading to a better understanding of how locomotor circuits and neural circuits in general function. There is no doubt that there are novel cell types that drive the spinal CPG of which we are currently unaware. Identification of these cell types would lead to new insights into the control of behavior and how animals integrate sensory and experience-based information to choose specific behavioral programs. Investigations that allow the manipulation of defined cell types in the locomotor circuit as well as simultaneous analysis of behavior would allow researchers to identify circuit components that mediate particular behaviors.

The spinal CPG is a rather simple, but structured circuit – with inhibitory and excitatory relationships as described above. It is therefore an ideal network for a study of circuit development, as the circuit relationships are well-defined and can be assessed functionally through behavioral assays. The ontogeny of the spinal CPG during development has been studied extensively in rodent and chick models. In rodents, for

example, bursts of early neural activity are initially synchronized in ipsilateral and contralateral neurons[12,13], and begin to alternate between the left and right sides when $GABA_A$ and glycine receptors switch from hyperpolarizing to depolarizing later in development[12,14]. This coordination between cells on the same side of the cord and alternation between opposite sides of the cord is characteristic of the spinal CPG, suggesting its basic circuit is formed by this time. It is unknown, however, how early neural activity, which at this stage in development is spontaneous and does not require excitatory sensory input, influences the maturation of this circuit. There is evidence that correlated patterns of spontaneous activity in the spinal cord are necessary for proper axon guidance[15,16], for establishing a balance between excitatory and inhibitory synaptic strength[17], and for setting up coordinated alternation between the two sides of the cord[18]. It is not known, however, if early neural activity is required for the establishment of ipsilateral synchronization and which cell types may mediate this activity-dependent process. Studies that allow recording and manipulation of neural activity in defined cell types would help to elucidate these outstanding questions.

Optogenetics: genetic tools for monitoring and manipulating neurons with light

Recent technological advances in genetics, optics and chemistry have brought forward a variety of genetically-encoded light-based tools ("optogenetic" tools) to monitor and manipulate the activity of neurons in genetically-defined populations of cells[19–21]. Applying these new tools to a study of the spinal CPG would help uncover novel mechanisms of behavioral control and nervous system development that were previously inaccessible with more traditional experimental methods.

Optogenetic tools to manipulate neural activity allow the remote activation or inhibition of neural activity with light. One approach to developing these tools has been to exploit naturally-occurring proteins with endogenous light sensitivity such as the Rhodopsins, which utilize the photo-sensitive element retinal. For example, the light-activated cation channel Channelrhodopsin2 (ChR2), endogenous to green algae, opens with the absorption of 480 nm light, resulting in an influx of cations and subsequent depolarization of the cell it is expressed in[22,23]. In contrast, the light-driven chloride pump Halorhodopsin (NpHR) from archaea uses the energy in yellow light (590 nm) to pump negative chloride ions into the cell, thus causing hyperpolarization and decreasing neural firing[24]. By exogenously expressing these microbial opsins in neurons, researchers can remotely activate or inhibit ChR2- or NpHR-expressing neurons with light. An alternative approach has been to engineer proteins endogenous to neurons to gain light-sensitivity. For example, the light-gated ionotropic glutamate receptor LiGLuR is an endogenous glutamate receptor that contains an added cysteine on its extracellular domain which allows the attachment of a synthetic photoswitch containing the ligand glutamate[25,26]. The spectral properties of the photoswitch and its location of attachment to the channel results in the channel opening in response to UV light and closing in response to blue light, thus allowing for the remote control of cation currents in the neurons in which it is expressed[25,26]. Endowing light sensitivity to hyperpolarizing potassium channels has been accomplished through similar approaches[27,28].

These genetically-encoded light-based tools provide advantages over more traditional experimental methods such as pharmacology and electrophysiology. Genetically-defined cell types can be isolated by restricted expression of the transgene allowing the manipulation of activity in defined populations. This contrasts with global application of pharmacological agents which affects all cell types that express drug-sensitive receptors, and electrical stimulation in which all cells in the local area of the electrode are influenced. Activating light can also be applied at desired time points with millisecond precision, allowing for finer temporal control than is acquired through the perfusion and wash-pout of pharmacological agents, especially in dense tissue preparations. Light can also be targeted spatially using tools such as digital micro-mirror devices to provide further cell specificity above genetic targeting. Large populations however can be reached with global illumination, providing fine temporal control of activity in specific cell types that can only be achieved using electrophysiology in single cells.

Genetically-encoded indicators to monitor neural activity have also been developed. Calcium indicators such as GCaMP[29,30], which is based on a circularly permutated version of GFP, and Cameleon, a FRET-based probe[31], have calcium binding motifs and increase in brightness or FRET, respectively, when bound to calcium. Since calcium enters neurons through voltage-gated calcium channels opened during cell depolarization, the measurement of calcium is an effective measurement of neural activity. Voltage changes during neural activity can also be directly measured with voltage-sensitive probes such as Mermaid[32] and Arch(D95N)[33] that utilize voltage-sensitive components in naturally occurring membrane proteins. These dynamic measurements of cell activity can be coupled with the imaging of cell morphology in the same or other genetically-defined populations of cells. Fluorophores that cover the visual spectrum such as green fluorescent protein (GFP) and red mCherry provide static information on cell morphology and circuit anatomy[34]. Photoswitchable probes such as Kaede and Dronpa change their spectral properties with the application of certain wavelengths of light, providing additional advantages in anatomical analysis. Kaede converts from red to green with UV light, allowing for color flexibility and permitting cell tracking and cell separation experiments[35]. Dronpa increases and decreases its spectral emission with light, allowing for better separation of the relevant signal from the background[36].

These genetically-encoded indicators of neural activity provide advantages over other methods to measure neural activity such as electrophysiology and dye imaging. Whole cell recordings provide high resolution information on electrical activity but the number of cells that can be recorded simultaneously is limited. Multi-unit electrode arrays allow the recording of larger populations of cells but the electrodes record from all local cells regardless of their identity, making it difficult to define cell-type specific properties. Functional imaging allows for simultaneous recording of large populations of cells, though at the sacrifice of temporal resolution. Imaging with genetically-encoded probes rather than injected dyes, however, allows for population imaging in genetically-defined

cell types, providing a means to record from populations of neurons while maintaining cell identity.

Zebrafish: an ideal model for an optogenetic dissection of locomotor circuits

Zebrafish have become a popular model for optogenetic studies of locomotion, due to several advantages. They have a simple and well-characterized spinal cord. They are transparent when they are embryos and larvae, and are genetically-accessible to exogenous expression of optogenetic tools. Additionally, they have a diverse yet limited repertoire of behaviors, which allows for the study of circuits that mediate discrete locomotor programs.

Locomotor behavior in the zebrafish starts in the embryo at 17 hours post fertilization (hpf) and consists of spontaneous coiling, or slow side-to-side movements of the tail[37], and is associated with spontaneous activity in neurons of the ventral spinal cord[38,39]. This spontaneous behavior peaks in frequency at 19 hpf and is largely absent by 30 hpf. By 21 hpf, zebrafish embryos respond to touch with an escape response[38,40]. Pharmacological and electrophysiology studies have suggested that the acquisition of this sensory-evoked behavior is associated with the formation of a network mediated by chemical synapses, whereas spontaneous coiling relies heavily on electrical synapses[38,39,40]. By 21 hpf, reticulospinal neurons, including the large Mauthner cell, have begun to extend axons caudally into the spinal cord[41], and indeed the hindbrain is required for a strong escape response[37].

Starting at 28 hpf, zebrafish begin to exhibit low-frequency spontaneous forward swimming, which also depends on circuits mediated by chemical synapses[37]. Between 2 and 3 days post-fertilization (dpf), after hatching, zebrafish larvae exhibit high frequency long duration bouts of swimming, indicating a strengthening of the associated chemical network during this time[42,43]. By 4 dpf, swimming has a “beat and glide” kinematic and bouts are shorter with pauses in between and more directed than at earlier stages[42,43]. By 5-6 dpf, zebrafish larvae can perform more complex behaviors including prey tracking and capture[44,45], which requires the tracking of visual objects and sensorimotor integration. This repertoire of behaviors can be studied in individual animals whose head is fixed in agarose to acquire high resolution movies of body kinematics and to possibly associate with imaging or targeted light activation. High throughput behavior studies can also be performed easily in the zebrafish and have been used successfully for the screening of pharmacological[46,47] and biological[48,49] agents that affect behavior.

Behaviors in the zebrafish are initiated by supraspinal or spinal inputs and trigger the CPG located in the spinal cord. The spinal CPG then produces rhythmic output through the motoneurons which mediates the oscillations of the tail and pectoral fins necessary for swimming. The zebrafish spinal cord is a simple and well-characterized network, which makes a cellular investigation of the spinal CPG more tractable compared to higher vertebrates[21]. By 20 hpf, when the network is already spontaneously active and

there is spontaneous coiling, only 5 types of early-born neurons have begun to extend axons in the zebrafish spinal cord: Rohon Beard cells, commissural primary ascending (CoPA) interneurons, ipsilateral caudal (IC) interneurons, ventral lateral descending (VeLD) interneurons, and primary motoneurons (PMNs) (Fig. 2A)[50–52]. Since spontaneous activity is confined to the ventral, motor-associated part of the spinal cord in the zebrafish, only the last four of these are spontaneously active at this time[38,39]. Rohon Beard cells are the primary somatosensory cell of the spinal cord in the embryo and larvae (replaced by dorsal root ganglion cells later in development) and extend afferent processes to the surface of the skin. Their cell bodies reside in the most dorsal part of the spinal cord[50]. CoPA interneurons are glutamaturgic, with large cell bodies and axons that project ventrally and then ascend contralaterally in the dorsal longitudinal fasciculus (DLF)[50,53,54]. IC interneurons are small-bodied glutamaturgic neurons with descending ipsilateral axons and reside in the caudal hindbrain and the first six segments of the spinal cord[41]. VeLDs are also glutamaturgic with descending ipsilateral axons, but are restricted to the spinal cord and have larger, more dorsal cell bodies than the ICs[50,53]. There are three to four PMNs per hemisegment which extend their axons out of the cord to the muscle[52,55]. They are early-born, large and with thick axons and contrast with the more numerous (approximately 20 per hemisegment) and small, late-born secondary motoneurons (SMNs)[52,55,56].

By 24 hpf, six additional interneurons have extended their axons (Fig. 2B). These include GABAergic dorsolateral ascending (DoLA) interneurons that reside in the dorsal cord and rostrally extend ipsilateral axons in the DLF[50,53]. More ventrally are the glutamaturgic circumferential descending (CiD) interneurons which have large cell bodies and extend axons ventrally and then caudally in the DLF[50,54]. Circumferential ascending (CiA) interneurons also extend axons ipsilaterally, but ascend and are glycinergic[50,54]. There are two types of contralateral interneurons that extend axons at this time: the commissural secondary (CoSA) and commissural bifurcating (CoB) interneurons[50,54]. The former follows the same axonal path as its primary homologue the CoPAs, but the CoSAs are smaller and consist of both glutamaturgic and glycinergic populations. CoBs are glycinergic with axons that both ascending and descend in the contralateral cord. Finally, GABAergic Kolmer-Agduhr interneurons sit in the ventral cord and have ciliated processes that contact the cerebral spinal fluid in the central canal[57]. By 27 hpf, SMNs also begin to grow axons which extend out of the cord[52].

Morphological studies have revealed the presence of a few additional interneurons in the 5 dpf larvae (Fig. 2C). These include the large commissural longitudinal ascending (CoLA) interneurons with ascending contralateral axons, and three types of descending interneurons: multipolar commissural descending (MCoD), unipolar commissural descending (UCoD), and ventral medial (VeMe) interneurons[54]. MCoDs and UCoDs have cell bodies in the middle of the cord with axons that descending on the contralateral side, whereas VeMes reside at the ventral boder of the cord and extend axons ipsilaterally[54].

Zebrafish are amenable to genetic manipulations and these defined cell types can be targeted genetically with specific promoters or enhancer-trapped driver lines to allow the

expression of exogenous genes such as those for genetically-encoded indicators of activity or light-gated or light driven channels and pumps. For example, lines utilizing the known promoter *Hb9* target motoneurons and VeLD neurons in the spinal cord[58] whereas lines using the *glycine transporter-2* promoter target glycinergic interneurons[59]. Numerous labs have also generated *Gal4* driver lines using enhancer trapping which are useful when known promoters are not available[60–62]. The *Gal4,UAS* system is a genetic system from yeast in which a gene of interest (such as that for GCaMP) is cloned behind the upstream activating sequence (*UAS*)[63]. *UAS* is only activated when *Gal4,* which is not endogenous to zebrafish, is present in the cell. *Gal4* driver lines can be created through enhancer trapping in which constructs for the *Gal4* gene are injected into fertilized eggs and integrate randomly in the genome[60,64]. Depending on which promoters and enhancers the *Gal4* falls near, *Gal4* will be expressed in genetically-defined populations of cells. When mated with stable lines of *UAS:geneX* fish, progeny will express the gene of interest in the defined population of cells (Fig. 3).

In summary, zebrafish have a defined but varied set of behaviors, a simple and well-characterized spinal cord, and are genetically accessible. They are also transparent when they are embryos and larvae which make them an optimal model for optogenetic tools as no surgical manipulations are necessary for the application of light and genetic targeting of the transgene is simple using the *UAS,Gal4* system[21]. Zebrafish also develop rapidly and so are an ideal model for developmental studies of the locomotor system. Taking advantage of these characteristics of young zebrafish and applying optogenetic tools, it is possible monitor neural activity, manipulate this activity and assay behavior non-invasively all in the same animal and even at the same time.

Thesis summary

Here I have applied optogenetic techniques to the zebrafish *in vivo* to investigate the cellular basis of control of the spinal CPG and its development in the embryo. This study involved two technical components: 1) I demonstrated that the photo-switchable fluorophore Dronpa could be applied *in vivo* in zebrafish to improve fluorescent imaging of genetically-targeted cells **(Chapter 2)**, and 2) I morphologically screened over 30 *Gal4* enhancer trap lines targeting cells in the spinal cord and identified driver lines useful for investigations of the spinal CPG **(Chapter 3)**. One of these *Gal4* lines was identified as targeting cerebral spinal fluid-contacting Kolmer-Agduhr (KA) neurons whose function was previously unknown. Activating these cells with the light-gated glutamate receptor LiGluR in behavioral studies revealed that these cells provide positive drive to the spinal CPG for forward swimming **(Chapter 4)**, which was previously unknown. I next investigated how the spinal CPG forms in the embryo. Targeting the genetically-encoded calcium indicator GCaMP to other spinal neurons - motoneurons and ventral longitudinal descending interneurons (VeLDs) - using another *Gal4* line, I – in collaboration with others – found that spontaneous activity in these cells transitions from sporadic to locomotor-like activity rapidly in less than three hours. Inhibiting early sporadic activity with the light-driven chloride pump Halorhodopsin

impeded the integration of maturing neurons into the coordinated network, revealing that the formation of the first CPG-like patterns depends on the sporadic activity that precedes it **(Chapter 5)**.

Figure 1

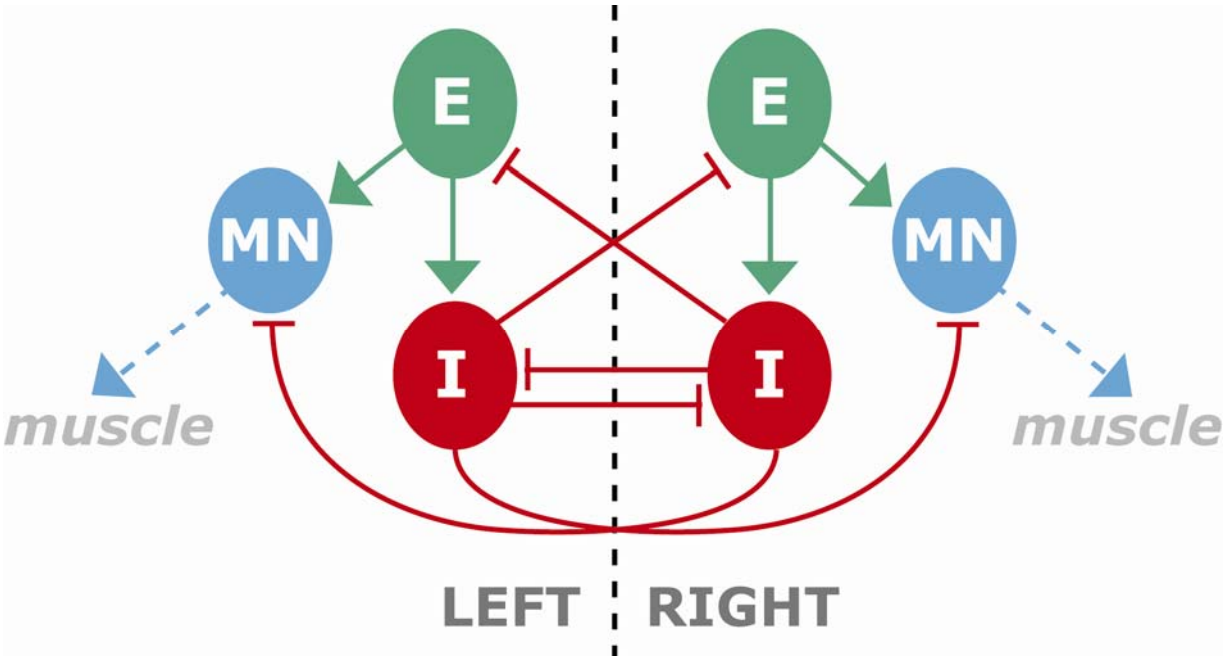

Figure 1. The circuit of the spinal central pattern generator (CPG) consists of stereotyped excitatory and inhibitory components. Diagram of a simplified CPG circuit showing groups of excitatory (E) and inhibitory (I) interneurons and pools of motoneurons (MN) that are the final output of the CPG to the muscle cells. Inhibitory synapses are indicated with a "T" shape and excitatory synapses with an arrow. Dotted line indicates the midline of the spinal cord. Adapted from Grillner, *Neuron*, 2006.

Figure 2

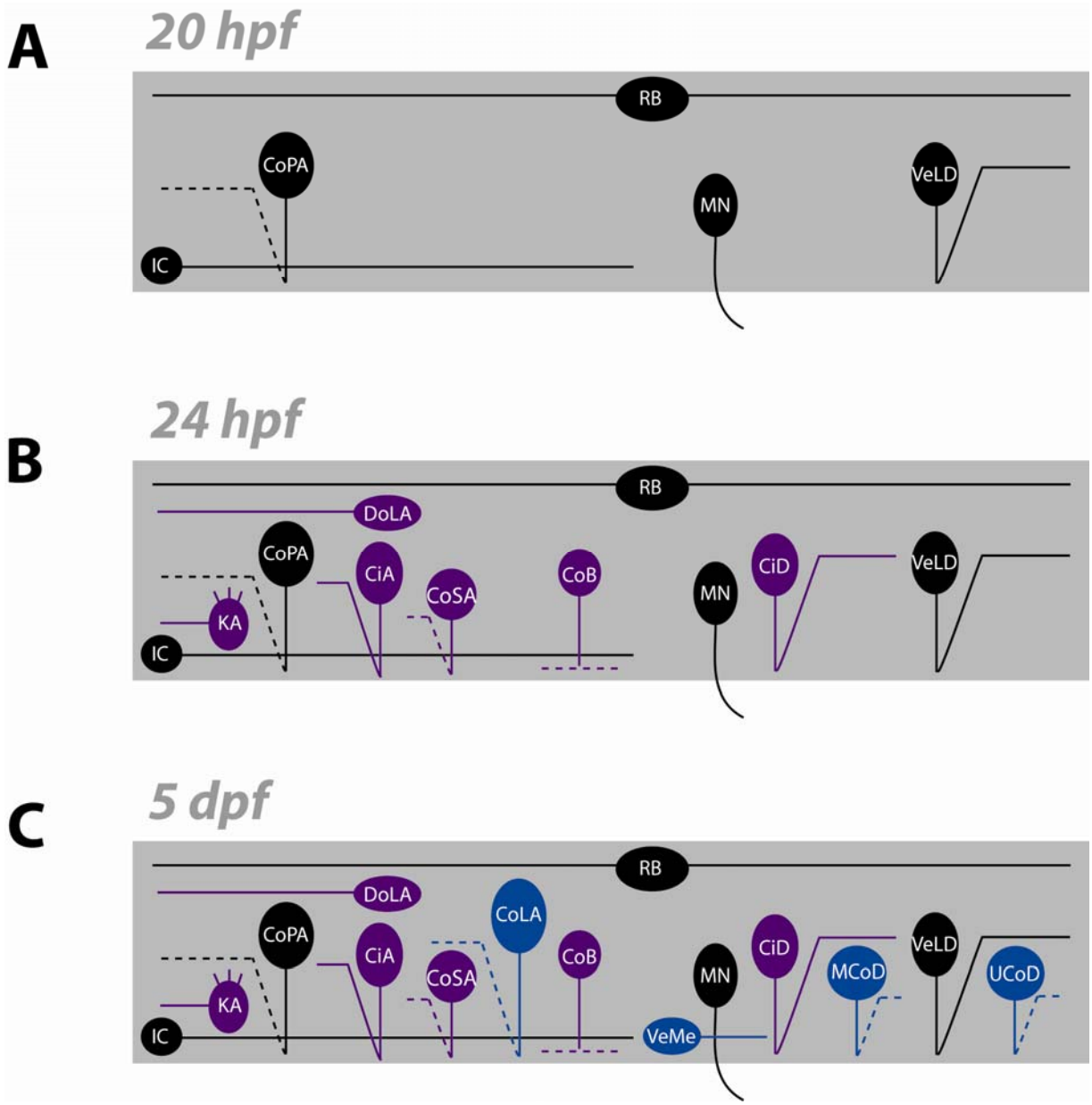
A
20 hpf
RB
CoPA
IC
MN
VeLD
B
24 hpf
RB
DoLA
CoPA
CiA
CoSA
CoB
KA
IC
MN
CiD
VeLD
C
5 dpf
RB
DoLA
CoLA
CoPA
CiA
CoSA
CoB
KA
IC
VeMe
MN
CiD
MCoD
VeLD
UCoD

Figure 2. Cells of the embryonic and larval zebrafish spinal cord extend axons at different periods of development. Diagram of the cell types that have begun to extend axons in the zebrafish spinal cord (gray box) by 20 hpf (A, *black*), 24 hpf (B, *purple*) and 5 dpf (C, *blue*). At 20 hpf (A), only five cells types have undergone axogenesis: the Rohon Beard cells (RB), ipsilateral caudal (IC) interneurons, ventral longitudinal descending (VeLD) and commissural primary ascending interneurons, and primary motoneurons (MNs) whose axons leave the cord. By 24 hpf (B), six more interneurons have extended axons: dorsal lateral ascending (DoLA), circumferential descending (CiD), circumferential ascending (CiA), commissural bifurcating (CoB), commissural secondary ascending (CoSA) and Kolmer-Agduhr interneurons. At 5 dpf (C), four additional cell types have also been observed: commissural longitudinal ascending (CoLA), multipolar commissural descending (MCoD), unipolar commissural descending (UCoD), and ventral medial interneurons. Dotted lines indicate axons that cross the midline of the spinal cord. The rostral direction is to the left. Adapted from Saint-Amant, *Zebrafish*, 2006.

Figure 3

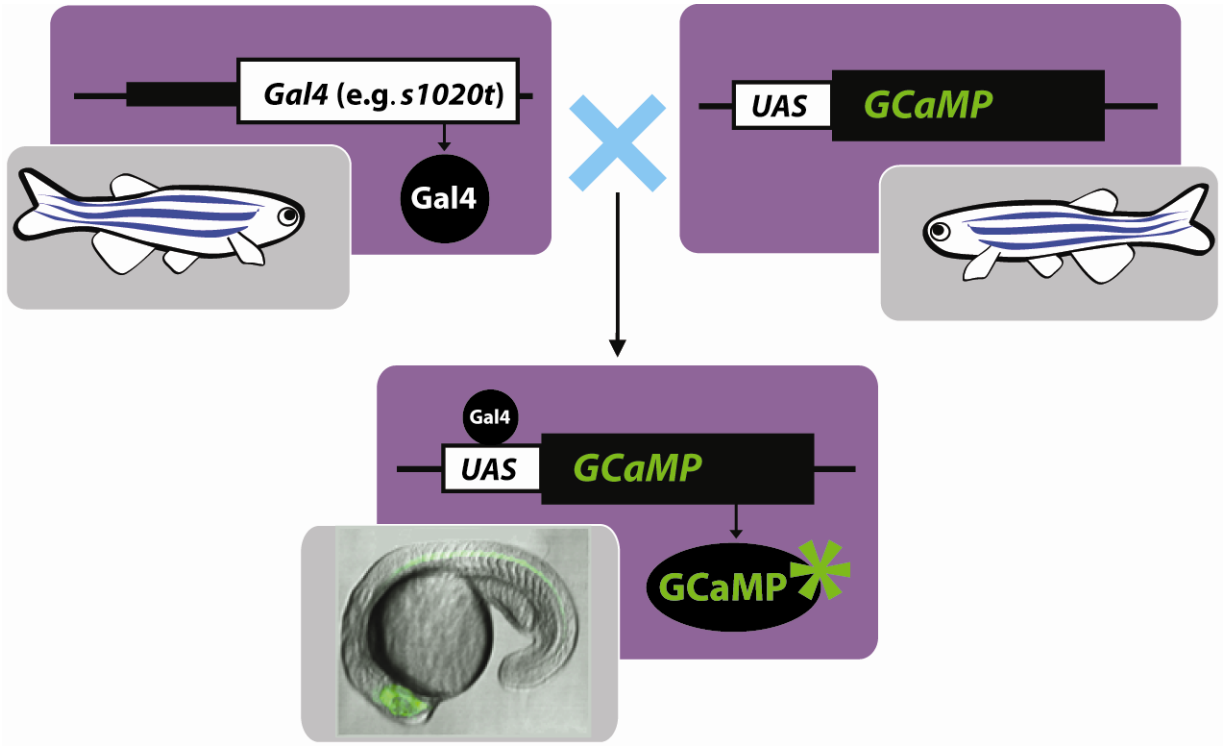

Figure 3. The *UAS,Gal4* system allows for targeted expression of an exogenous gene of interest in a population of cells defined by a driver line. *Gal4* driver lines (*top left*) such as *Gal4*^{s1020t}, are created through enhancer trapping or by controlling *Gal4* expression with known promoters and results in *Gal4* being expressed in the targeted population of cells. *UAS* lines (*top right*) are also created in which *UAS* drives the expression of a transgene such as *GCaMP*. The transgene, however, is not expresses in these fish that lack *Gal4.* Progeny of these fish, however, that carry the gene for *Gal4* and *UAS* will express the trangene in the cellular population targeted with *Gal4* as only these cells express the *UAS*-activating *Gal4* transcription factor. Adapted from Heberlein et al., *Integr. Comp. Biol.*, 2004.

REFERENCES

1. Grillner, S. Biological pattern generation: the cellular and computational logic of networks in motion. *Neuron* **52**, 751-766 (2006).

2. Grillner, S. The motor infrastructure: from ion channels to neuronal networks. *Nat Rev Neurosci* **4**, 573-586 (2003).

3. Selverston, A. I. A Neural Infrastructure for Rhythmic Motor Patterns. *Cellular and Molecular Neurobiology* **25**, 223-244 (2005).

4. Roberts, A., Soffe, S. R., Wolf, E. S., Yoshida, M. & Zhao, F. Y. Central circuits controlling locomotion in young frog tadpoles. *Ann. N. Y. Acad. Sci.* **860**, 19-34 (1998).

5. Fenaux, F., Corio, M., Palisses, R. & Viala, D. Effects of an NMDA-receptor antagonist, MK-801, on central locomotor programming in the rabbit. *Exp Brain Res* **86**, 393-401 (1991).

6. Kiehn, O. *et al.* Excitatory components of the mammalian locomotor CPG. *Brain Res Rev* **57**, 56-63 (2008).

7. Zottoli, S. J. Correlation of the startle reflex and Mauthner cell auditory responses in unrestrained goldfish. *J. Exp. Biol.* **66**, 243-254 (1977).

8. Fetcho, J. R. & Faber, D. S. Identification of motoneurons and interneurons in the spinal network for escapes initiated by the mauthner cell in goldfish. *J. Neurosci* **8**, 4192-4213 (1988).

9. Charpier, S., Behrends, J. C., Chang, Y. T., Sur, C. & Korn, H. Synchronous bursting in a subset of interneurons inhibitory to the goldfish Mauthner cell: synaptic mediation and plasticity. *J. Neurophysiol.* **72**, 531-541 (1994).

10. Preuss, T., Osei-Bonsu, P. E., Weiss, S. A., Wang, C. & Faber, D. S. Neural representation of object approach in a decision-making motor circuit. *J. Neurosci.* **26**, 3454-3464 (2006).

11. Neumeister, H., Szabo, T. M. & Preuss, T. Behavioral and physiological characterization of sensorimotor gating in the goldfish startle response. *J. Neurophysiol.* **99**, 1493-1502 (2008).

12. Nakayama, K., Nishimaru, H. & Kudo, N. Basis of changes in left-right coordination of rhythmic motor activity during development in the rat spinal cord. *J. Neurosci* **22**, 10388-10398 (2002).

13. Hanson, M. G. & Landmesser, L. T. Characterization of the circuits that generate spontaneous episodes of activity in the early embryonic mouse spinal cord. *J. Neurosci* **23**, 587-600 (2003).

14. Bonnot, A., Whelan, P. J., Mentis, G. Z. & O'Donovan, M. J. Spatiotemporal pattern of motoneuron activation in the rostral lumbar and the sacral segments during locomotor-like activity in the neonatal mouse spinal cord. *J. Neurosci* **22**, RC203 (2002).

15. Hanson, M. G. & Landmesser, L. T. Normal patterns of spontaneous activity are required for correct motor axon guidance and the expression of specific guidance molecules. *Neuron* **43**, 687-701 (2004).

16. Menelaou, E. *et al.* Embryonic motor activity and implications for regulating motoneuron axonal pathfinding in zebrafish. *Eur. J. Neurosci* **28**, 1080-1096 (2008).

17. Gonzalez-Islas, C. & Wenner, P. Spontaneous network activity in the embryonic spinal cord regulates AMPAergic and GABAergic synaptic strength. *Neuron* **49**, 563-575 (2006).

18. Myers, C. P. *et al.* Cholinergic input is required during embryonic development to mediate proper assembly of spinal locomotor circuits. *Neuron* **46**, 37-49 (2005).

19. Herlitze, S. & Landmesser, L. T. New optical tools for controlling neuronal activity. *Curr. Opin. Neurobiol* **17**, 87-94 (2007).

20. Szobota, S. & Isacoff, E. Y. Optical control of neuronal activity. *Annu Rev Biophys* **39**, 329-348 (2010).

21. Fetcho, J. R., Higashijima, S. & McLean, D. L. Zebrafish and motor control over the last decade. *Brain Res Rev* **57**, 86-93 (2008).

22. Boyden, E. S., Zhang, F., Bamberg, E., Nagel, G. & Deisseroth, K. Millisecond-timescale, genetically targeted optical control of neural activity. *Nat. Neurosci* **8**, 1263-1268 (2005).

23. Zhang, F., Wang, L.-P., Boyden, E. S. & Deisseroth, K. Channelrhodopsin-2 and optical control of excitable cells. *Nat. Methods* **3**, 785-792 (2006).

24. Zhang, F. *et al.* Multimodal fast optical interrogation of neural circuitry. *Nature* **446**, 633-639 (2007).

25. Volgraf, M. *et al.* Allosteric control of an ionotropic glutamate receptor with an optical switch. *Nat. Chem. Biol* **2**, 47-52 (2006).

26. Szobota, S. *et al.* Remote control of neuronal activity with a light-gated glutamate receptor. *Neuron* **54**, 535-545 (2007).

27. Banghart, M., Borges, K., Isacoff, E., Trauner, D. & Kramer, R. H. Light-activated ion channels for remote control of neuronal firing. *Nat. Neurosci* **7**, 1381-1386 (2004).

28. Janovjak, H., Szobota, S., Wyart, C., Trauner, D. & Isacoff, E. Y. A light-gated, potassium-selective glutamate receptor for the optical inhibition of neuronal firing. *Nat. Neurosci.* **13**, 1027-1032 (2010).

29. Nakai, J., Ohkura, M. & Imoto, K. A high signal-to-noise Ca(2+) probe composed of a single green fluorescent protein. *Nat. Biotechnol* **19**, 137-141 (2001).

30. Tian, L. *et al.* Imaging neural activity in worms, flies and mice with improved GCaMP calcium indicators. *Nat. Methods* **6**, 875-881 (2009).

31. Miyawaki, A. *et al.* Fluorescent indicators for Ca2+ based on green fluorescent proteins and calmodulin. *Nature* **388**, 882-887 (1997).

32. Tsutsui, H., Karasawa, S., Okamura, Y. & Miyawaki, A. Improving membrane voltage measurements using FRET with new fluorescent proteins. *Nat. Methods* **5**, 683-685 (2008).

33. Kralj, J. M., Douglass, A. D., Hochbaum, D. R., Maclaurin, D. & Cohen, A. E. Optical recording of action potentials in mammalian neurons using a microbial rhodopsin. *Nat. Methods* **9**, 90-95 (2011).

34. Chudakov, D. M., Lukyanov, S. & Lukyanov, K. A. Fluorescent proteins as a toolkit for in vivo imaging. *Trends Biotechnol.* **23**, 605-613 (2005).

35. Ando, R., Hama, H., Yamamoto-Hino, M., Mizuno, H. & Miyawaki, A. An optical marker based on the UV-induced green-to-red photoconversion of a fluorescent protein. *Proc. Natl. Acad. Sci. U.S.A.* **99**, 12651-12656 (2002).

36. Habuchi, S. *et al.* Reversible single-molecule photoswitching in the GFP-like fluorescent protein Dronpa. *Proc. Natl. Acad. Sci. U.S.A.* **102**, 9511-9516 (2005).

37. Saint-Amant, L. & Drapeau, P. Time course of the development of motor behaviors in the zebrafish embryo. *J. Neurobiol* **37**, 622-632 (1998).

38. Saint-Amant, L. & Drapeau, P. Motoneuron activity patterns related to the earliest behavior of the zebrafish embryo. *J. Neurosci* **20**, 3964-3972 (2000).

39. Saint-Amant, L. & Drapeau, P. Synchronization of an embryonic network of identified spinal interneurons solely by electrical coupling. *Neuron* **31**, 1035-1046 (2001).

40. Drapeau, P. *et al.* Development of the locomotor network in zebrafish. *Prog. Neurobiol* **68**, 85-111 (2002).

41. Mendelson, B. Development of reticulospinal neurons of the zebrafish. II. Early axonal outgrowth and cell body position. *J. Comp. Neurol* **251**, 172-184 (1986).

42. Buss, R. R. & Drapeau, P. Synaptic drive to motoneurons during fictive swimming in the developing zebrafish. *J. Neurophysiol* **86**, 197-210 (2001).

43. Müller, U. K. & van Leeuwen, J. L. Swimming of larval zebrafish: ontogeny of body waves and implications for locomotory development. *J. Exp. Biol.* **207**, 853-868 (2004).

44. Kimmel, C. B., Ballard, W. W., Kimmel, S. R., Ullmann, B. & Schilling, T. F. Stages of embryonic development of the zebrafish. *Dev. Dyn* **203**, 253-310 (1995).

45. Borla, M. A., Palecek, B., Budick, S. & O'Malley, D. M. Prey capture by larval zebrafish: evidence for fine axial motor control. *Brain Behav. Evol.* **60**, 207-229 (2002).

46. Kokel, D. *et al.* Rapid behavior-based identification of neuroactive small molecules in the zebrafish. *Nat. Chem. Biol.* **6**, 231-237 (2010).

47. Rihel, J. *et al.* Zebrafish behavioral profiling links drugs to biological targets and rest/wake regulation. *Science* **327**, 348-351 (2010).

48. Burgess, H. A. & Granato, M. Sensorimotor Gating in Larval Zebrafish. *The Journal of Neuroscience* **27**, 4984 -4994 (2007).

49. Prober, D. A., Rihel, J., Onah, A. A., Sung, R.-J. & Schier, A. F. Hypocretin/Orexin Overexpression Induces An Insomnia-Like Phenotype in Zebrafish. *The Journal of Neuroscience* **26**, 13400 -13410 (2006).

50. Bernhardt, R. R., Chitnis, A. B., Lindamer, L. & Kuwada, J. Y. Identification of spinal neurons in the embryonic and larval zebrafish. *J. Comp. Neurol* **302**, 603-616 (1990).

51. Kuwada, J. Y., Bernhardt, R. R. & Nguyen, N. Development of spinal neurons and tracts in the zebrafish embryo. *J. Comp. Neurol* **302**, 617-628 (1990).

52. Myers, P. Z., Eisen, J. S. & Westerfield, M. Development and axonal outgrowth of identified motoneurons in the zebrafish. *J. Neurosci* **6**, 2278-2289 (1986).

53. Higashijima, S.-I., Mandel, G. & Fetcho, J. R. Distribution of prospective glutamatergic, glycinergic, and GABAergic neurons in embryonic and larval zebrafish. *J. Comp. Neurol* **480**, 1-18 (2004).

54. Hale, M. E., Ritter, D. A. & Fetcho, J. R. A confocal study of spinal interneurons in living larval zebrafish. *J. Comp. Neurol* **437**, 1-16 (2001).

55. Westerfield, M., McMurray, J. V. & Eisen, J. S. Identified motoneurons and their innervation of axial muscles in the zebrafish. *J. Neurosci.* **6**, 2267-2277 (1986).

56. Liu, D. W. & Westerfield, M. Function of identified motoneurones and co-ordination of primary and secondary motor systems during zebra fish swimming. *J. Physiol. (Lond.)* **403**, 73-89 (1988).

57. Bernhardt, R. R., Patel, C. K., Wilson, S. W. & Kuwada, J. Y. Axonal trajectories and distribution of GABAergic spinal neurons in wildtype and mutant zebrafish lacking floor plate cells. *J. Comp. Neurol* **326**, 263-272 (1992).

58. Nakano, T., Windrem, M., Zappavigna, V. & Goldman, S. A. Identification of a conserved 125 base-pair Hb9 enhancer that specifies gene expression to spinal motor neurons. *Dev. Biol* **283**, 474-485 (2005).

59. McLean, D. L., Fan, J., Higashijima, S., Hale, M. E. & Fetcho, J. R. A topographic map of recruitment in spinal cord. *Nature* **446**, 71-75 (2007).

60. Kawakami, K. *et al.* A transposon-mediated gene trap approach identifies developmentally regulated genes in zebrafish. *Dev. Cell* **7**, 133-144 (2004).

61. Inbal, A., Topczewski, J. & Solnica-Krezel, L. Targeted gene expression in the zebrafish prechordal plate. *Genesis* **44**, 584-588 (2006).

62. Scott, E. K. *et al.* Targeting neural circuitry in zebrafish using GAL4 enhancer trapping. *Nat. Methods* **4**, 323-326 (2007).

63. Brand, A. H. & Perrimon, N. Targeted gene expression as a means of altering cell fates and generating dominant phenotypes. *Development* **118**, 401-415 (1993).

64. Ellingsen, S. *et al.* Large-scale enhancer detection in the zebrafish genome. *Development* **132**, 3799-3811 (2005).

Chapter 2:

Optical lock-in detection imaging microscopy for contrast-enhanced imaging in living cells

This work has been published in the following article and is reprinted in full with permission*:*

Marriott G, Mao S, Sakata T, Ran J, Jackson DK, Petchprayoon C, Gomez TJ, Warp E, Tulyathan O, Aaron HL, Isacoff EY, Yan Y. **"**Optical lock-in detection imaging microscopy for contrast-enhanced imaging in living cells," *PNAS,* Nov 18, 2008.

For this work, I applied the photo-switchable genetically-encoded fluorophore *Dronpa* to the zebrafish larvae *in vivo* (Figure 5). I performed all zebrafish experiments which included the injection of *Dronpa* constructs into fertilized eggs for transient expression, screening of *Dronpa*-positive larvae, and imaging of *Dronpa*-expressing spinal neurons and muscle cells.

ABSTRACT

One of the limitations on imaging fluorescent proteins within living cells is that they are usually present in small numbers and need to be detected over a large background. We have developed the means to isolate specific fluorescence signals from background by using lock-in detection of the modulated fluorescence of a class of optical probe termed “optical switches.” This optical lock-in detection (OLID) approach involves modulating the fluorescence emission of the probe through deterministic, optical control of its fluorescent and nonfluorescent states, and subsequently applying a lock-in detection method to isolate the modulated signal of interest from nonmodulated background signals. Cross-correlation analysis provides a measure of correlation between the total fluorescence emission within single pixels of an image detected over several cycles of optical switching and a reference waveform detected within the same image over the same switching cycles. This approach to imaging provides a means to selectively detect the emission from optical switch probes among a larger population of conventional fluorescent probes and is compatible with conventional microscopes. OLID using nitrospirobenzopyran-based probes and the genetically encoded Dronpa fluorescent protein are shown to generate high-contrast images of specific structures and proteins in labeled cells in cultured and explanted neurons and in live *Xenopus* embryos and zebrafish larvae.

INTRODUCTION

Understanding the molecular basis for the regulation of complex biological processes such as cell motility and proliferation requires analysis of the distribution and dynamics of protein interactions within living cells in culture and in intact tissue (1). Tremendous advances have been made toward the development of new optical probes (2, 3) and imaging techniques that are capable of detecting proteins down to the level of single molecules (4–11). However, in living cells, such detection is compromised by autofluorescence, which can amount to several thousand equivalents of fluorescein per cell (12), as well as by light scattering (13). A major challenge in live-cell imaging, therefore, is to develop classes of probes and imaging techniques that are capable of resolving fluorescence signals from synthetic probes or genetically encoded fluorescent proteins in living cells and tissue against large background signals that may vary in time and space.

A simple and highly-effective approach for isolating a specific fluorescence signal from a large background is to reversibly modulate the fluorescence intensity of only a probe of interest that is bound to a specific protein by applying a uniform, rapid and specific perturbation (e.g., a change in temperature (14), pressure (15), or voltage (16) to which that probe is uniquely attuned. The modulated fluorescence can be isolated from other steady sources of background fluorescence by lock-in detection, making it possible to specifically extract the probe fluorescence even when it constitutes 0.1% or less of the total signal (16). Employing this concept, we developed optical lock-in detection (OLID) as a means for contrast-enhanced imaging of probes within living cells. We demonstrate

OLID on a chemical probe, nitrospirobenzopyran (nitroBIPS; 17–18), and on a fluorescent protein, Dronpa (19), both of which can be driven optically in a reversible manner between nonfluorescent and fluorescent states. These correspond respectively to the spiro (SP) and merocyanine (MC) states for nitroBIPS and the *trans* and *cis* states for Dronpa. Cross-correlation analysis is used to isolate the modulated signal of the probe and generate a pixel-by-pixel cross-correlation image, which enhances the contrast of the probe of interest over the background.

Several major advances in microscopy have been reported recently that exploit photochemical transitions between a nonfluorescent and fluorescent state of probe-labeled structures, including the superresolution imaging techniques of stochastic reconstruction optical microscopy (STORM), photoactivation light microscopy (PALM/FPALM) and stimulated emission depletion (STED) (6–11). In this study, the OLID approach is used to image ensembles of optical switch-labeled proteins in living cells, although by using a suitable high-quantum-yield optical switch probe, it should be possible to use OLID imaging microscopy to realize both superresolution and image contrast at the single-molecule level.

OLID using optical switch probes described herein affords key advantages for high-contrast imaging: (*i*) the mechanisms of optical switching of nitroBIPS (17–18, 20–21) and related photochromes (22) and Dronpa (19, 23) are known, and do not require chemical additives; (*ii*) optical switching between the two states (<2 μs) is much faster than probes used in PALM and STORM; (*iii*) optically driven transitions occur in the entire population of probe molecules, providing large signals and rapid imaging; and (*iv*) kinetic signatures and quantum yields for excited-state transitions can easily be measured in the sample and are used for lock-in detection. Thus, the properties of optically switched organic dyes and fluorescent proteins in OLID are compatible with rapid imaging of specific proteins and structures in live cells and within live animals and can be readily used in most laboratories on existing microscopes.

RESULTS

Deterministic Control of Optical-Switch Probe Fluorescence.

nitroBIPS and its derivatives (Fig. 1*A*) (17–18) undergo deterministic, rapid and reversible, optically driven, excited-state transitions between two distinct states, only one of which is fluorescent. As illustrated in Fig. 1*B* for nitroBIPS, a cycle of optical switching begins with excitation of the nonfluorescent SP state with either 2-photon (720 nm) or single-photon near-UV (365 nm) light, eliciting an excited-state isomerization to the fluorescent MC state. Subsequent excitation of MC using 543-nm light induces either red fluorescence or photoisomerization back to the nonfluorescent SP state. These rapid reactions proceed with defined quantum yields (20, 21) that lead to quantitative and deterministic interconversions between the SP and MC states within a single cycle of optical switching (Fig. 1*E*).

We first examined the ability of light to modulate the fluorescence of two synthetic switches within live cells, the thiol-reactive probe 8-iodomethyl-nitroBIPS (17–18) and the membrane probe C11-nitroBIPS (Fig. 1*A*). The transition from SP to MC was detected as a rapid increase in MC fluorescence that was complete within a single 2-photon scan (1.6-μs pixel dwell time) or within a 100-ms pulse of 365-nm light (Fig. 1 *C*–*E*). The conversion of MC to SP on the other hand, was elicited by using 543-nm excitation at an intensity that required several sequential scans of the field, each of which led to a defined decrease of MC fluorescence, according to the quantum yield for the MC to SP photoisomerization (20, 21). This decline in fluorescence was tracked over time for all pixels within the image. The repeated cycles of interconversion between the SP and MC states led to a characteristic saw-tooth waveform, with peak-to-trough MC-fluorescence levels that varied by <10% over 10 cycles of optical switching (Fig. 1*E*). The reproducibility of the increase and decrease in fluorescence demonstrates that nitroBIPS undergoes high-fidelity optical switching and is largely resistant to fatigue. From previous studies (17, 18), we know that the time constant for thermally driven (dark) transition of MC to SP is ≈3,000 s for protein-bound nitroBIPS, i.e., slow enough to enable nitroBIPS to function as an all-optically controlled switch. Thus, nitroBIPS-derived probes undergo 1- and 2-photon-driven, rapid, efficient, and high-fidelity optical switching within living cells using excitation intensities that are commonly used without toxicity in live-cell microscopy.

The genetically encoded protein Dronpa variant of the GFP (19, 23) undergoes optically driven, excited-state transitions between a fluorescent *cis* state and a nonfluorescent *trans* state with defined quantum yields (23). Dronpa was also shown to be an effective probe for OLID imaging. A single cycle of optical switching between the *trans* and *cis* states of Dronpa involved the following optical perturbations: two sequential scans of the field using 800 nm (2-photon, at an intensity of ≈45 mW at the sample) or a ≈100-ms pulse of 365-nm light were both effective in triggering the *trans*-to-*cis* transition, followed by 5–10 sequential scans of the field at 488 nm using a laser power at the sample of ≈70 μW to convert the fluorescent *cis* back to *trans*-Dronpa and to image Dronpa distribution. As shown below, optical switching between the two states of Dronpa could also be repeated over many cycles (as shown in Figs. 3 and 5 *C* and *D*).

Correlation Analysis.

To selectively amplify signals from the optical switch probes, a cross-correlation analysis was performed between every pixel in an image field and a reference waveform of the course of optical switching over several cycles [supporting information (SI) Fig. S1]. The reference waveform could be obtained internally, by recording the fluorescence of the optical switch in a small region (e.g., 5 × 5 pixels) that exhibited little background and displayed a large intensity modulation when imaged over multiple cycles of optical switching (Fig. 1*E*). Alternatively, an external reference waveform could be obtained by recording the fluorescence from optical switch probes covalently attached to immobilized micron-sized latex beads added to the sample, as shown below. The reference waveform for nitroBIPS showed highly reproducible profiles from

one optical switching cycle to the next (Fig. 1*E*). The correlation coefficient ρ(*x*, *y*) for any pixel location (*x*, *y*) is calculated as follows:

$$\rho(x, y) = \sum_{t} \frac{\{I(x,y,t) - \mu_I\}\{R(t) - \mu_R\}}{\sigma_I \sigma_R},$$

where, *I*(*x*, *y*, *t*)is the detected fluorescence intensity at pixel (*x*, *y*) at a time *t* during the switching cycle; and *R*(*t*)is the reference waveform. μ_I and μ_R are the mean values, and σ_I and σ_R are the standard deviation (std) values of the pixel fluorescence intensity and the reference waveform, respectively. The correlation coefficient has an absolute value varying from unity to zero (the few negative values indicate no or anti-correlation and are set to zero). The correlation values >0 are displayed on a pixel-by-pixel basis in an intensity-independent correlation image, which is unique to probes that undergo reversible excited-state transitions between fluorescent and nonfluorescent states. Because conventional fluorophores such as GFP and autofluorescence do not exhibit optical switching, their emission is not correlated with the reference waveform.

High-Contrast Fluorescence Imaging of NitroBIPS Probes in Living Neurons.

Having seen that patterns of excitation pulses can be used to drive the nitroBIPS optical switch between its fluorescent and nonfluorescent states in cultured cells (Fig. 1 *C*–*E*), we next asked whether the approach would work in intact tissue. We tested this in live *Xenopus* spinal cord explants (24, 25). Steady-state, red fluorescence images from the *Xenopus* spinal cord explant loaded with the membrane probe C11-nitroBIPS revealed a complex staining pattern with contributions from both MC and from a high-intensity yolk autofluorescence (Fig. 2*B*). A correlation analyses was performed by using as an internal reference waveform a region of nitroBIPS staining (Fig. 2*A*) that exhibited a large modulation over consecutive cycles of optical switching. The intensity image was dominated by a large number of particles that obscured the fine detail of the axons and cell-body protrusions. These were absent from the correlation image (Fig. 2*C*) and so, likely represented autofluorescent yolk particles. The C11-nitroBIPS probe was preferentially distributed within the membranes of both neurons and glia, with high values of the correlation coefficient found within the flat growth cone and filopodia (Fig. 2*C*). The correlation coefficient image of the growth cone and filopodia had a high signal even though the fluorescence intensity within these structures was low (Fig. 2*B*). The effectiveness of OLID in discriminating between the “DC” (steady-state intensity) and “AC” (modulated fluorescence) components of the fluorescence signal was further illustrated in an overlay of their spatial profiles (Fig. 2*D*, black and red traces, respectively). Analysis of the signal along the yellow box shown in the intensity and correlation images of the growth cone revealed a signal-to-background ratio of ≈2 (52/25) in the intensity image (Fig. 2*B*), which increased to >13 (205/15) in the correlation image (Fig. 2*C*).

High-Contrast Imaging of Dronpa-Actin in NIH 3T3 Cells.

Dronpa was also shown to be an effective probe for OLID imaging in this study. A single cycle of optical switching between the *trans* and *cis* states of Dronpa involved the following optical perturbations: two sequential scans of the field using 800-nm (2-photon, ≈45 mW at sample), or a ≈100-ms pulse of 365-nm light, were both effective in triggering the *trans*-to-*cis* transition, followed by 5–10 sequential scans of the field at 488 nm using a laser power at the sample of ≈70 μW to convert the *cis*- to *trans*-Dronpa. Optical switching between the two states of Dronpa was demonstrated by using these illumination conditions in the series of photoswitch cycles from a mixture of Dronpa-coupled and Fluoresbrite latex beads (Fig. 3*A*; green and white arrows respectively). The transitions between the two states of Dronpa could be repeated over multiple cycles, with ≈15% total loss of fluorescence (Fig. 3*C*, red, showing the intensity profile of Dronpa beads marked with short green arrow in Fig. 3*A*), likely because of cumulative occupancy of nonswitchable dark states (23). In contrast, the fluorescence intensity of the Fluorescbrite-bead (Fig. 3*A*, short white arrow, with intensity profile shown in black in Fig. 3*C*) was relatively stable with small fluctuations that were unrelated to the sequence of near-UV and 488-nm scans of the field. The mean correlation coefficient for the Dronpa beads (Fig. 3*B*) was 0.89. Because the intensity profile for the fluoresbrite beads (Fig. 3*C*, black) did not correlate with the reference waveform, i.e., the correlation coefficient was close to zero, these beads are not evident in the correlation image. Similar improvements in image contrast were obtained by using OLID for a mixture of Dronpa-beads and GFP-beads and by using 2-photon excitation of *trans*-Dronpa as shown in *SI Text* (Fig. S2).

Having found that we could selectively enhance detection of Dronpa on beads, we next turned to testing it in live cells. We expressed a fusion of Dronpa to actin in NIH 3T3 cells and compared its fluorescent signal to Dronpa-beads. Fluorescence-intensity images of the cells and of beads surrounding them showed the localization of Dronpa-actin to the cytoskeleton, with strong signals from stress fibers (Fig. 3*D*). Optical switching yielded almost identical fluorescence-intensity waveforms for Dronpa-actin in the cytoskeleton and Dronpa on the latex beads (Fig. 3*E*, compare black dots from Dronpa beads with blue dots for Dronpa-actin; fluorescence taken from regions indicated in Fig. 3*D*: with cytoskeleton marked by green arrow and bead with white arrow). This waveform provides a measure of the cumulative effects of the quantum efficiencies of optical switching, fluorescence, photobleaching, and fatigue in Dronpa over multiple cycles of optical switching. Because the profiles for the intracellular and extracellular derived waveforms are superimposed, we conclude that these quantum efficiencies are independent of environment. We note, however, that dissimilar profiles might occur for probes found in lower-pH environments (e.g., endosomes), although this is clearly not the case in the system under study.

Because Dronpa-actin made up the majority of the fluorescence signal in the cell shown in Fig. 3*D*, we examined similarly labeled cells to which GFP-latex beads (0.35 μm) were added to the medium to artificially increase the background signal (Fig. 3*F*). A pixel region showing the highest depth of *cis*-Dronpa fluorescence-intensity modulation

(green arrow in the stress fiber of the cell in Fig. 3*F*) was used to generate the internal reference waveform (data not shown). The signal-to-background ratio for the correlation image (Fig. 3*G*; scale is 0–1) was higher for specific structures compared with the intensity image (Fig. 3*F*; scale is 0–255) because of the almost complete absence of GFP background. In some regions, the contrast enhancement increased the signal to background ratio from 5:1 in the intensity image to as high as 100:1 in the correlation image (green versus white arrows in Fig. 3 *F* and *G*). Attempts to adjust the brightness and/or contrast for the intensity image shown in Fig. 3*F* to achieve the same quality contrast as that obtained in the correlation image were unsuccessful. This was also the case for all other images using nitroBIPS or Dronpa presented in this study.

OLID Imaging of Dronpa in Neurons and Muscle, in Vitro and in Vivo.

A major need for optical microscopy is to develop methods that improve imaging in tissues and in vivo, where background fluorescence can be high and where it is important to generate high-content images quickly under modest levels of irradiation. To assess OLID for such applications, we set out to use Dronpa to image neurons and muscle in intact spinal cord and in live animals. First, we imaged cultured postnatal rat hippocampal neurons and found that the Dronpa-actin probe could be modulated between its nonfluorescent and fluorescent forms very effectively within the tissue (Fig. 4*A Inset*). The correlation image of Dronpa-actin derived from these data (Fig. 4*B*; correlation coefficient values 0–0.7) substantially enhanced signals from dendritic shafts, increased the visibility of fine dendrites, and drastically improved the visualization of dendritic spines, which were buried in the background in the intensity image (Fig. 4*A*; scale 0–160 of an 8-bit range). The improvement to image contrast for these structures can also be seen in profiles of the intensity and correlation coefficient along a line defined by the yellow arrows in Fig. 4 *A* and *B* shown in Fig. S3.

We next used OLID imaging to map the distribution of Dronpa-actin within the highly autofluorescent tissue of *Xenopus* embryos. Several cell types were found to express Dronpa-actin in the live *Xenopus* embryo ≈24 h after DNA injection and fertilization. We focused our attention on motor neuron growth cones. The fluorescence of *cis*-Dronpa-actin was bright at the center of the growth cone and lower at the edge and in the axon, where the brightness was similar to that of autofluorescence in surrounding muscle cells (Fig. 4*C*). OLID correlation over only 2 cycles of optical switching of Dronpa-actin provided a high-contrast image of Dronpa-actin within the axon, edge of the growth cone, and emerging filopodia and effectively suppressed the high-autofluorescence signal from the muscle cells (Fig. 4*D*).

Having seen significant contrast enhancement in cultured neurons and intact embryos, we proceeded to OLID imaging of Dronpa in live zebrafish. UAS-Dronpa-actin injected into the single-cell stage of the st1020 GAL4 line (26) expressed strongly in muscle at 5 days after fertilization (dpf) and could be readily detected in an intensity image (Fig. 5*A*) of tricaine-paralyzed fish embedded in low-melting-point agarose. Optical modulation of Dronpa-actin fluorescence was readily achieved in the larva, as seen in the intensity trace during optical switching in Fig. 5*C*. The correlation image of the muscle enhanced

structural details of sarcomeric organization and the paths of individual myofibrils (Fig. 5*B*) that were difficult to discern from the intensity image and effectively removed background from the outer regions of the sample indicated by a green arrow in Fig. 5 *A* and *B*. OLID also enhanced the imaging of zebrafish neurons. UAS-Dronpa injected into the single-cell stage of the st1011 GAL4 line (26) expressed strongly in larval spinal cord interneurons at 5 dpf. Optical switching was reversible and highly reproducible over 10 cycles of 2-photon photoisomerization to the fluorescent *cis*-Dronpa state, followed by 1-photon imaging and return isomerization (*Upper Inset*, Fig. 5*D*, cell body marked by a white arrow). The correlation image augmented the signal from fine processes of these neurons and for specific regions along a line indicated by the yellow arrows in Fig. 5 *D* and *E* increased the signal to background ratio from 6.8 for the intensity image to 35.4 for the same pixels in the correlation image (profile shown in Fig. S4).

DISCUSSION

OLID microscopy provides a powerful tool for contrast-enhanced imaging, allowing specific resolution of the fluorescence signals from synthetic or genetically encoded optical switches such as nitroBIPS and Dronpa within a variety of live-cell systems, in culture and within living embryos, that usually contain substantial background signals. The approach relies on the specific property of the optical switches whereby their fluorescence emission is modulated as they are driven back and forth, with two distinct wavelengths of light, between nonfluorescent and fluorescent states. This produces a stimulus-coupled change that is distinct from the native sources of cellular fluorescence, such as protein-bound NAD(P)H and $FADH_2$, and from the vast majority of extrinsic fluorophores and fluorescent proteins, enabling the desired cell structure to which the optical switch is targeted, or the protein to which it is attached, to be visualized above the autofluorescent background and amplified above the level of other indicators and trackers. The simple way that the signal from optical switches is enhanced is by generating a correlation image, i.e., to display the correlation coefficient of fluorescence with respect to an internal reference of a bead or cell structure that is enriched for the optical switch. This makes it possible to visualize a small modulated or AC signal from an optical switch over the other sources of fluorescence by selectively enhancing the modulated pixels and excluding the unmodulated ones. This method of isolating the specific signal from the optical switch in an image is similar in several aspects to radar, and to lock-in and phase-sensitive detection techniques that are widely used in the physical, chemical, and life sciences.

The usefulness of Dronpa as an optical switch is somewhat limited by its high fluorescence quantum yield and tendency to transition into a nonswitchable state (23) that leads, in some cases, to loss of switchable Dronpa over the course of an optical switching study. Despite this complication, our analyses of Dronpa probes showed that the intensity profile within each cycle is constant even after 12 cycles of switching and loss of >50% of the original *cis*-Dronpa signal (Fig. S2). At this point in an experiment, an even in cases where only a modest modulation of the fluorescence signal is

achieved (Fig. S2), the waveforms still generate correlation images that exhibit a high degree of contrast. The ability to genetically encode fusions of an optical switch probe with any protein in a living cell adds such a great measure of convenience and specificity that Dronpa is most likely to have the broadest immediate impact for cellular imaging. This will motivate a search for dark-state and fatigue-resistant, fast-switching, multicolored, and infrared-emitting Dronpa variants that might include the recently described Dronpa-2 and Dronpa-3 (19).

The contrast-enhancing power of OLID imaging extends to imaging Dronpa-actin and cytoplasmic Dronpa in rat hippocampal neurons, neurons in live *Xenopus* embryos, and in muscle cells and neurons in live zebrafish larvae by using 2-photon illumination to generate the fluorescent states and 1-photon illumination to image and restore the nonfluorescent state. Together, the properties of OLID imaging microscopy using nitroBIPS and Dronpa-related switches will allow for rapid, deep-tissue imaging of specific probes and markers proteins within living animals with superior image contrast compared with existing probes and imaging modalities.

MATERIALS AND METHODS

Synthesis of C11-nitroBIPS.

C11-nitroBIPS (Fig. 1*A*) was prepared according to the methods described in Sakata *et al.* (18) and is detailed in *SI Text*.

Cell Culture and Transfection.

Standard cell-culture methods were used for mammalian and *Xenopus* preparations as detailed in *SI Text*.

Plasmid Construction and Protein Purification.

Standard molecular biology and protein purification methods were used for the expression of genes in cells and for preparation of Dronpa and GFP as detailed in *SI Text*.

Labeling of Intracellular Proteins with 8-Iodomethyl-NitroBIPS.

Standard probe-labeling techniques were used for studies detailed in this study as described in *SI Text*.

Imaging System and Optical Manipulation of MC-and *cis*-Dronpa Fluorescence in Cells.

Three different microscope systems were used to image and manipulate optical switch-labeled cells. Details of these systems are provided in *SI Text*.

Cultured Neurons.

Dissociated hippocampal cultures were prepared from P1 rats and transfected and imaged as described in *SI Text*.

Dronpa Imaging in Zebrafish.

Single-cell *s1011t:GAL4* and *s1020t:GAL4* embryos (26) were injected with plasmid DNA for *UAS:Dronpa* or *UAS:Dronpa-actin* at 20 ng/μl along with 50 ng/μl transposase mRNA and 0.04% phenol red. Zebrafish were raised at 28.5 °C in E3 medium and imaged at 5 dpf, as described in *SI Text*.

Figure 1

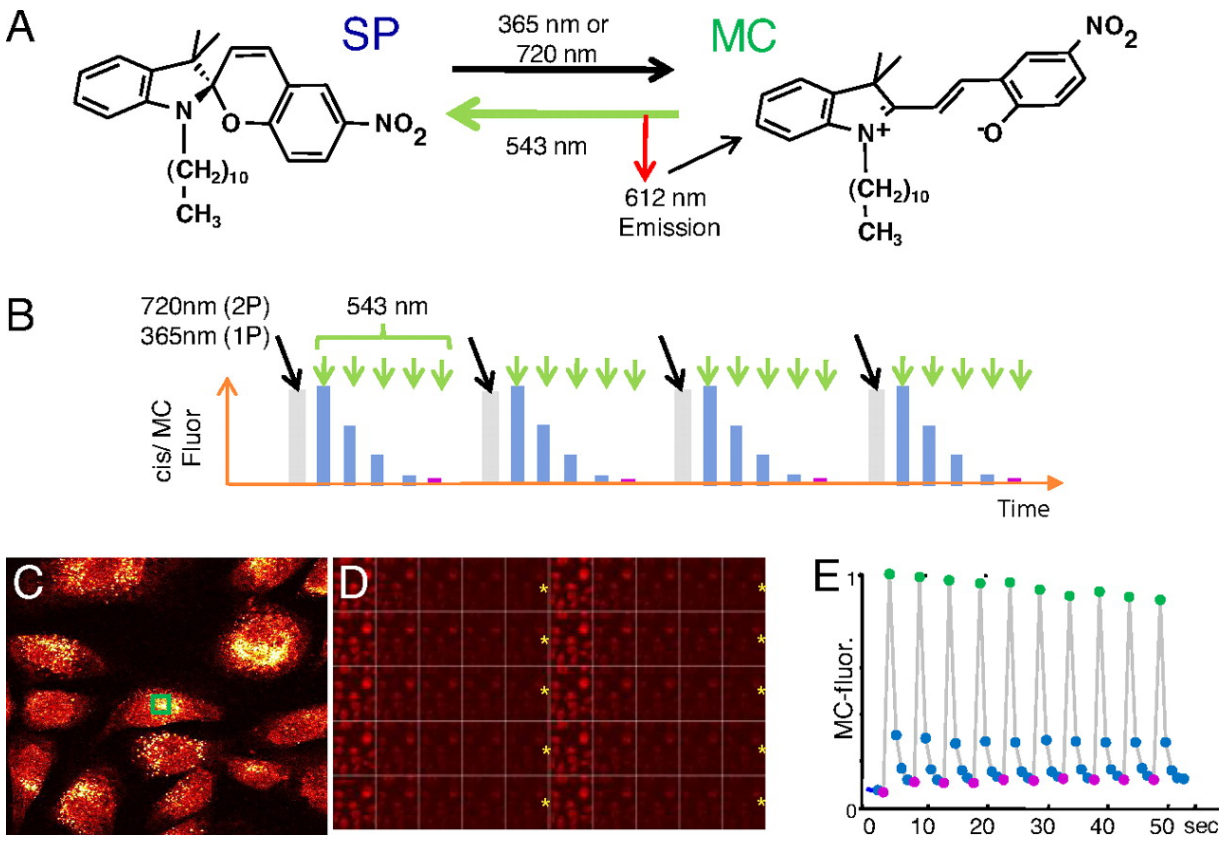

Fig. 1. Cyclic excitation repeatedly switches nitroBIPS fluorescence on and off. (*A*) Structure and excited-state reactions of the C11-nitroBIPS optical switch. Excitation of nonfluorescent SP state with either 2-photon (720 nm) or single-photon near-UV (365 nm) light elicits isomerization to fluorescent MC state. Subsequent excitation of MC (543 nm) induces red fluorescence or photoisomerization to the nonfluorescent SP state. (*B*) Defined waveform of optical perturbation of nitroBIPS results in deterministic control of fluorescent and nonfluorescent states. Progress of photochemical reactions is detected by using the fluorescence of the MC-state of nitroBIPS. (*C–E*) Cycling MC-fluorescence in live NIH 3T3 cells loaded with thiol-reactive 8-IodomethylBIPS. (*C*) Single image of cells at peak fluorescence. (*D*) Ten cycles of optical switching as seen in MC-fluorescence images of cells shown in *C*. Each cycle consists of a 100-ms pulse of 365-nm light (yellow asterisk), followed by a series of 1-s scans of the field using 543 nm and imaged with a 560-nm long-pass filter. (*E*) Trace of the normalized modulated intensity of MC-fluorescence (internal reference waveform) in one cell (*C*, green box) over 10 cycles of optical switching.

Figure 2

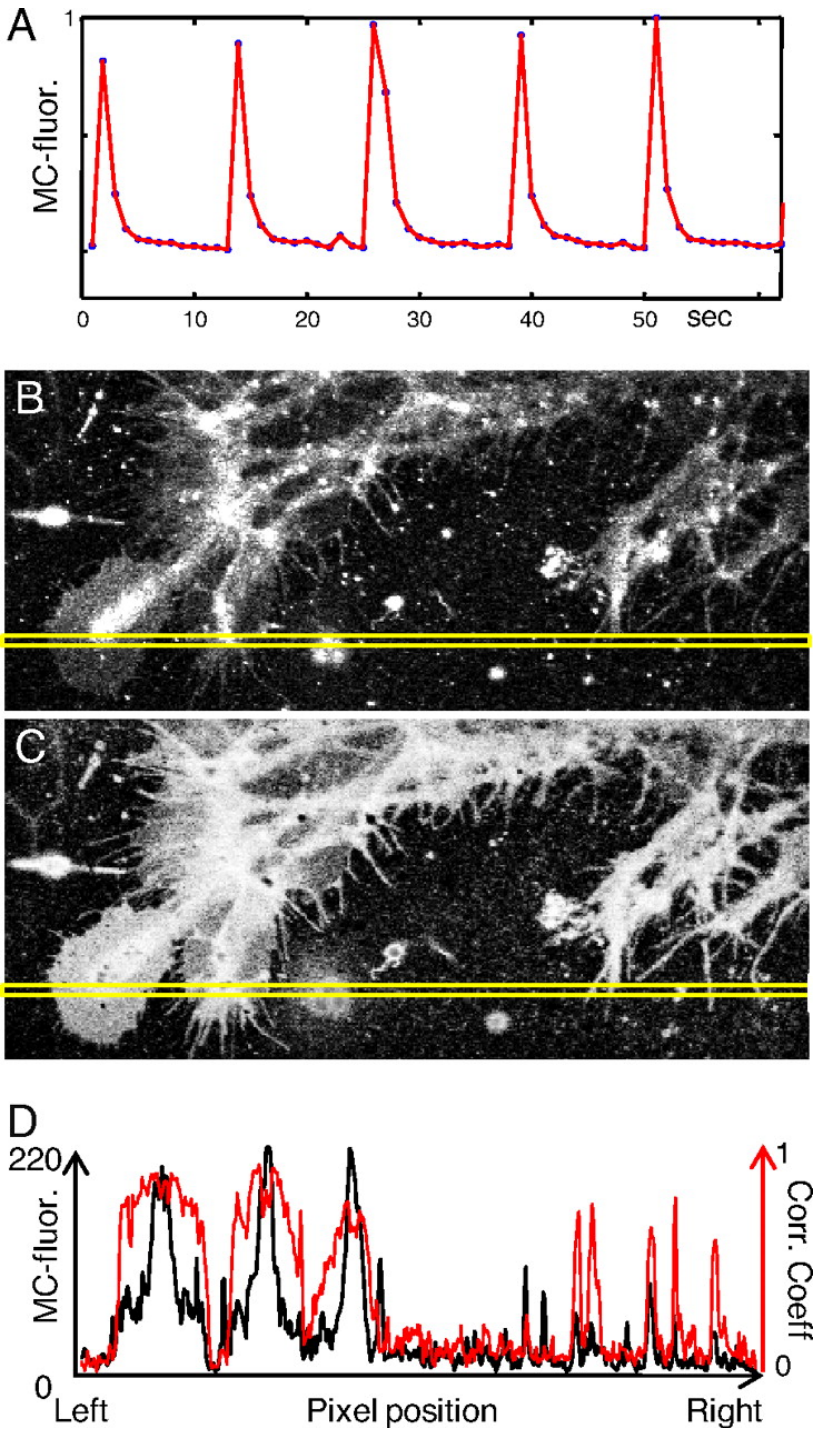
A
1
MC-fluor.
0
10
20
30
40
50
sec
B
C
D
220
MC-fluor.
0
Left
Pixel position
Right
1
Corr. Coeff
0

Fig. 2. OLID for imaging live *Xenopus* spinal cord explants using nitroBIPS probes. (*A*) Internal reference waveform for the optical switching of C11-nitroBIPS in cells within a *Xenopus* spinal cord explants measured by using MC-fluorescence. The normalized waveform was obtained from a selected region of 5 × 5 pixels with strongest MC-fluorescence corresponding to 5 cycles of optical switching of the probe and was used in the pixel-by-pixel calculation of the correlation coefficient. (*B*) Fluorescence-intensity image of the C11-nitroBIPS stained cells within the *Xenopus* spinal cord explant. (*C*) Correlation image corresponding to *B*, which used *A* as a reference waveform. (*D*) Traces of the relative fluorescence intensity (black) and the correlation (red) of C11-nitroBIPS for the yellow boxed region in *B* and *C*, respectively.

Figure 3

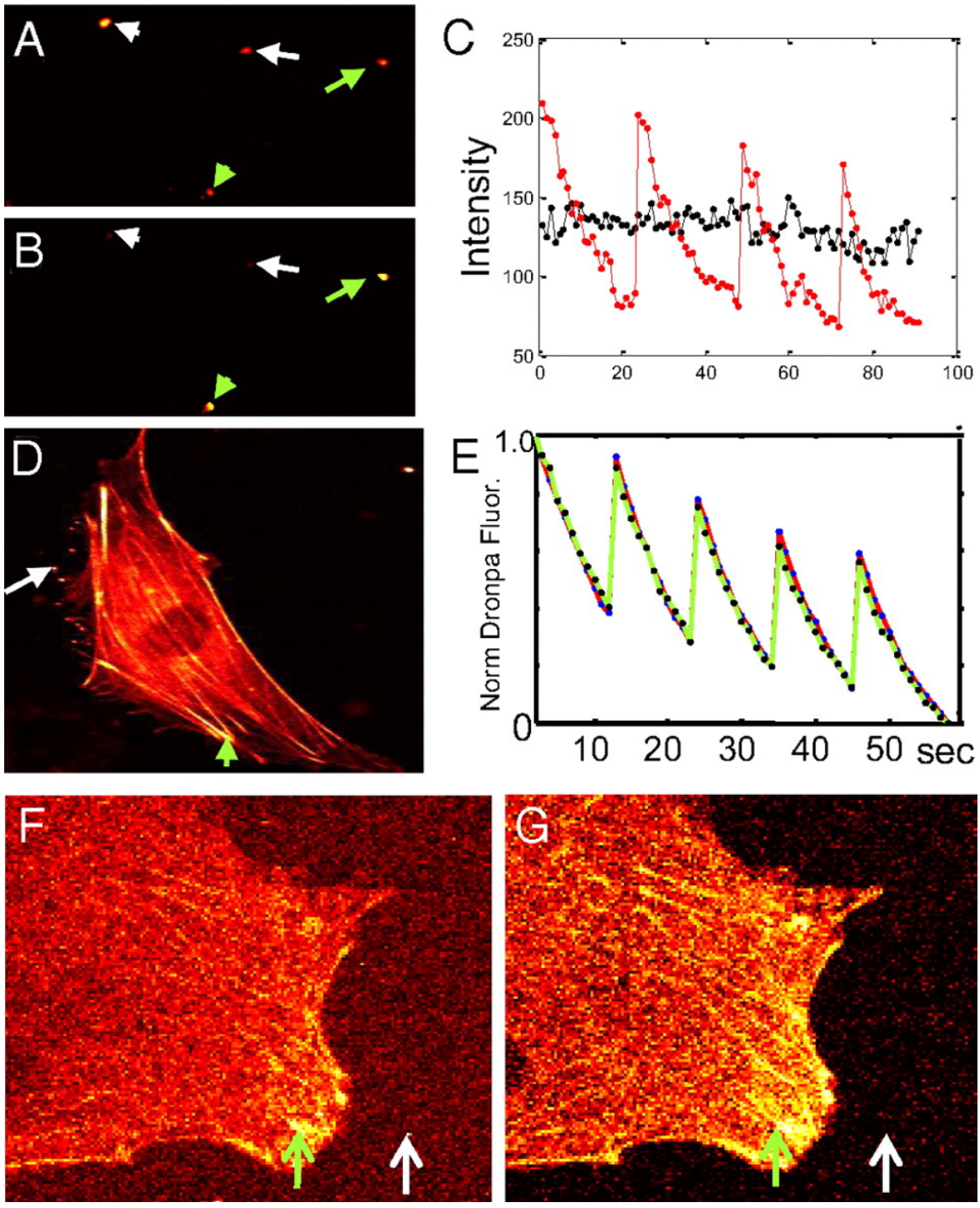
A
B
C
Intensity
250
200
150
100
50
0
20
40
60
80
100
D
E
Norm Dronpa Fluor.
1.0
0
10
20
30
40
50
sec
F
G

Fig. 3. Optical switching of Dronpa. (*A*) Intensity image of Dronpa-beads (green arrows) mixed with a cluster of 40-nm fluoresbrite beads (white arrows). (*B*) Correlation image of same image field as in *A* shows the Dronpa-beads but not the 40-nm fluoresbrite beads. (*C*) Fluorescence-intensity profiles for optical switching of a single 0.35-μm Dronpa-latex bead [red trace from bead marked with the short green arrow (*A*)] and the uncorrelated and much more constant intensity from the fluoresbrite bead cluster (black trace from bead marked with the short white arrow in *A*). Optical cycling was achieved by using a single 100-ms pulse of 365-nm light to convert nonfluorescent *trans*-Dronpa to the fluorescent *cis*-Dronpa and 488-nm excitation to evoke fluorescence and the reverse isomerization. The fluoresence-intensity axis applies to both profiles. (*D*) Image of Dronpa-actin in a living NIH 3T3 cell (green arrow) compared with Dronpa-coupled 1-μm latex beads (white arrow). Beads were used to generate an external reference waveform of optical switching. Transition to the fluorescent *cis* state is triggered by excitation of the *trans* state at 365 nm for 100 ms. Subsequent excitation of *cis*-Dronpa at 488 nm is used to bring about the *cis*-to-*trans* photoisomerization. (*E*) Normalized fluorescence-intensity profiles of *cis*-Dronpa in a stress fiber in the NIH 3T3 cell (green arrow in *D*; red trace, with data shown as blue dots) and a Dronpa-bead located next to the cell (white arrow in Fig. *D*; green trace, with data shown as black dots) over the course of 5 cycles of optical switching. Note that the internal reference waveform generated from Dronpa-actin in the live cell is almost identical to that of the external reference waveform derived from Dronpa on the bead. (*F* and *G*) Fluorescence-intensity (*F*) and correlation (*G*) images of Dronpa-actin in NIH 3T3 cell (Intensity scale is 0–255, and the correlation coefficient is 0–1). The intensity image was taken immediately after a 200-ms 365-nm pulse. GFP-coupled latex beads (0.35 μm) were added to the external medium to add a milky background signal with bright spots, presumably representing bead aggregates (white arrow). The green arrow indicates the location of a focal contact, containing a high concentration of Dronpa-actin, that was used to generate an internal reference waveform.

Figure 4

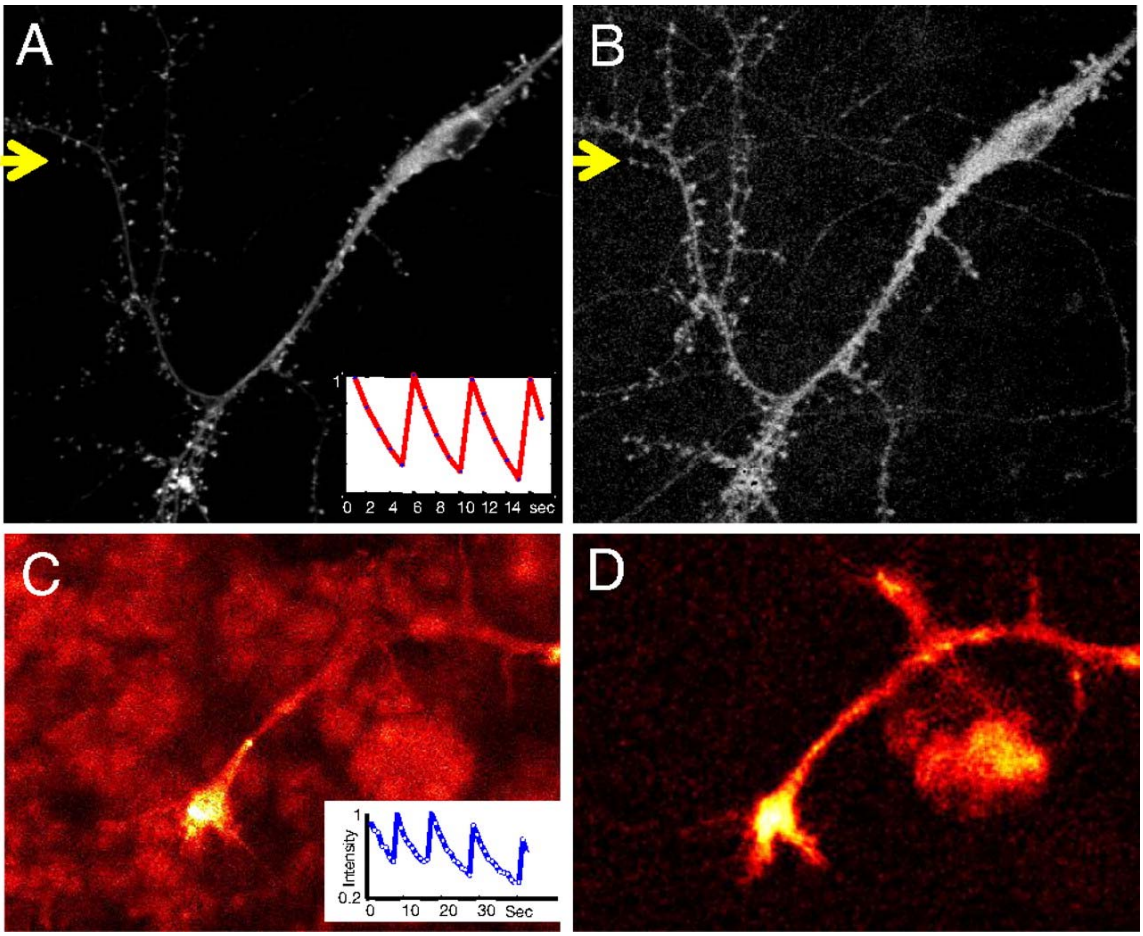

Fig. 4. OLID-imaging of Dronpa in cultured mammalian neurons and *Xenopus* spinal cord explant. (*A*) Fluorescence-intensity image of Dronpa-actin transiently expressed in rat P1 hippocampal neurons, transfected at 8 days in vitro (DIV) and imaged in live cells at 11 DIV. The *Inset* shows normalized fluorescence intensity of the internal reference over 3 cycles of optical switching. (*B*) Correlation image of Dronpa-actin of same field as in *A* improves contrast and reveals finer processes and dendritic spines. Profiles of the fluorescence intensity and correlation coefficient along a line defined by the yellow arrows (*A* and *B*, respectively) are shown in Fig. S3. (*C*) Image of the fluorescence intensity of *cis*-Dronpa-actin within the growth cone of a motor neuron in a live, deskinned *Xenopus* embryo. The *Inset* shows the internal reference waveform derived from optical switching of Dronpa-actin in the cell body. (*D*) Correlation image of Dronpa-actin for image field shown in *C*. The improvement in contrast in the correlation image is largely from the suppression of background of the muscle cells that is evident in the intensity image. (For details see *SI Text*).

Figure 5

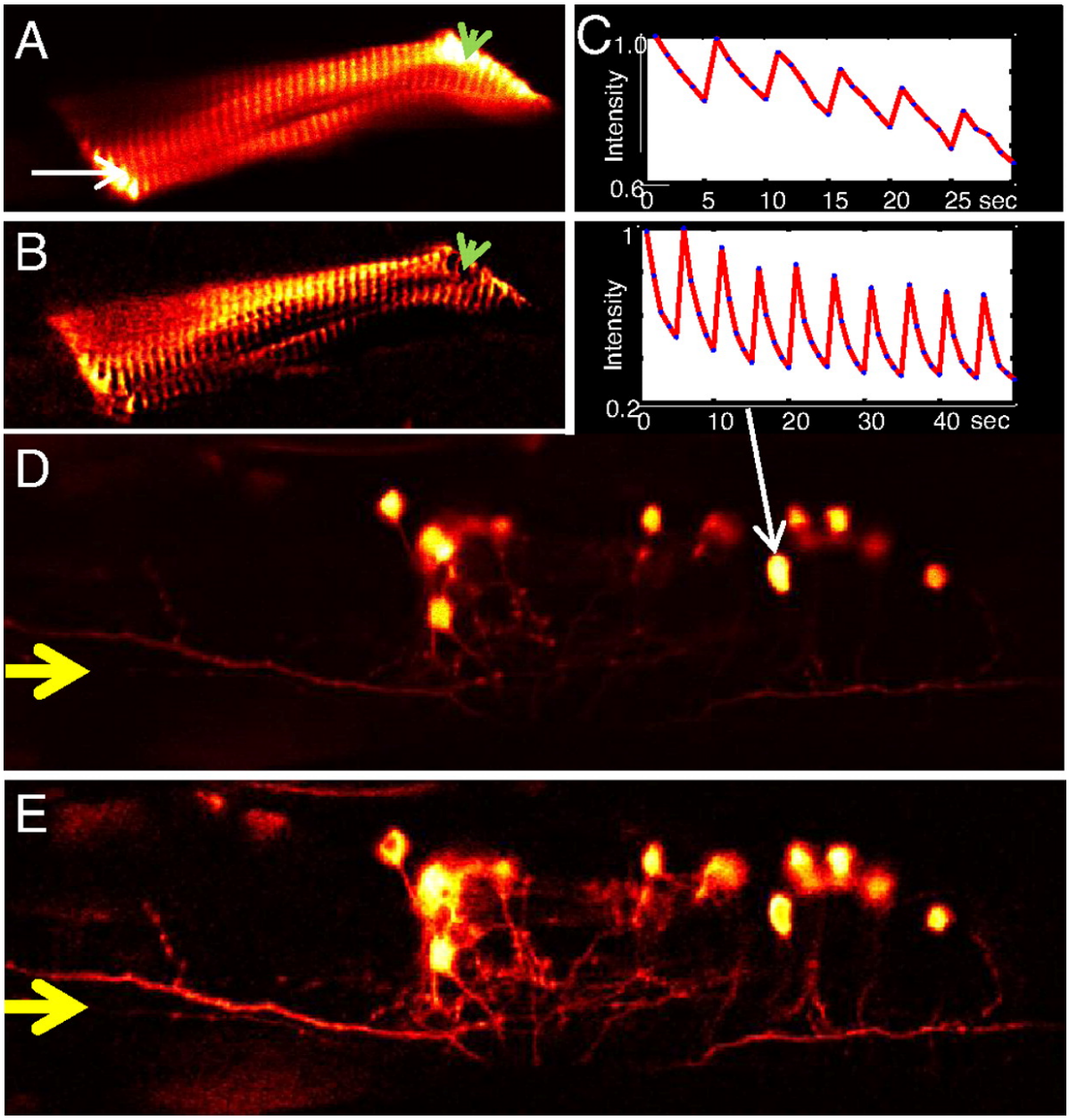
A
B
C
1.0
Intensity
0.6
0
5
10
15
20
25 sec
1
Intensity
0.2
0
10
20
30
40 sec
D
E

Fig. 5. OLID-imaging of Dronpa in live zebrafish. (*A*–*C*) OLID imaging of Dronpa-actin in muscle of live zebrafish larva. (*A* and *B*) Fluorescence-intensity image (*A*) and correlation-coefficient image (*B*) of Dronpa-actin in larval muscle at 5 dpf. Note that details of sarcomeric organization are sharper in the correlation coefficient image. The green arrow indicates the region that has considerable background fluorescence but little to no correlation, suggesting an absence of Dronpa-actin. (*C*) Saw-tooth modulation of the normalized fluorescence intensity by optical switching between *trans*- and *cis*-Dronpa-actin in zebrafish muscle of *A*. (*D* and *E*) OLID imaging of cytoplasmic Dronpa in neurons of live zebrafish larva. Fluorescence-intensity image (*D*) and correlation image (*E*) and modulation of the normalized fluorescence intensity by optical switching (*D Inset*) of cytoplasmic Dronpa in spinal cord interneurons in larva at 5 dpf. Profiles of the intensity and correlation coefficient for these data along a narrow box defined by the yellow arrows are shown in Fig. S4

REFERENCES

1. Yan Y, Marriott G. Analysis of protein interactions using fluorescence technologies. Curr Opin Chem Biol. 2003;7:635–640.

2. Zhang J, Campbell R, Ting A, Tsien R. Creating new fluorescent probes for cell biology. Nat Rev Mol Cell Biol. 2002;3:906–918.

3. Westphal M, et al. Microfilament dynamics in motility and cytokinesis imaged with GFP-actin. Curr Biol. 1997;7:176.

4. Axelrod D. Total internal reflection fluorescence microscopy in cell biology. Methods Enzymol. 2003;361:1–33.

5. Koyama-Honda I, et al. Fluorescence imaging for monitoring the colocalization of two single molecules in living cells. Biophys J. 2005;88:2126–2136.

6. Hell SW, Dyba M, Jakobs S. Concepts for nanoscale resolution in fluorescence microscopy. Curr Opin Neurobiol. 2004;14:599–609.

7. Betzig E, et al. Imaging intracellular fluorescent proteins at nanometer resolution. Science. 2006;313:1642–1645.

8. Rust MJ, Bates M, Zhuang X. Sub-diffraction-limit imaging by stochastic reconstruction optical microscopy (STORM) Nat Methods. 2006;3:793–795.

9. Bates M, Huang B, Dempsey GT, Zhuang X. Multicolor super-resolution imaging with photo-switchable fluorescent probes. Science. 2007;317:1749–1753.

10. Hofmann M, Eggeling C, Jakobs S, Hell S. Breaking the diffraction barrier in fluorescence microscopy at low light intensities by using reversibly photoswitchable proteins. Proc Natl Acad Sci USA. 2005;102:565–569.

11. Hess ST, Girirajan TP, Mason MD. Ultra-high resolution imaging by fluorescence photoactivation localization microscopy. Biophys J. 2006;91:4258–4272.

12. Aubin J, Histochem J. Autofluorescence of viable cultured mammalian cells. J Histochem Cytochem. 1979;27:36–43.

13. So PTC, Kim H, Kochevar IE. Two-photon deep tissue ex vivo imaging of mouse dermal and subcutaneous structures. Opt Express. 1998;3:339–350.

14. Eigen M, Maeyer LD, Weissberger A. Technique of Organic Chemistry. Vol 8. New York: Interscience; 1963. p. 895.

15. MacGregor R, Clegg RM, Jovin TM. Pressure-jump study of the kinetics of ethidium bromide binding to DNA. Biochemistry. 1985;24:5503–5510.

16. Mannuzzu L, Moronne M, Isacoff E. Direct physical measure of conformational rearrangement underlying potassium channel gating. Science. 1996;271:213–216.

17. Sakata T, Yan Y, Marriott G. Optical switching of dipolar interactions on proteins. Proc Natl Acad Sci USA. 2005;102:4759–4764.

18. Sakata T, Yan Y, Marriott G. Family of site-selective molecular optical switches. J Org Chem. 2005;70:2009–2013.

19. Ando R, Flors C, Mizuno H, Hofkens J, Miyawaki A. Highlighted generation of fluorescence signals using simultaneous two-color irradiation on Dronpa mutants. Biophys J. 2007;92:97–99.

20. Bletz M, Pfeifer-Fukumura U, Kolb U, Baumann W. Ground- and first-excited-singlet-state electric dipole moments of some photochromic spirobenzopyrans in their spiropyran and merocyanine form. J Phys Chem A. 2002;106:2232–2236.

21. Görner H, Matter S. Photochromism of nitrospiropyrans: Effects of structure, solvent and temperature. Phys Chem Chem Phys. 2001;3:416–423.

22. Giordano L, Jovin T, Irie M, Jares-Erijman E. Diheteroarylethenes as thermally stable photoswitchable acceptors in photochromic fluorescence resonance energy transfer (pcFRET) J Am Chem Soc. 2002;124:7481–7489.

23. Dedecker P, et al. Fast and reversible photoswitching of the fluorescent protein dronpa as evidenced by fluorescence correlation spectroscopy. Biophys J. 2006;91:L45–7.

24. Gomez T, Harrigan D, Henely J, Robles E. Working with *Xenopus* spinal neurons in live cell culture. Methods Cell Biol. 2003;71:130–154.

25. Gomez T, Robles E. Imaging calcium dynamics in developing neurons. Methods Enzymol. 2003;361:407–422.

26. Scott EK, et al. Targeting neural circuitry in zebrafish using GAL4 enhancer trapping. Nat Methods. 2007;4:323–326.

SUPPORTING INFORMATION

Synthesis of C11-NitroBIPS. C11-NitroBIPS was prepared according to the methods described in Sakata *et al.* (1). Briefly, 2,3,3-trimethyl-3H-indole was refluxed with 1-bromo-undecane in CH_2Cl_2 for 12 h. After filtration, the solid was dissolved in 0.5 M NaOH and stirred for 15 min. Extraction with CH_2Cl_2 gave *N*-undecyl-dihydroindole. The dihydroindole was coupled with 5-nitrosalicylaldehyde and SiO_2 column chromatography afforded pure C11-nitroBIPS (Fig. 1*A*).

Plasmid Construction. Dronpa-actin was subcloned into the pCDNA vector (Invitrogen) between the XhoI and HindIII restriction sites. For the study of zebrafish, Dronpa-actin was subcloned into the pT2KXIGΔin vector between the SpeI and NotI restriction sites. For protein purification, Dronpa was subcloned into the pTrcHisC vector (Invitrogen) between the XhoI and HindIII restriction sites and transformed into JM109 *Escherichia coli* (Promega) by using the manufacturer's recommended protocol. The Dronpa protein was expressed and purified according to the handbook of Ni-NTA affinity chromatography (Qiagen). All constructs were verified by DNA sequencing.

Cell Culture and Transfection. NIH 3T3 (Mouse embryonic fibroblast cell line) cells were grown in DMEM (Invitrogen) supplemented with 10% fetal bovine serum (Invitrogen), 1% penicillin–streptomycin (Invitrogen), and 0.2% Fungizone Amphotericin B (Invitrogen) and transfected by using an ECM 830 electroporator (BTX) with a 7-ms pulse of 210 V. The cultures were kept at 37 °C in a humidified atmosphere with 5% CO_2. *Xenopus* spinal cord explants cultures were prepared as described by Gomez *et al.* (2, 3).

Cultured Neurons. Dissociated hippocampal cultures were prepared from P1 rats and transfected, as described previously (4). After 8 DIV, cells were transfected with 1.5 μg of DNA per 12-mm coverslip by using calcium phosphate. Live cultures were imaged after 11 DIV by using a Zeiss LSM 510/NLO META confocal microscope. A Spectra-Physics MaiTai HP laser was used for 2-photon activation, and a 488-nm argon laser was used for imaging. One-micron optical sections were collected with a pixel time of 1.6 μs. Achroplan IR 40x/0.80 W or Achroplan IR 63x/0.95 W dipping objectives were used.

Labeling of Intracellular Proteins with 8-Iodomethyl-NitroBIPS. Cells from 16- to 20-h-old *Xenopus* spinal cord explants plated on poly-D-lysine-coated coverslips were treated with a freshly prepared solution of 100 _M 8-iodomethyl-nitroBIPS (1) for 5 min. The thiol-reactive optical switch readily crosses the plasma membrane and labels cysteine-containing peptides and proteins. Some cells in the explant preparations contained yolk that exhibited a red fluorescence that provided a convenient autofluorescence signal for OLID imaging microscopy.

Imaging System and Optical Manipulation of MC-and cis-Dronpa Fluorescence in Cells. Three different microscope systems were used to image and manipulate nitroBIPS-labeled cells. (*i*) Images were collected on an Olympus FluoView500 confocal

microscope using a 60x, N.A. = 1.45 oil immersion objective. UV light pulses from a 100-W Hg-arc lamp filtered through a 365 ± 25 bandpass filter were controlled with a time-varying shutter (Vincent Associates) to drive the SP to MC transition and was described in Gomez *et al.* (3). The duration of the 365-nm pulse was varied from 5 to 500 ms. Imaging of MC and concomitant conversion of the MC-excited state to SP was driven by using 543-nm laser scanning at a rate of ~3 frames per second, whereas the emission was collected by using a 560-nm long-pass filter. The fastest laser scan speed used translated into a 2-μs pixel dwell time. A typical optical switching cycle was composed of a 100-ms pulse of 365-nm light during continuous scanning of the 543-nm laser. The use of a laser power consistent with live-cell imaging converted all MC in the image field to SP within 5 scans. Thus, an optical switch cycle composed of the complete interconversion of SP to MC and then MC to SP within an image field required ~1-10 s. Because the shutter controlling the 365-nm light source was not synchronized with the scanning of the 543-nm laser, the MC-fluorescence intensity was averaged in cases where the 365-nm pulse spanned two sequential 543-nm laser scans, and in cases where the 365-nm pulse was contained within a single scan, the MC-fluorescence from the previous image was used to generate the average. (*ii*), A Zeiss 510 META NLO on a AxioImager Zl stand with a Spectra-Physics MaiTai HP ti:sapphire laser was also used to image and manipulate NitroBIPS and Dronpa optical switches in living cells. Excitation of the SP state of NitroBIPS was achieved by using 720-nm (2-photon) excitation of the image field with the 63x/0.95 NA LWD water-immersion dipping objective. The MC-to-SP transition was driven by using 543-nm excitation of the image field and the concomitant MC-fluorescence was imaged by using a bandpass filter. The fastest scan speed of the 2-photon laser translated into a 1.6-μs pixel dwell time. (*iii*), A Bio-Rad Radiance 2100 MP Rainbow Confocal/Multiphoton System was used to image and manipulate Dronpa-actin optical switches in living cells. Excitation of Dronpa was achieved by using 35% 800-nm 2-photon excitation of the image field with PlanApo 60x oil objective. Imaging of Dronpa and concomitant conversion of the fluorescence state to no fluorescence state was driven by using 30% of the maximum power from a 488-nm laser scanning at a frame rate of 0.32 Hz, whereas the 500- to 530-nm emission was collected through a 500-nm long-pass filter (HQ500LP) and a 530-nm emission filter (HQ530SP).

Dronpa Imaging in Zebrafish. Single-cell *s1011t:GAL4* and *s1020t:GAL4* embryos (4) were injected with plasmid DNA for *UAS:Dronpa* or *UAS:Dronpa-actin* at 20 ng/μl, along with 50 ng/_l transposase mRNA and 0.04% phenol red. Zebrafish were raised at 28.5°C in E3 medium and imaged at 5 dpf. Dronpapositive fish were selected for fluorescence after activation of Dronpa by a 365-nm UV lamp. For live imaging, zebrafish larvae were mounted in 2% low-melting-point agarose (Invitrogen) and bathed in E3 medium containing 0.02% tricaine (Sigma) to prevent motion artifacts. Two-photon activation and confocal imaging of Dronpa was performed on a Zeiss 510 Axioplan META system using the LSM510 bleach function and a 63x objective. Dronpa was activated by 2-photon with a 780-nm laser set at 25–35% power. For neurons, activation was performed for 2 scans at 1.6 μs per pixel (1,024 x 1,024 pixels per image frame), and confocal images were acquired with a 488-nm laser at 17–24% power for 1.6 μs per pixel with an optical slice of 4.4 μm. For muscle cells, activation was performed for 2

scans at 2.5 μs per pixel (512 x 512 pixels per image frame), and confocal images were acquired with a 488-nm laser at 4% power for 2.5 μs per pixel with an optical slice of 2.5 μm. Two-photon activation of Dronpa was followed by 5 confocal images and repeated 10 times for all images.

Lock-in Detection and Correlation Images. An internal reference intensity profile, reflecting the time-varying change in *cis*- Dronpa emission in response to the train of 800-nm and 488-nm scans is established from a selected pixel region having little background and greater signal of interest, which represents a structure with a high density of Dronpa-actin or one of the 0.35-μm latex beads covalently labeled with Dronpa that are added to the preparation. A cross-correlation between the intensity of any pixel in the image, as a function of time, and the reference signal is calculated to yield the correlation coefficient that is displayed on a pixel-by-pixel basis to construct a correlation image, which reveals correlation between the raw intensity and the modulated intensity profile over the switching cycles. Any negative values of the correlation coefficient represent noncorrelation with the reference waveform and are set to zero. In some situations, e.g., Fig. S2, the squared value of the correlation coefficient (within the range of 0–1) is displayed to highlight the structures exhibiting higher values of correlation over those with lower values of correlation. Unlike the intensity image, the correlation image enables discrimination between the signal and the background by the value of the correlation coefficient, i.e., the signal of interest assumes high value of correlation, whereas the background assumes low value of correlation. In addition this unique feature of the correlation image allows for effective post-image processing such as histogram manipulation and multithreshold display that can further improve the image contrast. A more detailed description is beyond the scope of this study and will be published elsewhere.

SUPPLEMENTAL REFERENCES

1. Sakata T, Yan Y, Marriott G (2005) Family of site-selective molecular optical switches. *J Org Chem* 70:2009–2013.

2. Gomez T, Harrigan D, Henely J, Robles E (2003) Working with *Xenopus* spinal neurons in live cell culture. *Methods Cell Biol* 71:130–154.

3. Gomez T, Robles E (2003) Imaging calcium dynamics in developing neurons. *Methods Enzymol* 361:407–422.

4. Scott EK, *et al.* (2007) Targeting neural circuitry in zebrafish using GAL4 enhancer trapping. *Nat Methods* 4:323–326.

Supplemental Figure 1

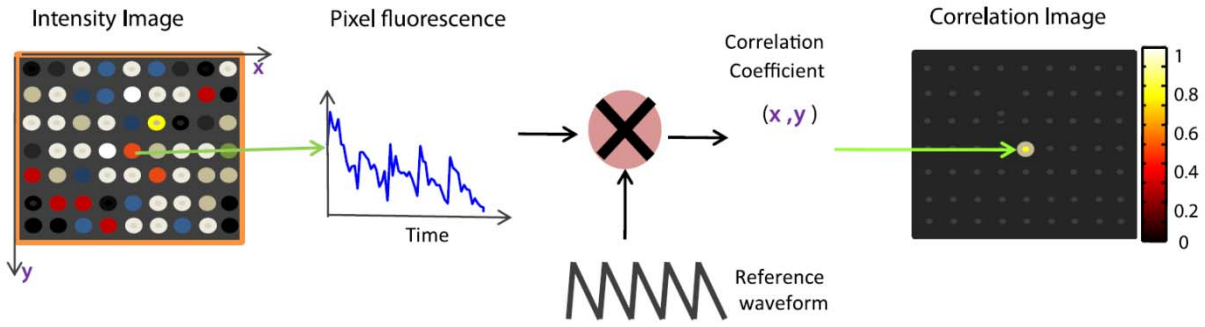

Fig. S1. Correlation imaging in OLID. To selectively amplify signals from the optical switch probes in the image field (*Left*), a cross-correlation analysis was performed between every pixel in an image field (*Left*) and a reference waveform (*Center*) to yield a correlation image (*Right*). Details are provided in *Results*.

Supplemental Figure 2

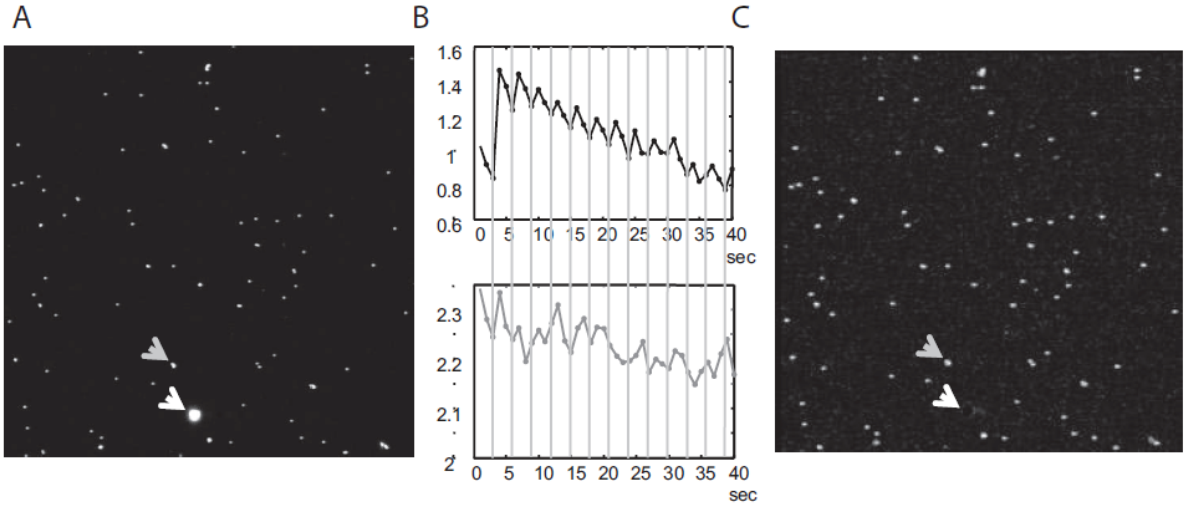

Fig. S2. OLID-enhanced images of beads bearing Dronpa in the presence of an aggregate of GFP-latex beads. (*A*) Image of fluorescence intensity from a mixture of ~80 Dronpa-latex beads and a single larger aggregate of GFP-latex beads (white arrowhead). (*B*) (*Upper*) Black trace shows the fluorescence intensity profile (arbitrary units) of the reference waveform of the optical switching of a single Dronpa-latex bead (dark-gray arrowhead in*A*) according to the train of laser scans by using 800-nm 2-photon stimulation to convert nonfluorescent *trans*-Dronpa to the fluorescent *cis*-Dronpa and 488-nm stimulation to evoke fluorescence and the reverse isomerization, as shown. (*Lower*) Gray trace shows the fluorescence intensity (arbitrary units) profile within the larger aggregate of GFP-latex beads (white arrowhead in *A*). (*C*) Image of the square of the correlation coefficient of the beads from *A* derived from 12 cycles of optical switching. Note that all of the small Dronpa beads are visible, whereas the larger GFP bead (white arrowhead in *A*) is not.

Supplemental Figure 3

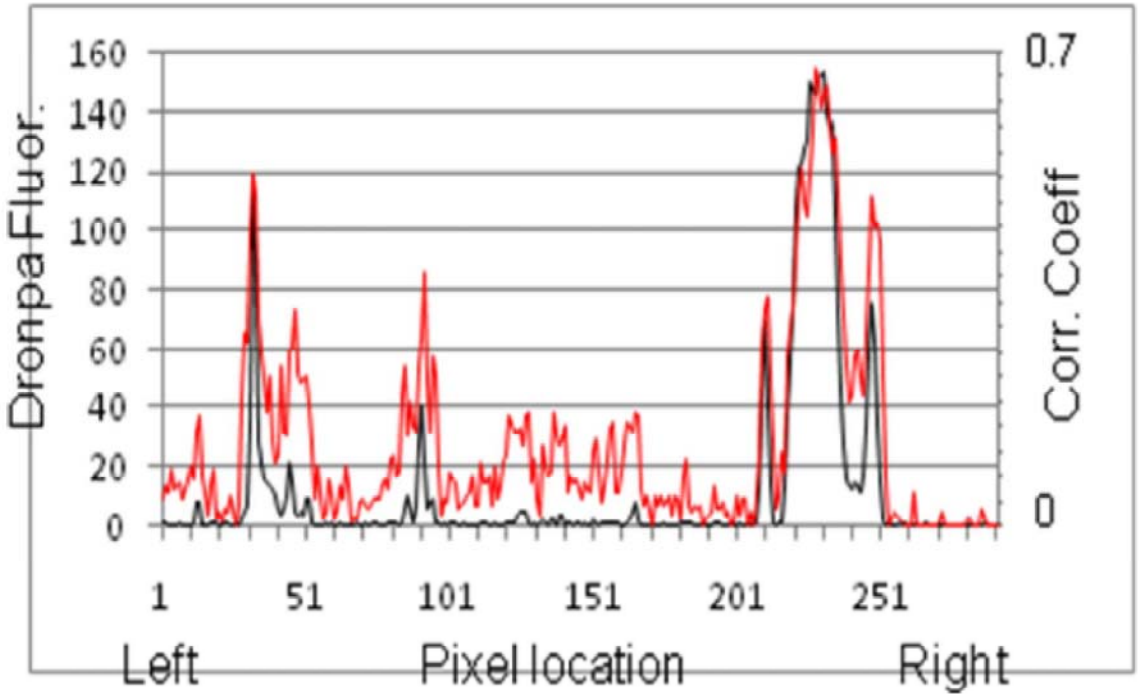

Fig. S3. Comparison of intensity and correlation images. Traces of Dronpa-actin fluorescence intensity (black, left axis) and the correlation coefficient (red, right axis) of Dronpa-actin in Fig. 4 *A* and *B* along the line defined by the yellow arrows in Fig. 4 *A* and *B*. Specific improvements to image contrast can be seen both visually (Fig. 4*A* and *B*) and in the plot (above) for pixel loci from 40 to 200 that correspond to neuronal connections. Data were extracted by using ImageJ software and analyzed by using Excel.

Supplemental Figure 4

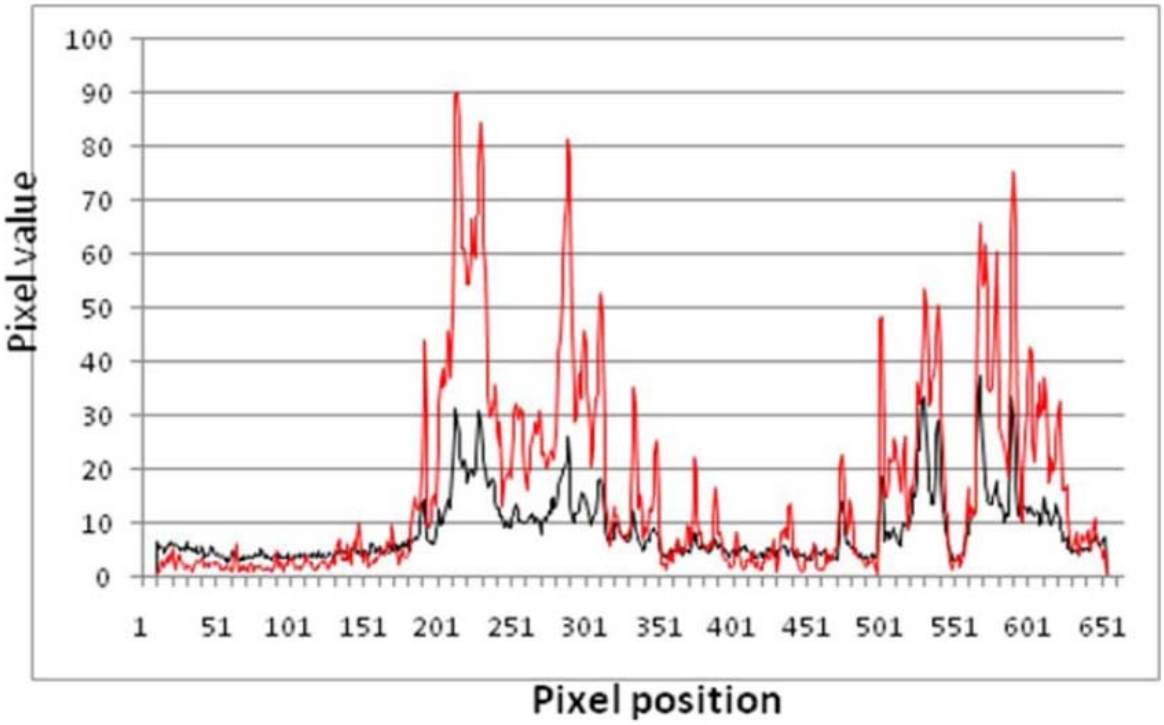

Fig. S4. Comparison of intensity and correlation images. Traces of the intensity (black, left scale) and correlation coefficient (red; scale is 0–1) of Dronpa along the line defined by the yellow arrows in Fig. 5 *D* and *E*. The signal-to-background for the intensity and correlation images were calculated for specific pixels along the trace shown in Fig. 5 *D* and *E*, choosing a region comprising only background and a Dronpa-labeled neuronal substructure. Data were extracted by using ImageJ software and analyzed by using Excel.

Chapter 3:

Screening of spinal *Gal4* enhancer trap lines for studies of CPG development and control in the zebrafish

ABSTRACT

Optogenetic tools allow for the monitoring and manipulation of neural activity in genetically-defined populations of cells non-invasively with light. A key component of this approach is the production and characterization of genetic lines that target cell populations of interest for study. Known promoters can be used to target restricted cell types, but we do not yet have an exhaustive library of promoters to cover all desired cell populations. Another way to generate driver lines that target genetically-defined populations is through enhancer trapping. In enhancer trapping, the *Gal4* transgene is randomly inserted during genomic integration nearby endogenous enhancers, each of which drives a particular expression pattern that can be screened for utility. Our lab was interested in identifying driver lines that target the spinal cord for investigation of the motor system, and collaborated with the Baier lab at the University of California, San Francisco that had performed an enhancer trap screen, to find useful spinal cord lines. Here I present the work that I did on this effort and highlight seven *Gal4* lines that are promising candidates for studies of the control and development of the spinal CPG.

INTRODUCTION

A key advantage of the optogenetic approach is that tools to monitor and manipulate neural activity can be targeted to genetically defined cell types, allowing the dissection of circuit components at the cellular level[1,2]. In contrast, calcium-sensitive or voltage-sensitive dyes can be injected into general areas of the nervous system, but will be taken up by a wide variety of cell types, requiring additional approaches to identify which cells display the observed activity. In the case of experimentally altering neural activity, pharmacology or electrophysiological methods target cells based on the receptors that they express or location in reference to the electrode, respectively. Targeting optogenetic tools to genetically-defined populations of cells provides consistent and specific interrogation of neural circuits. To dissect which cells drive the CPG in the mature circuit and which cells contribute to the development of the CPG, it is essential to have driver lines that target particular cells of interest in this circuit.

Populations of cells can be genetically targeted directly through the application of cloned endogenous promoters such as *Hb9*[3], which targets all motoneurons, or *GATA2*[4], which targets a subset of motoneurons. However, specific promoters are not known for all cells types and isolating the effective regulatory region for a promoter is not trivial. An alternative approach is to perform enhancer trapping, where a driver gene is randomly inserted into the genome, driving an expression pattern that is dependent on which endogenous enhancers or promoters it integrates nearby[5,6]. This approach allows for the random generation of novel driver patterns which can then be screened for relevance to the study at hand and used in conjunction with the flexible bipartite *UAS,Gal4* system.

The *Gal4,UAS* system is a genetic tool endogenous to yeast and commonly applied experimentally in *Drosophila* for targeting specific populations of cells[7]. More recently it has been successfully used in zebrafish[8,9]. Our lab formed a collaboration with the Baier lab at UCSF to bring the *Gal4* system and optical tools together in

zebrafish. The Baier lab developed over fifty *Gal4* lines with targeted expression in the spinal cord in an enhancer trap screen[10]. In this screen, the gene for *Gal4*, which was flanked with Tol2 transposable elements, was injected into fertilized eggs at the single cell stage, along with RNA for transposase, the enzyme that catalyzes genomic integration at Tol2 sites. Founders with expression in the nervous system were screened and stable lines created. I screened through over 30 of these stable lines to identify novel patterns that could be utilized for behavioral and developmental studies of the spinal CPG. I sought lines that 1) targeted a single homogenous population of neurons in the spinal cord, 2) had little background expression in other cell types, such as muscle, and 3) had strong expression at the developmental time point intended for experiments (17-21 hpf for developmental studies; 5 dpf for behavioral studies).

The neuronal population of the zebrafish spinal cord is comprised of sensory neurons, interneurons, and motor neurons. Transient Rohon Beard cells are the primary sensory neurons of zebrafish embryos and there are currently 13 types of interneurons described[11,12]. Zebrafish motor neurons are divided into two distinct populations: primary motor neurons (PMNs) and secondary motor neurons (SMNs). PMNs are large, few, develop early and are involved in quick, escape response movements[13,14,15]. Contrarily, SMNs are small and numerous, develop later, and are involved in more finely controlled swimming behaviors[13,14,15]. Neurons in the spinal cord, other than motoneurons, extend their axons in three different tracts: the dorsal longitudinal fasciculus (DLF) which lies dorsal in the spinal cord and is most associated with sensory functions; the ventral longitudinal fasciculus (VLF), which run more ventral and contains a large number of descending axons from spinal interneurons; and the medial longitudinal fasciculus (MLF) which runs along the ventral medial portion of the spinal cord and contains descending axons from the hindbrain[16]. Within the spinal cord, a *Gal4* enhancer trap line can target any subset of these neurons, as well as glial cells.

To determine the cells targeted, I used confocal imaging to analyze the morphology of targeted cells and matched them with known anatomy[13,14,11,12]. The *Gal4* positive fish contain a transgene for the photoconvertible protein *Kaede* under the *UAS* promoter[10]. This green fluorescent protein is expressed throughout the cytoplasm of *Gal4* positive cells and allows for the easy recognition of transgenic lines and visualization of their morphology. The morphology of individual cells can be further characterized for prospective lines using single cell imaging and immunohistochemistry (see Chapter 4 and 5)[17,18].

RESULTS

This section highlights the morphological characterization of seven lines that my screening identified as promising candidate lines for studies of the spinal CPG. Indeed one of these lines, *Gal4*^{s1003t}, allowed our lab to genetically isolate Kolmer-Agduhr interneurons in the spinal cord and characterize their function in relation to the spinal CPG (see Chapter 4)[17]. Additional experiments are being performed with other lines.

Gal4 lines targeting motoneurons and ventral interneurons

The motor system of the spinal cord is localized to the ventral portion of the cord and contains interneurons as well as motoneurons[19]. I identified a line, the *Gal4*^{s1089t} line, which targets ventral interneurons as well as motoneurons (Fig. 1). Expression in this line is strong and consistent along the rostral-caudal axis, making it ideal for the robust expression of optogenetic tools in CPG-related neurons (Fig. 1A). The line also targets neurons in the hindbrain which provides supraspinal activation of the spinal CPG during forward swimming and escape behaviors (Fig. 1E, F)[20,21]. Expression is absent in the dorsal hindbrain, suggesting again that the line is largely restricted to ventral cells of the motor system. Using the *Gal4*^{s1089t} line, one could for example express the genetically-encoded voltage indicator Arch(D95N)[22] and image patterns of electrical activity across the population of motor system interneurons and motoneurons during particular behaviors like spontaneous forward swimming or escape, in a paralyzed fictive preparation[21]. High imaging speed would be required to detect high frequency voltage changes, making it challenging to image the full 3D pattern for a given time series. Different planes of the targeted pattern, however, could be imaged in sequential trials.

Gal4 lines targeting interneurons only

I identified two *Gal4* lines that each target homogenous populations of ventral spinal interneurons associated with the motor system: the *Gal4*^{s1011t} and *Gal4*^{s1003t} lines, as well as a line that broadly targets interneurons, the *Gal4*^{s1048t} line.

The *Gal4*^{s1011t} line targets a sparse population of cells with somas in the mid to mid-ventral spinal cord, as well as a fraction of muscle cells (Fig. 2A). The cells in the spinal cord have a tear drop shape and axons that extend at first ventrally and then descend laterally in the cord in the area associated with the VLF (Fig. 2B-D). These cells also sometimes have thinner axon branches that ascend in the cord, traveling in the more dorsal DLF (Fig. 2E). All of these characteristics are consistent with these cells being glutamatergic CiD interneurons[12]. A homologue of this cell type was first investigated in the goldfish where it was shown to be involved in the escape response[23]. This excitatory interneuron receives monosynaptic input from the Mauthner cell and projects directly to the motoneurons providing the intermediately step in the di-synaptic circuit between the sensory-activated Mauthner cell and the motoneurons. This *Gal4* line would, therefore, be applicable to studies of the escape circuit and the role that this intermediary interneuron plays. The line also targets muscle cells, which could be problematic in studies of behavior if light-gated ion channels were expressed in this line and activated by global illumination, directly causing contraction of the muscles. However, the muscle cell expression is minimal around the rostral parts of the cord (Fig. 2A), so targeted light application using a device such as a digital micro-mirror device could activate the CiD interneurons, while avoiding the muscle cells.

The *Gal4*^{s1003t} line also targets a homogeneous population of cells with cell bodies in the ventral half of the cord (Fig. 3A). High magnification imaging of these cells revealed “tuft-like” protrusions that came off of the dorsal or ventral part of the cell and projected towards the midline of the cord, where the central canal runs (Fig. 3B, e.g. *arrows*). Cell bodies resided either dorsal or ventral of the location of the canal. These

cells also had punctate processes that ran in the VLF, indicating the presence of synaptic contacts (Fig. 3C, e.g. *arrows*). These characteristics (as well as additional single cell imaging and immunohistochemistry data, Chapter 4) pointed to these cells being cerebral spinal fluid-contacting Kolmer-Agduhr interneurons, a cell type whose morphology has been known for over 75 years, but whose function was previously unknown[24]. Using this line, optogenetic tools could be expressed in these cells using the *UAS,Gal4* system and activated with light to investigate their function, which is precisely what I, in collaboration with others, did in Chapter 4[17].

I also identified a line, the *Gal4*^{s1048t} line, which targets a broad rather than homogenous population of interneurons including both ventral motor-associated interneurons and dorsal sensory-associated interneurons (Fig. 4). Though this line targets many neurons types, it does not target motoneurons or Rohon Beard sensory neurons, as no neural processes can be seen extending out of the spinal cord (Fig. 4C-D). Advantageous to this line is the absence of strong background expression in muscle cells and an even expression of *Gal4* along the rostral-caudal and dorsal-ventral axis in the spinal cord. This line could be used for experiments such as imaging the activity of interneuron populations during the escape response using the genetically-encoded calcium indicator GCaMP[25,26] or activating different components of the spinal cord along the rostral-caudal axis using light-gated ion channels like LiGluR[27,28] or ChR2[29] with targeted light to investigate the recruitment of the CPG and effects on swimming kinematics.

Gal4 lines targeting sensory neurons

I also identified a line, the *Gal4*^{s1049t} line, which targets sensory neurons in the nervous system (Fig. 5A,B). In the spinal cord, this line targets only Rohon Beard primary somatosensory neurons (Fig. 5C,D). Their large cell bodies that sit at the most dorsal point in the cord had high levels of expression, and processes extending from these cells and out of the spinal cord towards the skin were observed. Occasionally expression in dorsal root ganglion neurons was also observed lateral to the cord (Fig. 5E). This line also targets sensory ganglia in the head, including the trigeminal ganglia which mediate somatosensation of the head, as well as cells in the olfactory bulb (Fig. 5F). It is very likely the *Gal4* insert for this line is localized near an enhancer or promoter for a sensory receptor or its associated machinery. Expressing GCaMP in this line, one could look at patterns of neural activity elicited in primary sensory neurons during the presentation of different stimuli on the skin. One could also express a light-gated ion channel such as LiGluR[27,28] or ChR2[29] in these cells and stimulate fractions of the population to investigate circuit components required for sensory-evoked behaviors.

Gal4 lines targeting neurons and glial cells

Glial cells are cells in the nervous system that have traditionally been thought of merely as support cells for neurons. Recent evidence, however, has suggested that they may play an essential role in neural signaling, directly influencing the function of neural circuits[30,31]. Preliminary results in our lab have suggested that the activation of glial cells in the spinal cord using a glial specific enhancer trap line and the light-gated glutamate

receptor LiGluR elicits the activation of the spinal CPG and forward swimming behavior in the zebrafish larvae (Conner, Wyart et al., unpublished results). Driver lines targeting neurons and glia together in the spinal cord would allow for an investigation of the interplay between neural and glial signaling in this network. To morphologically separate glial cells from neurons in a single preparation, however, these lines must be relatively sparse. In my screening, I identified two *Gal4* enhancer trap lines that sparsely target subpopulations of neurons and glia, *Gal4*^{s1051t} and *Gal4*^{s1056t}.

The *Gal4*^{s1051t} line targets cells in the spinal cord spanning the whole rostral-caudal axis (Fig. 6). Analysis of cell morphology shows that this line targets interneurons in the spinal cord, motoneurons and glial cells that surround the ventral axons in the spinal cord (Fig. 6B-E). The absence of motoneuron expression in some somites and the gaps of expression in ventral glial cells suggest this line is stochastically expressed in a random subpopulation of certain cell types. This type of variegated expression is plausible and common in enhancer trap lines, as some genes express stochastically in genetically identical cells[32]. The *Gal4*^{s1056t} line also targets motoneurons, interneurons and glial cells in the spinal cord (Fig. 7). Expression, however, is much sparser in the rostral cord than in the *Gal4*^{s1051t} line, and expression is targeted to glial cells in the dorsal rather than ventral cord (Fig. A, E-F). Expression in this line is similarly variegated and stochastically expressed within these populations as few cells are targeted and cells where we know the expected number per somite (motoneurons) are targeted in relatively few numbers. This sparse expression however is advantageous for experiments where activity-altering tools can be expressed in the whole population, but spatial light targeting can restrict activation of these tools to individual cells, while other cells in the line are observed with imaging. Cell types can also be distinguished in live embryos and larvae by morphology, allowing for *in vivo* experiments looking at the relationship between spinal neurons and spinal glial cells.

DISCUSSION

Here I have characterized the expression pattern of a selection of *Gal4* enhancer trapped lines that are promising for studies of the control and development of the spinal CPG. These lines include the *Gal4*^{s1089t} line which strongly targets transgene expression to ventral interneurons associated with the motor system in the spinal cord and hindbrain, as well as motoneurons themselves. I also identified three lines with restricted expression in spinal cord interneurons: the *Gal4*^{s1011t} line which targets CiD interneurons, the *Gal4*^{s1003t} line which targets Kolmer-Agduhr cells, and the *Gal4*^{s1048t} line which targets a broad population of interneurons, without exhibiting expression in motoneurons or sensory neurons. I additionally found a line, the *Gal4*^{s1049t} line, which specifically targets sensory neurons in the spinal cord and brain, including Rohon Beard cells and trigeminal neurons. Finally, I identified two lines, the *Gal4*^{s1051t} and *Gal4*^{s1056t}, which sparsely target motoneurons and spinal interneurons and subclasses of glial cells.

These lines could be used to express indicators of neural activity such as GCaMP[25,26] in these defined cell populations to image activity during development of the CPG or fictive swimming (when the animal is paralyzed by blocking the

neuromuscular junction, but neural circuits are still active as usual)[21]. These lines could also be used to target light-gated ion channels or pumps to these cells types to activate or inhibit the *Gal4* population and observe resulting effects on behavior. It is also possible to use *Gal4* driver lines in conjunction with lines using specific promoters to drive imaging or activity-altering light-based tools. In this scenario, for example, an imaging tool like GCaMP could be expressed in one population of cells using a *Gal4* driver line, while a light-gated channel like LiGluR is expressed in another using a specific driver. In this case, activity in one group of cells can be altered while downstream effects are observed in a genetically different population. *Gal4* and *UAS* lines can also be used in combination with other expression systems like LexPR/LexA[33] and Cre/LoxP[34,35] which have been used successfully in zebrafish.

This one enhancer trap screen produced several candidate lines for study of the CPG as well as other investigations in the nervous system. Since enhancer trapping however depends on the chance insertion of *Gal4* into the genome, additional screens are advantageous as each screen is far from exhaustive and new screens will provide new genetic patterns that will increase the range of experiments that can be performed and cells types that can be isolated. Indeed, other enhancer trap screens have provided additional arrays of genetically encoded expression patterns that have been utilized to learn about novel functions of certain cell types[36,37,38,39], and technical improvements have been made in the expression system as applied to zebrafish[40]. The availability of libraries of genetic tools to target different populations of cells in the nervous system of zebrafish, coupled with the development of novel and improved genetically-encoded tools to manipulate and image neural activity and morphology with light, will no doubt enable more controlled and more specific experiments for the study of the neural circuits that control behavior and their genesis during development.

METHODS

Gal4$^{(X)}$/UAS:Kaede adults were crossed with TL wildtype adults and progeny were raised in embryo medium at 28.5°C until imaging. 2-6 day old progeny which carried both transgenes (displaying green fluorescence) were screened for imaging using a fluorescent stereoscope (Leica). All imaging was performed on live larvae mounted in 2% low-melting point agarose (Invitrogen) and anaesthetized with 0.02% MS-222 (Sigma) to eliminate muscle contractions during image acquisition. Imaging was performed on a Zeiss or Olympus upright confocal microscope, using 10x, 40x or 63x water-dipping objectives.

Figure 1

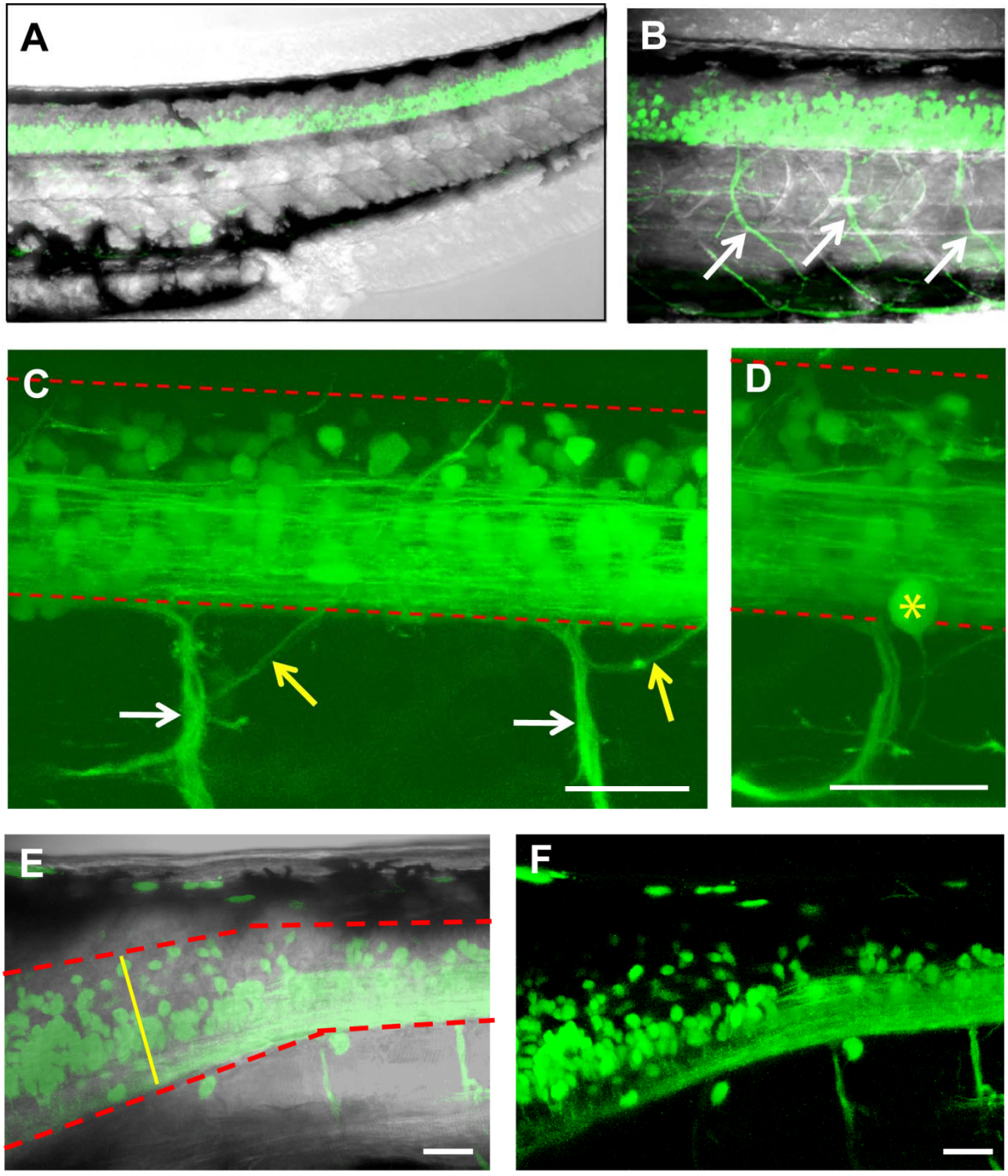

Figure 1. *Gal4*^{s1089t} targets motoneurons and ventral spinal interneurons. (A) Low magnification view of laterally mounted 5 dpf *Gal4*^{s1089t}*/UAS:Kaede* fish shows even expression in spinal cord along the rostral-caudal axis with very little expression outside of the spinal cord. (B) Axons extending out of the cord at the ventral roots (*arrows*) indicate expressing in motoneurons. (C) Higher magnification view shows densest expression in the ventral and mid-cord with little expression in the dorsal cord and strong expression in motoneuron axons extending ventrally (*white arrows*) and dorsally (*yellow arrows*) to the muscle cells. (D) Occasionally expression in DRG cells residing lateral to the cord was observe (*asterisk*). (E,F) Images taken more rostrally with (E) and without (F) bright field overlay shows expression is also extended into the hindbrain, with expression remaining densest in the ventral and mid-sections. Yellow line marks spinal cord/hindbrain border. The spinal cord is outlined in red in select images, with the rostral direction to the left and dorsal up. Scale bars, 25 µm.

Figure 2

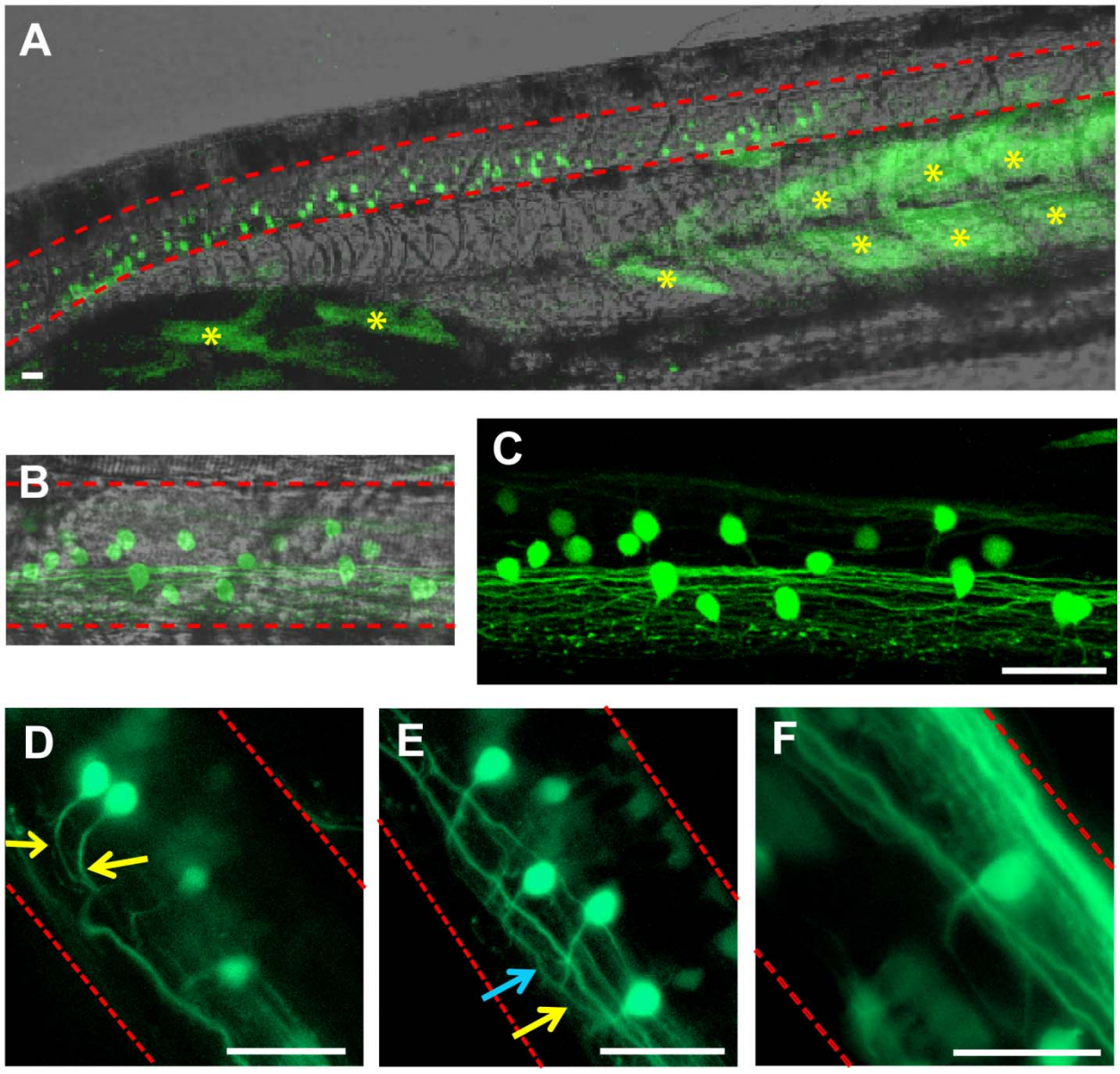

Figure 2. *Gal4*^{s1011t} targets Circumferential Descending (CiD) interneurons. (A) Low magnification view of laterally mounted 6 dpf *Gal4*^{s1011t}*/UAS:Kaede* larvae shows targeting of a sparse number of cells in the mid to ventral region of the spinal cord, with denser expression in rostral regions, as well as expression in muscle cells (*asterisk*s). (B,C) Higher magnification shows round, teardrop-shaped cell bodies with longitudinal processes in the mid to ventral cord (VLF), characteristic of CiD interneurons[11,12]. (D) Imaging in a single plan shows clearly axons from two neurons (*arrows*) projecting at first ventrally, then caudally. (E) In some cells, axons can be seen that have descending (*yellow arrow*) as well as ascending (*blue arrow*) components, characteristic of the CiDs. (F) Imaging more medially reveals these ascending processes running in the DLF in the dorsal part of the cord. In all images, the spinal cord is outlined in red, with the rostral direction to the left and dorsal up. Scale bars, 25 µm.

Figure 3

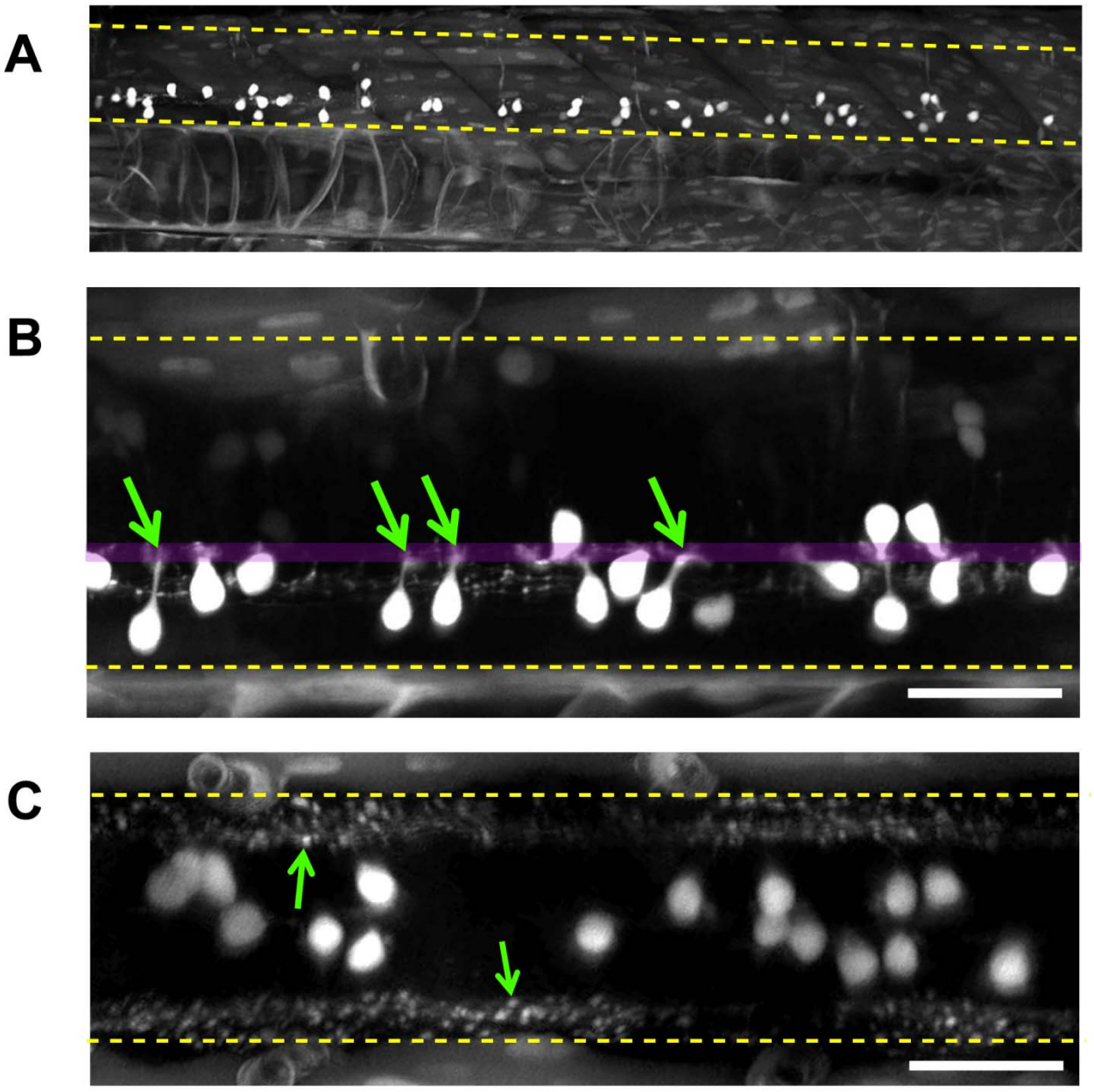

Figure 3. *Gal4*^{s1003t} targets Kolmer-Agduhr (KA) cerebral spinal fluid-contacting interneurons. (A) Low and (B) high magnification views of *Gal4*^{s1003t}*/UAS:Kaede* 5dpf larvae, mounted laterally, showing sparse cell bodies in the ventral half of the spinal cord. Faint expression of kaede is also observed in cells of the notochord and musculature. (B) Cell bodies have ciliated “tufts” (*e.g. arrow*) that project along a single line down the spinal cord where the central canal resides (*estimated location in purple*). Cell bodies are both dorsal and ventral to these ciliated projections. (C) Dorsal view shows medial location of cell bodies with processes located laterally in the spinal cord. Puncta are seen along these processes (e.g. *arrows*) indicating synapses at these locations. The spinal cord is outlined in yellow, with the rostral direction to the left and dorsal up. Scale bars, 25 μm.

Figure 4

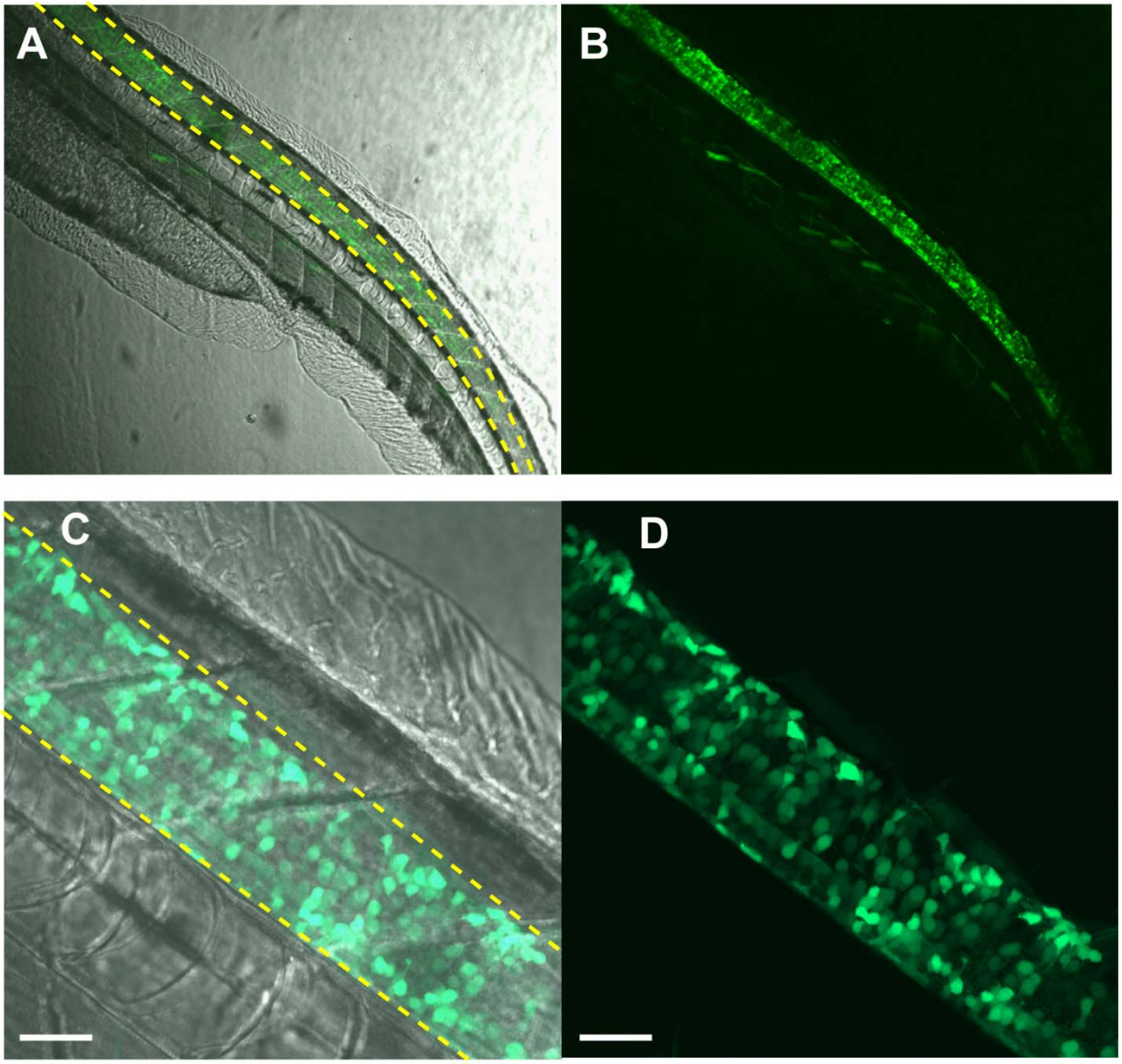

Figure 4. *Gal4*^{s1048t} targets a broad population of spinal interneurons. (A,B) Low magnification view of laterally mounted 3 dpf *Gal4*^{s1048t}*/UAS:Kaede* larvae spinal cord expression with (A) and without (B) bright field image overlay shows even expression in cells spanning the rostral-caudal and dorsal-ventral axis. (C,D) High magnification with (C) and without (D) bright field image overlay shows expression in cell bodies within the spinal cord but no processes extending out of the cord, indicating a lack of expression in motoneurons and sensory neurons. The spinal cord is outlined in yellow, with the rostral direction to the left and dorsal up. Scale bars, 25 μm.

Figure 5

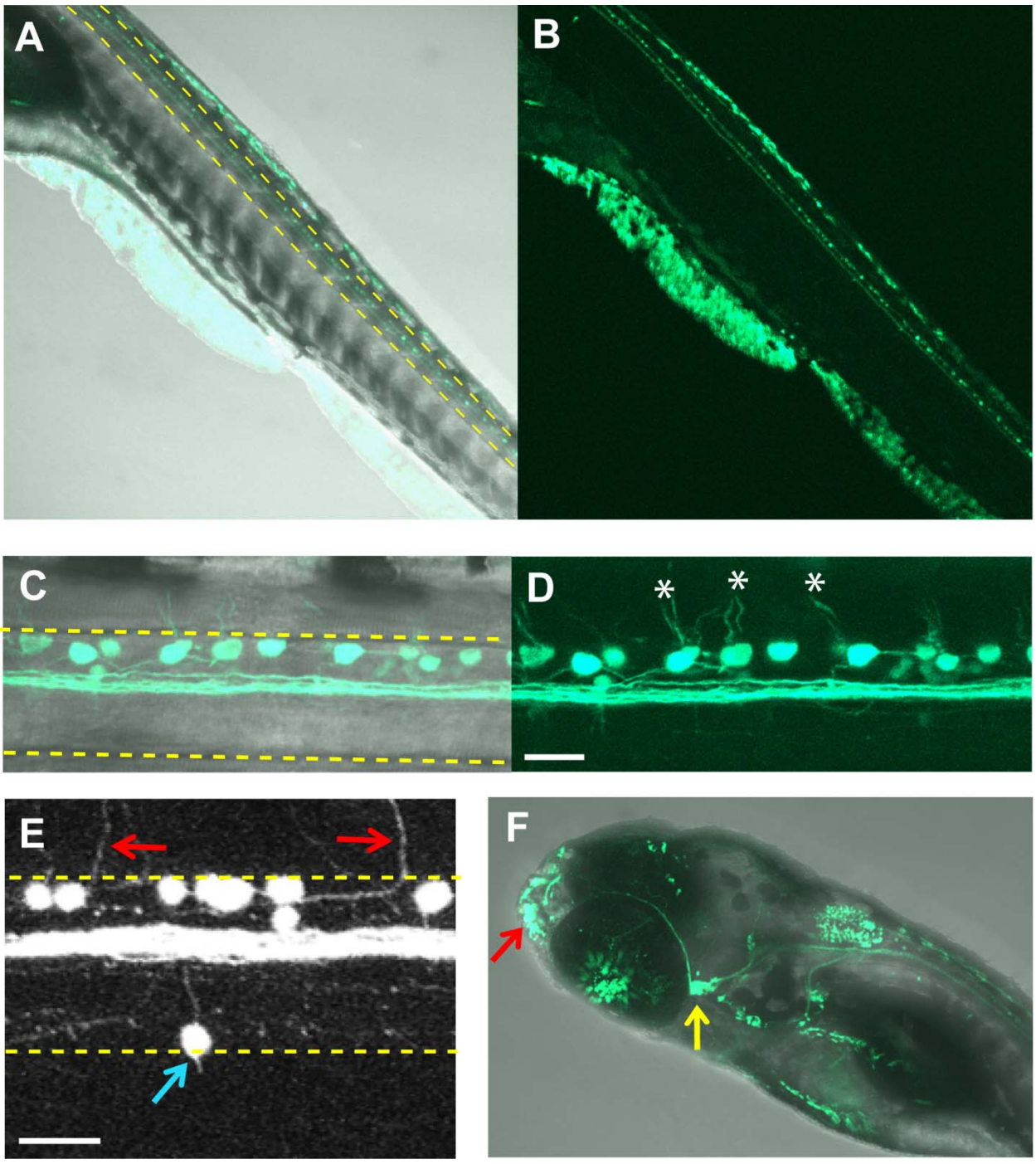

Figure 5. *Gal4*^{s1049t} targets primary somatosensory neurons in the head and spinal cord. (A,B) Low magnification lateral view of *Gal4*^{s1049t}*/UAS:Kaede* 5dpf larval spinal cord with (A) and without (B) bright field image overlay shows expression along whole length of spinal cord, as well as background expression in the skin and digestive system. (C,D) Higher magnification views with (C) and without (D) bright field overlay reveals expression in Rohon Beard cells, which have characteristic large, oval-shaped cell bodies in dorsal most part of cord with afferent processes extending towards skin (*asterisks*). Rohon Beard processes running rostral and caudal in the dorsal longitudinal fasciculus can also be seen here. (E) Afferent processes of Rohon Beards are clearly seen exiting dorsal cord (*red arrows*) and a primary sensory dorsal root ganglion cell (*blue arrow*), which replace Rohon Beard cells as the animal matures, sits just lateral to the cord. (F) In the head, this line also targets other sensory neurons, including those in the olfactory bulb (*red arrow*) and trigeminal ganglion (*yellow arrow*). The spinal cord is outlined in yellow, with the rostral direction to the left and dorsal up. Scale bars, 25 µm.

Figure 6

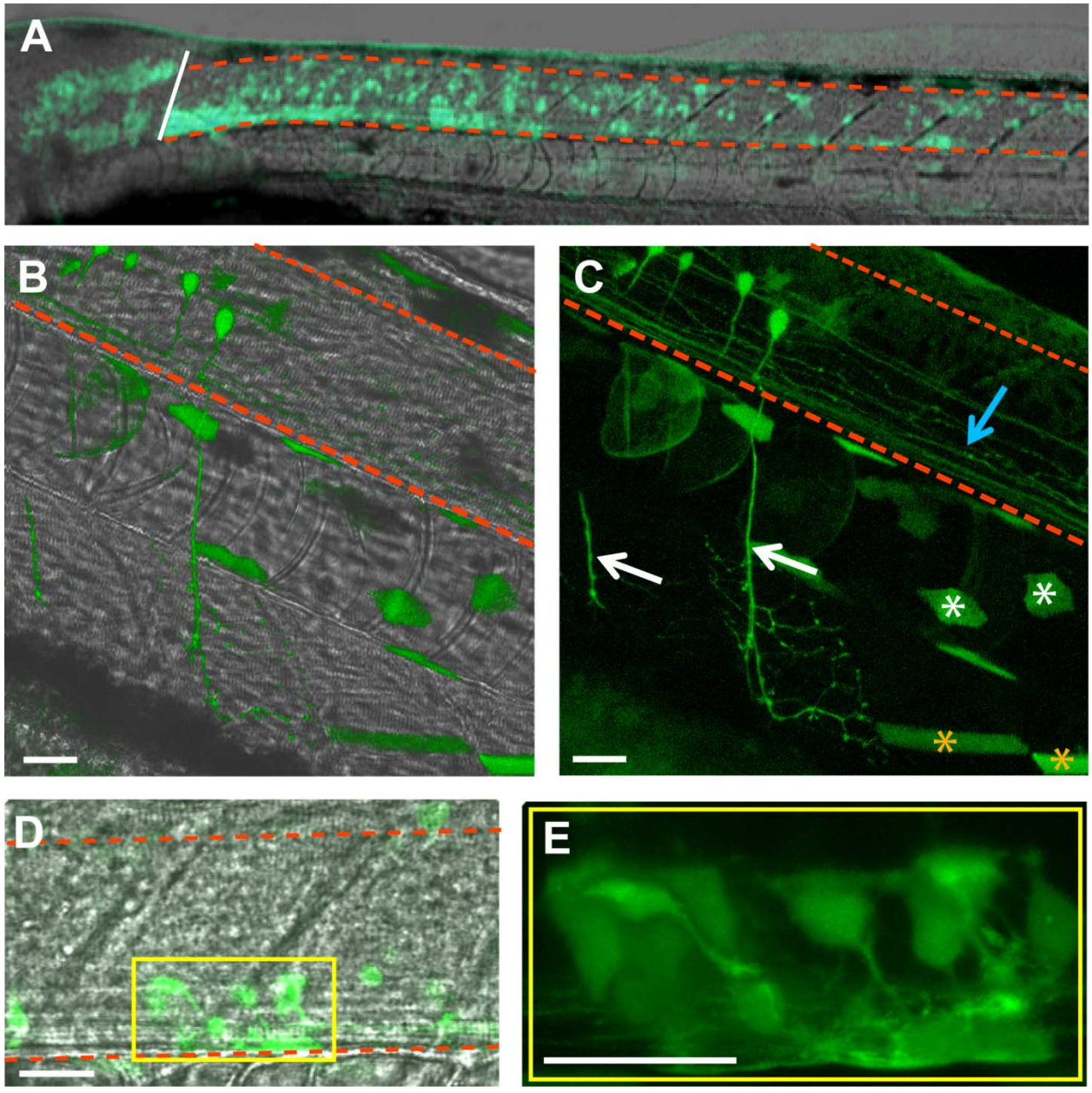

Figure 6. *Gal4*^{s1051t} targets neurons and glial cells in the spinal cord. (A) Low magnification view of a 2dpf *Gal4*^{s1051t}*/UAS:Kaede* fish with expression focused in the rostral spinal cord, though also extending more caudally and also present in the hindbrain (white line marks spinal cord/hindbrain boundary). (B,C) Higher magnification view with (B) and without (C) bright field image overlay shows axons running longitudinally in the ventral cord (*blue arrow*) indicating expression in interneurons, and axons extending out of the cord at the ventral root (*white arrows*) revealing expression in motoneurons. Expression is also seen in a fraction of cells in the notochord (*white asterisks*) and in some muscle cells (*orange asterisks*). (D) Expression is also present in clusters of cells surrounding the axon bundles in the ventral spinal cord. (E) Zooming in on the yellow box reveals these cells' tapered and irregularly shaped processes, indicating they are glial cells rather than neurons. Expression in clusters of these cells, as well as sparse expression of motoneurons, interneurons, and muscle and notochord indicates this line is stochastic and variegated. The spinal cord is outlined in red, with the rostral direction to the left and dorsal up. Scale bars, 25 μm.

Figure 7

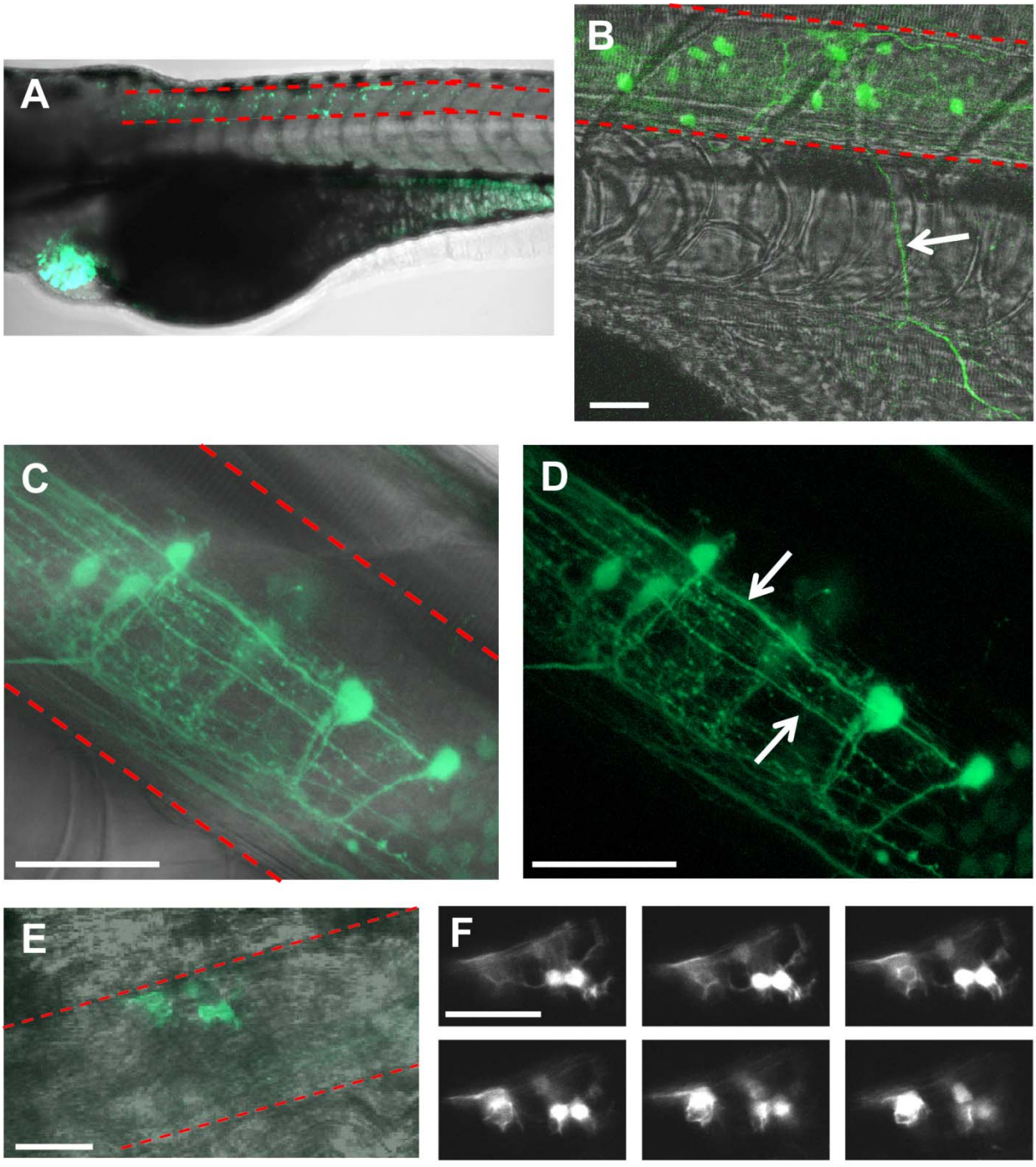

Figure 7. *Gal4*^{s1056t} targets neurons and glia in the rostral spinal cord. (A) Low magnification view of *Gal4*^{s1056t}*/UAS:Kaede* 3 dpf larvae shows sparse expression in the rostral spinal cord as well as expression in the heart and digestive tract. (B-D) Higher magnification of rostral cord shows cell bodies in the middle of the cord with processes extending out of the cord (B, *arrow*), indicating the presence of motoneuron expression, and processes extending longitudinally in the cord (D, e.g. *arrows*), indicating expression in interneurons. (E) Cells were also found in the rostral cord that exhibited non-neuronal morphologies. (F) A *z-stack* sequence of images shows the cells in (E) and their “ghost-like” shape suggesting they are glial cells. The spinal cord is outlined in red, with the rostral direction to the left and dorsal up. Scale bars, 25 μm.

REFERENCES

1. McLean DL, Fetcho JR. Using imaging and genetics in zebrafish to study developing spinal circuits in vivo. *Dev Neurobiol*. 2008;68(6):817-834.

2. Szobota S, Isacoff EY. Optical control of neuronal activity. *Annu Rev Biophys*. 2010;39:329-348.

3. Nakano T, Windrem M, Zappavigna V, Goldman SA. Identification of a conserved 125 base-pair Hb9 enhancer that specifies gene expression to spinal motor neurons. *Dev. Biol*. 2005;283(2):474-485.

4. Meng A, Tang H, Ong BA, Farrell MJ, Lin S. Promoter analysis in living zebrafish embryos identifies a cis-acting motif required for neuronal expression of GATA-2. *Proc. Natl. Acad. Sci. U.S.A.* 1997;94(12):6267-6272.

5. Ellingsen S, Laplante MA, König M, et al. Large-scale enhancer detection in the zebrafish genome. *Development*. 2005;132(17):3799-3811.

6. Kawakami K, Takeda H, Kawakami N, et al. A transposon-mediated gene trap approach identifies developmentally regulated genes in zebrafish. *Dev. Cell*. 2004;7(1):133-144.

7. Brand AH, Perrimon N. Targeted gene expression as a means of altering cell fates and generating dominant phenotypes. *Development*. 1993;118(2):401-415.

8. Inbal A, Topczewski J, Solnica-Krezel L. Targeted gene expression in the zebrafish prechordal plate. *Genesis*. 2006;44(12):584-588.

9. Halpern ME, Rhee J, Goll MG, et al. Gal4/UAS transgenic tools and their application to zebrafish. *Zebrafish*. 2008;5(2):97-110.

10. Scott EK, Mason L, Arrenberg AB, et al. Targeting neural circuitry in zebrafish using GAL4 enhancer trapping. *Nat. Methods*. 2007;4(4):323-326.

11. Bernhardt RR, Chitnis AB, Lindamer L, Kuwada JY. Identification of spinal neurons in the embryonic and larval zebrafish. *J. Comp. Neurol*. 1990;302(3):603-616.

12. Hale ME, Ritter DA, Fetcho JR. A confocal study of spinal interneurons in living larval zebrafish. *J. Comp. Neurol*. 2001;437(1):1-16.

13. Myers PZ, Eisen JS, Westerfield M. Development and axonal outgrowth of identified motoneurons in the zebrafish. *J. Neurosci*. 1986;6(8):2278-2289.

14. Westerfield M, McMurray JV, Eisen JS. Identified motoneurons and their innervation of axial muscles in the zebrafish. *J. Neurosci.* 1986;6(8):2267-2277.

15. Liu DW, Westerfield M. Function of identified motoneurones and co-ordination of primary and secondary motor systems during zebra fish swimming. *J. Physiol. (Lond.)*. 1988;403:73-89.

16. Kuwada JY, Bernhardt RR, Nguyen N. Development of spinal neurons and tracts in the zebrafish embryo. *J. Comp. Neurol*. 1990;302(3):617-628.

17. Wyart C, Del Bene F, Warp E, et al. Optogenetic dissection of a behavioural module in the vertebrate spinal cord. *Nature*. 2009;461(7262):407-410.

18. Warp E, Agarwal G, Wyart C, et al. Emergence of patterned activity in the developing zebrafish spinal cord. *Curr. Biol.* 2012;22(2):93-102.

19. Drapeau P, Saint-Amant L, Buss RR, et al. Development of the locomotor network in zebrafish. *Prog. Neurobiol*. 2002;68(2):85-111.

20. Deliagina TG, Zelenin PV, Orlovsky GN. Encoding and decoding of reticulospinal commands. *Brain Res. Brain Res. Rev*. 2002;40(1-3):166-177.

21. Masino MA, Fetcho JR. Fictive swimming motor patterns in wild type and mutant larval zebrafish. *J. Neurophysiol*. 2005;93(6):3177-3188.

22. Kralj JM, Douglass AD, Hochbaum DR, Maclaurin D, Cohen AE. Optical recording of action potentials in mammalian neurons using a microbial rhodopsin. *Nat. Methods*. 2011;9(1):90-95.

23. Fetcho JR, Faber DS. Identification of motoneurons and interneurons in the spinal network for escapes initiated by the mauthner cell in goldfish. *J. Neurosci*. 1988;8(11):4192-4213.

24. Dale N, Roberts A, Ottersen OP, Storm-Mathisen J. The morphology and distribution of “Kolmer-Agduhr cells”, a class of cerebrospinal-fluid-contacting neurons revealed in the frog embryo spinal cord by GABA immunocytochemistry. *Proc. R. Soc. Lond., B, Biol. Sci.* 1987;232(1267):193-203.

25. Nakai J, Ohkura M, Imoto K. A high signal-to-noise Ca(2+) probe composed of a single green fluorescent protein. *Nat. Biotechnol*. 2001;19(2):137-141.

26. Tian L, Hires SA, Mao T, et al. Imaging neural activity in worms, flies and mice with improved GCaMP calcium indicators. *Nat. Methods*. 2009;6(12):875-881.

27. Volgraf M, Gorostiza P, Numano R, et al. Allosteric control of an ionotropic glutamate receptor with an optical switch. *Nat. Chem. Biol*. 2006;2(1):47-52.

28. Szobota S, Gorostiza P, Del Bene F, et al. Remote control of neuronal activity with a light-gated glutamate receptor. *Neuron*. 2007;54(4):535-545.

29. Boyden ES, Zhang F, Bamberg E, Nagel G, Deisseroth K. Millisecond-timescale, genetically targeted optical control of neural activity. *Nat. Neurosci*. 2005;8(9):1263-1268.

30. Barres BA. The mystery and magic of glia: a perspective on their roles in health and disease. *Neuron*. 2008;60(3):430-440.

31. Perea G, Navarrete M, Araque A. Tripartite synapses: astrocytes process and control synaptic information. *Trends Neurosci.* 2009;32(8):421-431.

32. Elowitz MB, Levine AJ, Siggia ED, Swain PS. Stochastic Gene Expression in a Single Cell. *Science*. 2002;297(5584):1183 -1186.

33. Emelyanov A, Parinov S. Mifepristone-inducible LexPR system to drive and control gene expression in transgenic zebrafish. *Dev. Biol.* 2008;320(1):113-121.

34. Langenau DM, Feng H, Berghmans S, et al. Cre/lox-regulated transgenic zebrafish model with conditional myc-induced T cell acute lymphoblastic leukemia. *Proc. Natl. Acad. Sci. U.S.A.* 2005;102(17):6068-6073.

35. Thummel R, Burket CT, Brewer JL, et al. Cre-mediated site-specific recombination in zebrafish embryos. *Dev. Dyn.* 2005;233(4):1366-1377.

36. Ogura E, Okuda Y, Kondoh H, Kamachi Y. Adaptation of GAL4 activators for GAL4 enhancer trapping in zebrafish. *Dev. Dyn.* 2009;238(3):641-655.

37. Zhao X-F, Ellingsen S, Fjose A. Labelling and targeted ablation of specific bipolar cell types in the zebrafish retina. *BMC Neurosci*. 2009;10:107.

38. Kawakami K, Abe G, Asada T, et al. zTrap: zebrafish gene trap and enhancer trap database. *BMC Dev. Biol.* 2010;10:105.

39. Baier H, Scott EK. Genetic and optical targeting of neural circuits and behavior--zebrafish in the spotlight. *Curr. Opin. Neurobiol*. 2009;19(5):553-560.

40. Akitake CM, Macurak M, Halpern ME, Goll MG. Transgenerational analysis of transcriptional silencing in zebrafish. *Dev. Biol.* 2011;352(2):191-201.

Chapter 4:

Optogenetic dissection of a behavioural module in the vertebrate spinal cord

This work has been published in the following article and is reprinted in full with permission*:*

Wyart C, Del Bene F, Warp E, Scott EK, Trauner D, Baier H, Isacoff EY, “Optogenetic dissection of a behavioural module in the vertebrate spinal cord”, *Nature*, Sep 17, 2009.

The *Gal4*^{s1003t} line characterized in my *Gal4* screening (Chapter 3) was used for behavioral studies in this work to identify the previously unknown function of the cell type targeted in this line. For this work, I additionally participated in the single cell imaging of the *Gal4*^{s1003t} line using *BGUG* genetics (Figure 2) which identified this line to contain cerebral spinal fluid-contacting Kolmer-Agduhr neurons, which were found to provide a positive drive to the spinal CPG.

ABSTRACT

Locomotion relies on neural networks called central pattern generators (CPGs) that generate periodic motor commands for rhythmic movements[1]. In vertebrates, the excitatory synaptic drive for inducing the spinal CPG can originate from either supraspinal glutamatergic inputs or from within the spinal cord[2, 3]. Here we identify a spinal input to the CPG that drives spontaneous locomotion using a combination of intersectional gene expression and optogenetics[4] in zebrafish larvae. The photo-stimulation of one specific cell type was sufficient to induce a symmetrical tail beating sequence that mimics spontaneous slow forward swimming. This neuron is the Kolmer–Agduhr cell[5], which extends cilia into the central cerebrospinal-fluid-containing canal of the spinal cord and has an ipsilateral ascending axon that terminates in a series of consecutive segments[6]. Genetically silencing Kolmer–Agduhr cells reduced the frequency of spontaneous free swimming, indicating that activity of Kolmer–Agduhr cells provides necessary tone for spontaneous forward swimming. Kolmer–Agduhr cells have been known for over 75 years, but their function has been mysterious. Our results reveal that during early development in zebrafish these cells provide a positive drive to the spinal CPG for spontaneous locomotion.

RESULTS AND DISCUSSION

We searched for novel spinal neurons that trigger the CPG in the zebrafish larva by using 'intersectional optogenetics', a combination of transgene expression in specific cell types[7] and genetic tools for manipulating neuronal activity with light[4]. The light-gated channel LiGluR[8, 9] was selectively expressed in distinct subsets of spinal cord neurons by crossing transgenic animals carrying *UAS:LiGluR*[10] with a series of fish lines[11] that express GAL4, the transcription factor that activates the UAS promoter, in distinct cellular patterns. We looked for common behavioural outcomes induced by light stimulation in lines with partly overlapping expression patterns that could be attributed to the activity of a common cell type (Supplementary Fig. 1).

Five-day-old zebrafish larvae exhibit spontaneous forward slow swims[12]. These occur in brief bursts, with each burst consisting of a series of symmetrical, dampening left–right oscillations (Fig. 1a). We chose several *Gal4* transgenic lines to drive expression of LiGluR in different subsets of spinal neurons, and asked whether optical activation of these neurons elicits a forward swim-like behaviour. We first tested the *Gal4*^{s1020t} line, which labels a heterogeneous population of ventral spinal neurons. When crossed to *UAS:LiGluR* and labelled with the chemical photoswitch MAG1 (refs 8–10), 94% of the double-transgenic animals (n = 37) exhibited robust tail oscillations upon stimulation of the caudal spinal cord with a short light pulse (see Methods) (Fig. 1b and Supplementary Movie 2). The frequency and initial deflection angle of these oscillations closely resembled the spontaneous slow swim that we observed in unrestrained animals (Fig. 1c–f). The optical stimulation had no effect on non-transgenic larvae (n = 12) or on LiGluR-expressing larvae not incubated with MAG1 (n = 12).

The swim-like response induced by light in *Gal4*^{s1020t}/*UAS:LiGluR* larvae differed from the well-described touch–escape response[13], in which larvae respond to touch on one side of the tail by an initial sharp bend of the tail ('C-bend') to the opposite side that propels the fish away from the touch (Fig. 1g and Supplementary Movie 3). A C-bend to either the left or right side was elicited by bilateral illumination of the tail in *UAS:LiGluR*/*Gal4*^{s1102t}-line[10] larvae expressing the LiGluR in Rohon-Beard touch sensing neurons of the tail. A C-bend was evoked in 79% of trials (seven larvae tested five times each) (Fig. 1h, i and Supplementary Movie 4), resembling the natural escape of free-swimming fish (see initial one-sided tail bend, the frequency and the number of the ensuing tail beats in Fig. 1i–l). The left/right symmetry of the beating oscillations and small deflection angle seen in the *Gal4*^{s1020t} line distinguish it from this Rohon-Beard-cell-induced asymmetric escape response of the *Gal4*^{s1102t} line (compare Fig. 1c, d with Fig. 1i, j).

Gal4^{s1020t} drives expression in several cell types in the ventral spinal cord (Fig. 2a). Inverse PCR cloning indicates that the transposon is integrated near the *Olig2* gene[11]. Indeed, the expression pattern of *Gal4*^{s1020t} is indistinguishable from that seen in an *Olig2:GFP* transgenic line[14] (Supplementary Fig. 2). Using the *BGUG* expression system to determine which cell types express GAL4 in the *Gal4*^{s1020t} line (Supplementary Methods), we found that 79% of the 250 cells imaged in 73 fish were motor neurons (26.4% primary motor neurons: Fig. 2b, top panel; 52.4% secondary motor neurons: Fig. 2b, bottom panel). The remaining cells (20.4%) were neurons with a central ascending axon and lacking dendrites (Fig. 2c, d, f). A few cells (two out of 250 cells (0.8%)) resembling oligodendrocytes were also green fluorescent protein (GFP)-positive (data not shown). The neurons with a central axon appeared to represent a single cell type. They are located near the central canal and have an ascending axon that projects ipsilaterally, making terminals in a series of two to six consecutive segments (Fig. 2c, d, f). Instead of dendrites these cells have a brush of cilia emanating from the somata, which appear to contact the cerebrospinal fluid (CSF), as shown by the alignment of the cilia with the central canal (Fig. 2e). Antibody staining showed that these neurons are GABA (γ-aminobutyric acid)- and GAD65/67-positive (Fig. 2g, h and Supplementary Fig. 3) as well as somatostatin-positive (Supplementary Fig. 4). Combined, these features are consistent with these neurons being Kolmer–Agduhr cells[5, 15].

To find out whether the Kolmer–Agduhr neurons are responsible for triggering the swim-like behaviour in the *Gal4*^{s1020t}/*UAS:LiGluR* fish, we screened more *Gal4* lines and found one line, *Gal4*^{s1003t}, in which expression in the spinal cord is restricted to Kolmer–Agduhr cells. These cells shared morphology, cell body position and marker expression with the sensory neuron labelled in *Gal4*^{s1020t} (Fig. 3a–d and Supplementary Fig. 5). As in *Gal4*^{s1020t}/*UAS:LiGluR*, the light-induced response in *Gal4*^{s1003t}/*UAS:LiGluR* consisted of an alternating symmetrical tail beat at the slow swim frequency (Fig. 3e–i and Supplementary Movie 5), confirming that Kolmer–Agduhr cells are indeed able to trigger the CPG. The properties of the light-induced swim in the *Gal4*^{s1003t}/*UAS:LiGluR* larvae were indistinguishable from those of *Gal4*^{s1020t}/*UAS:LiGluR* (Fig. 3), which suggests that at the intensities applied, motor neurons are not activated in *Gal4*^{s1020t}/*UAS:LiGluR.*

Indeed, calcium imaging in tetrodotoxin (to block action potentials and confine activity to the optically stimulated cells) revealed that the light pulses used in the behavioural experiments were strong enough to activate the narrow region surrounding the central canal where Kolmer–Agduhr cells are located, but not elsewhere in the ventral spinal cord where most motor neurons are situated (Supplementary Fig. 6).

To eliminate the possibility that motor neuron activation in *Gal4*^{s1020t}/*UAS:LiGluR* fish elicits swimming movements, we tested two additional *Gal4* lines with motor neuron expression but no expression in Kolmer–Agduhr cells: *Gal4*^{s1041t} and *Hb9*:*Gal4* (ref. 16) (Supplementary Fig. 7). Light pulses that reliably triggered swim-like behaviour in animals expressing LiGluR in the *Gal4*^{s1020t} and *Gal4*^{s1003t} lines produced no effect in either of these motor neuron lines (six LiGluR larvae tested for each line; Fig. 3j). However, increasing the intensity or duration of illumination by at least tenfold evoked contraction on the illuminated side of the tail, which was distinct from the forward swim-like behaviour (Supplementary Fig. 8). The requirement for stronger illumination to evoke the contraction is consistent with the larger size and lower input resistance of motor neurons[17]. Altogether, these observations show that the forward swim can be attributed specifically to the activation of the Kolmer–Agduhr cells.

Kolmer–Agduhr cells are GABAergic. To test the role of GABAergic transmission in the light-induced response of *Gal4*^{s1020t}/*UAS:LiGluR*, we injected the GABA-A antagonist bicuculline into the spinal cord. This treatment greatly reduced the number of oscillations evoked by light in *Gal4*^{s1020t}/*UAS:LiGluR* fish ($P < 10^{-6}$, $t(7) = 11.2950$; Supplementary Fig. 9), abolishing the light-induced response entirely in four out of eight larvae. These experiments indicate that the optical stimulation of Kolmer–Agduhr cells is sufficient to initiate a swim-like behaviour by a GABA-dependent process.

Having shown that activation of Kolmer–Agduhr cells is sufficient for inducing a swim-like behaviour, we next asked whether they are also necessary for spontaneous swimming by blocking synaptic transmission from Kolmer–Agduhr cells by a targeted expression of the tetanus toxin light chain (TeTxLC) fused to cyan fluorescent protein (CFP) (*UAS:TeTxLC-CFP* (ref. 18) crossed with *Gal4*^{s1020t} and *Gal4*^{s1003t}). Three- to five-day-old larvae expressing TeTxLC-CFP were easily identified by their CFP fluorescence (Methods). We compared the swimming behaviour of CFP-positive larvae with that of siblings that did not have CFP fluorescence (that is, did not express TeTxLC). *Gal4*^{s1020t}/*UAS:TeTxLC-CFP* larvae expressing the TeTxLC were paralysed at five days, as expected for expression of GAL4 in motor neurons. On the other hand, *Gal4*^{s1003t}/*UAS:TeTxLC-CFP* larvae, which lack motor neuron expression, were not paralysed, enabling behavioural assays. *Gal4*^{s1003t}/*UAS:TeTxLC-CFP* exhibited spontaneous burst-swimming, but the frequency of the swims was greatly reduced ($P < 0.0075$; $t(9) = -3.4278$) (Fig. 3k). These results indicate that Kolmer–Agduhr cells provide a positive drive to spontaneous swimming. It should be noted that only half of the Kolmer–Agduhr cells express the UAS transgene in the *Gal4*^{s1003t} line (Supplementary Fig. 3), which suggests that block of synaptic transmission in all of the Kolmer–Agduhr cells could have an even more profound effect on spontaneous swimming. Strikingly, we found that *Gal4*^{s1003t}/*UAS:TeTxLC-CFP* still respond to touch

by a touch–escape (P = 0.45; t(11) = 0.7863) (Fig. 3k), indicating that Kolmer–Agduhr cells do not play a significant role in initiating touch–escape.

We further examined the Kolmer–Agduhr-induced swim and the Rohon-Beard-induced escape behaviours by performing local photo-activation. Because mechanical activation on one side of the larva elicits, as part of the escape response, a C-turn on the opposite side (Fig. 1g), we predicted that one-sided optical activation of Rohon-Beard cells would have the same effect. We tested this by confining the illumination to a small portion of the spinal cord with a digital light processing array (Fig. 4a). One-sided optical stimulation of Rohon-Beard cells in the *Gal4*^{s1102t} line triggered a reliable large-angle contralateral bend (n = 9 out of 9; Fig. 4c), resembling the C-bend induced by one-sided mechanical stimulation (Fig. 1i). In contrast, one-sided optical stimulation of *Gal4*^{s1020t} elicited a symmetrical forward swim-like behaviour (Fig. 4b), closely resembling the response to bilateral optical stimulation (Fig. 1c).

To test the involvement of supraspinal inputs in the Kolmer–Agduhr-elicited swim-like behaviour, we performed hindbrain lesions that ablated the connections between the brain and the spinal cord (Fig. 4d). Tactile stimuli sensed by Rohon-Beard cells are known to be transmitted to the hindbrain[13] where the command for escape is relayed back to the tail, and ablation of the hindbrain was shown earlier to suppress the fast contralateral C-bend that begins the escape[13]. Consistent with this, the C-bend component of the response to optical activation of Rohon-Beard cells in the *Gal4*^{s1102t}/*UAS:LiGluR* line was abolished by the hindbrain lesion (n = 4 out of 4; Fig. 4f). In contrast, the light-evoked swim-like behaviour in *Gal4*^{s1020t} remained intact after the lesion (n = 7; Fig. 4e), which demonstrates that intra-spinal activation of *Gal4*^{s1020t}-positive neurons is sufficient to drive the swim-like behaviour.

Previous work in vertebrates has implicated specific classes of spinal interneuron in regulating locomotion speed[19, 20] or movement strength, and their activity was associated with specific states of the spinal networks recorded during fictive locomotion[16, 21]. These studies were based on either loss of function[19] or on correlation of the activity of neurons with specific phases of ventral root activity during fictive locomotion[16, 20]. We show that it is possible to employ a light-gated channel to show sufficiency of genetically targeted neurons in behaviour. Genetically encoded blockers of activity can then be used to also show the necessity of neuronal function in behaviour (Supplementary Fig. 1).

Previous studies in the lamprey showed that the GABAergic system is a strong modulator of fictive swimming[22], but there are many types of spinal GABAergic neuron and the neuronal basis for the observed modulation was not known. We demonstrate here that a single GABAergic cell, the Kolmer–Agduhr neuron, is a major modulator of locomotion in the awake behaving animal. Although Kolmer–Agduhr neurons were first described decades ago[5], their role in spinal circuits remained enigmatic. We show that Kolmer–Agduhr cells are necessary for the normal frequency of spontaneous swimming and are sufficient to drive the CPG in early development, when GABAergic transmission is excitatory[23].

The Kolmer–Agduhr neurons of zebrafish resemble the CSF-contacting cells of lamprey and other vertebrates, including mammals[24, 25], in that they express GABA and the transcription factor olig2 (ref. 26) (Supplementary Fig. 2), are located next to the central canal and project a brush of stereocilia into the CSF, and have axons that run longitudinally[25]. It remains to be determined whether potential homologues of Kolmer–Agduhr cells may affect locomotor patterns in mammals.

Although we have determined that Kolmer–Agduhr cells provide a positive drive to the CPG in larval fish, in adult fish and in postnatal mammals, GABAergic transmission is inhibitory and blocking GABA receptor in the adult lamprey enhances swim frequency[22]. This suggests that Kolmer–Agduhr activity may suppress swimming in adult zebrafish. The 'liquor-contacting' cilia of the Kolmer–Agduhr neurons in the central canal[5, 15, 22] could allow them to sense mechanical deformation of the spine or chemical signals in the central canal, such as low pH, as proposed recently for mammalian CSF-contacting neurons[27]. The natural drive to Kolmer–Agduhr cells and their function later in life remain to be defined.

METHODS

Summary

To determine which cell types express in a GAL4 line and to quantify their abundance, we used the *BGUG* transgene (short for Brn3c:Gal4; *UAS: mGFP*), which labels a small, random subset of the GAL4-expressing cells owing to variegated expression of the gene encoding a membrane-targeted GFP[11, 28]. The transgenic line *UAS:LiGluR*, as well as all Gal4 lines from the enhancer trap screen, were published previously[10, 11]. To make the *Hb9:Gal4* transgenic construct, 3 kilobases of genomic sequence upstream of the *hb9* coding sequence[18, 29] was amplified by PCR and inserted upstream of the *GAL4* coding sequence[30]. Synthesis of MAG-1 was performed as described[8, 9, 10]. Five-day-old larvae were bathed in 200 µM MAG-1, 4% dimethylsulphoxide (DMSO) for 45 min at 28.5 °C in the dark. The fast photoswitching light source was coupled to an upright Zeiss epifluorescence microscope. Patterned illumination was accomplished using a digital micromirror device. Motion of the tail was monitored at 250 frames per second by using a high-speed camera. Lesions were performed on anaesthetized larvae bathed in Evans solution with a fine tungsten needle. Embryos at appropriate stages were fixed in 4% PFA in PBS and processed for immunohistochemistry according to published protocols[28]. Injection of the calcium dye was performed 30–60 min after MAG-1 labelling. Fluorometric Ca^{2+} measurements were performed using a confocal Olympus laser-scanning microscope equipped with an ultraviolet SIM Scanner. Tracking of the tail position and calcium imaging analysis were performed using a custom-made script written in Matlab 2007 (Mathworks).

Generation of transgenic lines

Zebrafish were maintained at 28 °C in the Tubingen Line genetic background. To make the *Hb9:Gal4* transgenic construct, 3 kilobases of genomic sequence upstream of the *hb9* coding sequence[18, 29] was amplified by PCR and inserted upstream of the *GAL4* coding sequence[30]. This expression cassette was inserted between the Tol2 recognition sequences in the pT2KXIGΔin vector[31]. Wild-type TL embryos were injected at the one-cell stage with a solution of 25 ng μl^{-1} *Hb9:GAL4* DNA, 50 ng μl^{-1} transposase mRNA (prepared using the Ambion mMESSAGE mMACHINE T7 kit) and 0.04% Phenol Red. F1 embryos were pooled and screened for the transgene by crossing them with *UAS:Kaede* carriers. F0 founder animals were then mated to wild-type TL fish to create stable lines.

The following transgenic lines were used (designations according to official zebrafish nomenclature; previously published synonyms or abbreviated name are in parentheses): Tg(*UAS:iGluR6*(L439C))s1995 (*UAS:LiGluR*); *Tg(UAS-E1b:Kaede)s1999t/+ (UAS:Kaede); Et(-1.5hsp70l:Gal4-VP16)s1003t (Gal4^{s1003t}); Et(-0.6hsp70l:Gal4-VP16)s1020t (Gal4^{s1020t}); Et(fos:Gal4-VP16)s1041t (Gal4^{s1041t}); Et(E1b:GAL4-VP16)s1102t (Gal4^{s1102t}); Tg(pou4f3:GAL4,UAS:gap43-GFP)s314t (BGUG); Tg(5xUAS:TeTxLC-CFP)zf85 (UAS:TeTxLC-CFP).* Because the GAL4 lines carry the *UAS:Kaede* construct, embryos positive for Kaede produced in a cross with

UAS:LiGluR carriers were selected for behaviour experiments (50% were also *UAS:LiGluR* expressers). Dark embryos were used for calcium-imaging experiments. Genotyping of larvae for the LiGluR transgene was performed after behavioural experiments using the following primers: forward primer GGCTTGAGGATGGGAAATATGG and reverse primer GGGTTGCAAGGGTGTGGGTTATACC.

To determine which cell types expressed GAL4 in the Gal4s1020t line and to quantify their abundance, we used the *BGUG* transgene (an abbreviation of Brn3c:Gal4; *UAS:mGFP*), which labels a small, random subset of the GAL4-expressing cells owing to variegated expression of the gene encoding a membrane-targeted GFP[11, 28].

MAG-1 labelling and mounting of zebrafish larvae

Synthesis of MAG-1 was performed as previously described[8, 9, 10]. MAG-1 was first diluted to 5 mM in DMSO and pre-activated by ultraviolet light (365 nm) for 1 min. The medium E3 was then added to reach the final concentration of 200 µM MAG-1, 4% DMSO. Five days after fertilization, larvae were bathed in the labelling solution for 45 min at 28.5 °C in the dark. The larvae were then washed three times with fresh E3 medium. After recovery period of 1 h, all spontaneously swimming larvae were embedded in 2% agar and free-tailed. The agar was removed up to the fins for the behaviour experiments where illumination of the tail was global under a ×5 air objective (numerical aperture = 0.25), whereas the agar was removed only up to the anus for experiments where single (group of) cells were illuminated under the ×40 water immersion objective (numerical aperture = 0.8).

Photostimulation

The light source used for fast photoswitching was a DG-4 (Sutter Instruments) coupled to an upright Zeiss AxioImager epifluorescence microscope. Patterned illumination was accomplished using a digital micromirror device (Mosaic System, Photonic Instruments) coupled to the epifluorescence path of the microscope. For global illumination experiments, we illuminated the caudal portion of the tail bilaterally using a ×5 air objective (the light power was 0.24 mW mm^{-2} at 390 nm and 0.71 mW mm^{-2} at 500 nm; as a comparison the low power illumination previously used[10] was 0.04 mW mm^{-2} at 365 nm for 15 min), whereas local illumination of single segments or groups of cells was achieved using a ×40 water immersion objective (light power 24.6 mW mm^{-2} at 390nm and 37.7 mW mm^{-2} at 500 nm).

The *Gal4* transgenic lines carry the *UAS:Kaede* constructs. Therefore, in all behavioural experiments reported here with *Gal4* lines, we selected the larvae expressing Kaede. Half of the larvae tested were positive for *UAS:LiGluR*, meaning that the tests were always run blindly and genotyping was performed afterwards. The light-induced responses of $Gal4^{s1020t}$/*UAS:LiGluR*, $Gal4^{s1102t}$/*UAS:LiGluR* and $Gal4^{s1003t}$/*UAS:LiGluR* labelled with MAG-1 were abolished by bath application of tricaine (0.02%; n = 8, 8 and 7, respectively).

We used patterned illumination to ask whether optical stimulation of CSF-contacting neurons in three consecutive segments on either the left or the right side of the animal would also evoke asymmetrical tail motions (experiments were done in the *Gal4*^{s1020t} line because it reliably targets all Kolmer–Agduhr neurons, whereas *Gal4s*^{1003t} drives expression in only half of them).

Monitoring of behavioural responses

Five-day-old larvae exhibit spontaneous forward swims, also referred to as slow swims[12]. These occur in brief bursts, with each burst consisting of a series of symmetrical, dampening left–right oscillations, which can be analysed quantitatively in 'head-centred' movies, where the image of the fish in each frame is repositioned to register the head in one spot so that the movements of the tail can be visualized (Fig. 1a and Supplementary Movie 1). Swimming movements can also be observed in semi-restrained larvae with their heads fixed in agar and tails free to move (Methods), thus allowing targeted optical stimulation of the central nervous system to be combined with behavioural analysis and providing an easy comparison with the head-centred free swim. We chose several *Gal4* transgenic lines that allowed us to drive expression of LiGluR in different subsets of spinal neurons, and we asked whether optical activation of these neurons elicits a forward swim-like behaviour.

Motion of the tail was monitored at 250 frames per second using a high-speed camera (Fastec Inline, Itronx Imaging Technologies). The camera was coupled to the side port of the AxioImager microscope in global illumination experiments using the ×5 objective, or coupled to a ×4 objective under the stage when local photoswitching was performed using a higher magnification (×40) objective. The tracking of the tail position was performed using a custom-made script written in Matlab 2007 (Mathworks). Lesions were performed on larvae anaesthetized by a cold exposure and bathing in Evans solution using a fine tungsten needle at the boundary of the hindbrain and spinal cord. Animals were tested after a period of 60 min recovery. The quantification of spontaneous swimming in *Gal4*^{s1003t}*/UAS:TeTxLC-CFP* and dark siblings was performed by isolating six 5-day-old larvae at a time and counting swimming events in a 10-min recording. Thirty larvae were observed for each group. All experiments were conducted at room temperature.

Immunochemistry

Embryos at appropriate stages were fixed in 4% PFA in PBS and processed for immunohistochemistry according to published protocols[28]. The following primary antibodies and concentrations were used for whole-mount immunohistochemistry: antibody to GFP (rabbit anti-GFP; Molecular Probes A11122, or chick anti-GFP; GeneTex GTX13970) 1:500; antibody to GABA (rabbit anti-GABA; Sigma A2052) 1:2,000; antibody to GAD65/67 (rabbit anti GAD65+GAD67; Abcam ab11070-50) 1:500; antibody to Somatostatin (ImmunoStar 20067) 1:200. GABA immunostaining required fixation in 0.1% glutaraldehyde/4%PFA in PBS. Secondary antibodies conjugated to

Alexa-488 or Alexa-555 (Invitrogen) were selected accordingly and used at 1:500 dilutions. Nuclei were counterstained with DAPI (Invitrogen).

Dye preparation and loading

Injection of the calcium dye was performed 30–60 min after MAG-1 labelling. Oregon Green Bapta 1-AM was freshly diluted in DMSO with 20% pluronic acid (Invitrogen) to yield to a 10 mM stock solution and further diluted in Evans solution with 0.01% Fast-Green (Sigma-Aldrich) to a final concentration of 1 mM. A fine borosilicate pipette of 1 mm outer diameter and 0.5 mm internal diameter (FHC; 5 MΩ resistance when filled with Evans solution) was used to inject the dye in the spinal cord using a Picospritzer (General Valve; 50 ms, 20 pounds per square inch, one to three puffs). Calcium recordings were performed between 1 and 5 h after the dye loading.

Calcium imaging

Fluorometric Ca^{2+} measurements were performed at room temperature using a confocal Olympus Fluoview laser scanning microscope equipped with a ×40 (numerical aperture = 0.8) water immersion objective. The 488-nm argon laser (20 mW) was used at 1–3% power for exciting the dye, and a 405-nm laser (50 mW) used at 1–30% power for photoswitching. Frames were acquired at 4–10 Hz. Local photoactivation of cells was performed by one scan at the same acquisition speed repeated every 10 s unless otherwise stated. Values of $\Delta F/F_s$ were computed using a custom-made script in Matlab 2007.

Pharmacology

Tricaine (0.02%) was dissolved in E3 and added to the bath. Bicuculline dissolved in fish Ringer's solution was injected at 40 µM, and TTX at 10 µM.

Figure 1

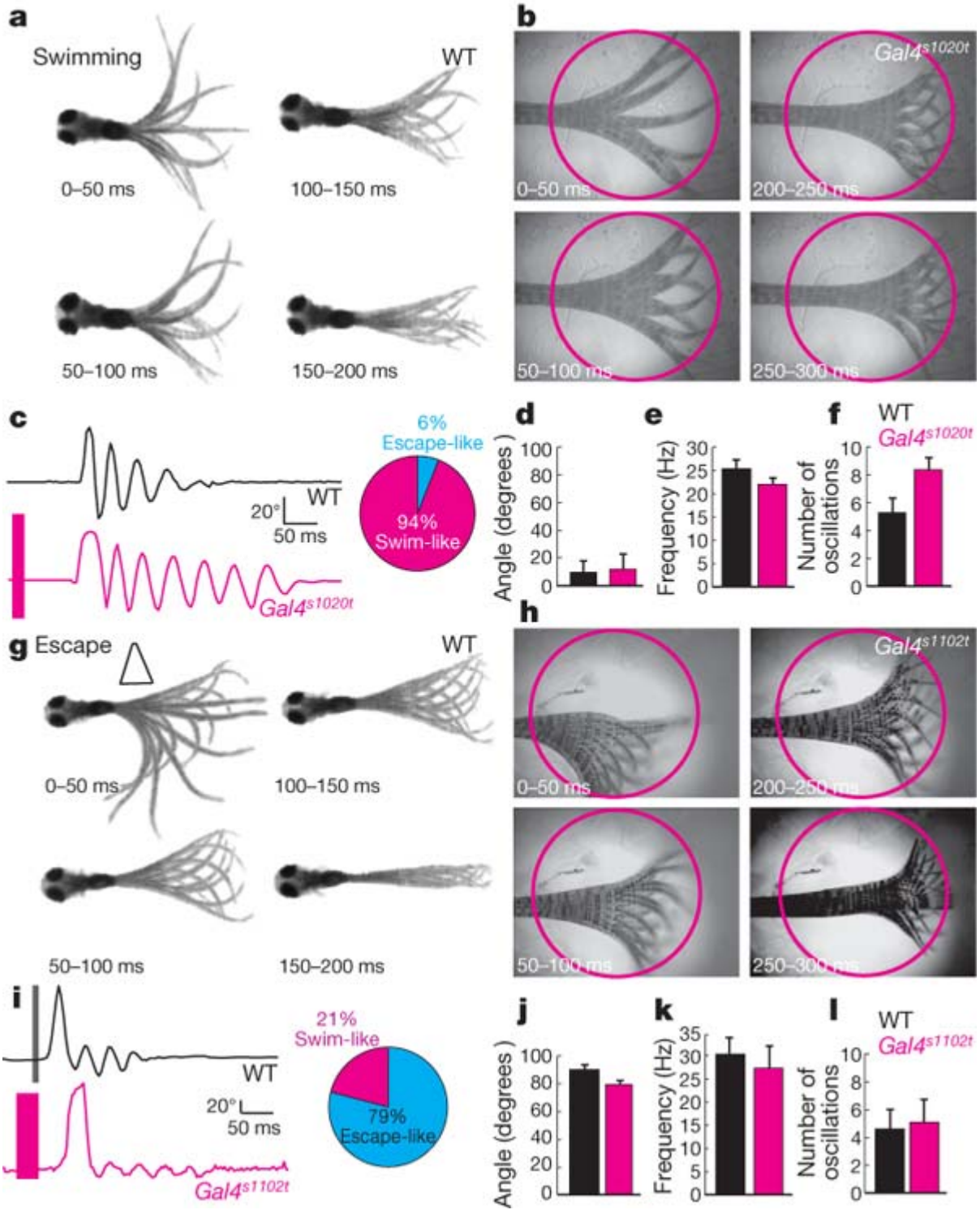
a
Swimming
WT
0–50 ms
100–150 ms
50–100 ms
150–200 ms
b
Gal4s1020t
0–50 ms
200–250 ms
50–100 ms
250–300 ms
c
6%
Escape-like
WT
20°
50 ms
94%
Swim-like
Gal4s1020t
d
Angle (degrees)
e
Frequency (Hz)
f
WT
Gal4s1020t
Number of oscillations
g Escape
WT
0–50 ms
100–150 ms
50–100 ms
150–200 ms
h
Gal4s1102t
0–50 ms
200–250 ms
50–100 ms
250–300 ms
i
21%
Swim-like
WT
20°
50 ms
79%
Escape-like
Gal4s1102t
j
Angle (degrees)
k
Frequency (Hz)
l
WT
Gal4s1102t
Number of oscillations

Figure 1: Optical stimulation of specific spinal neurons leads to distinct locomotor behaviours. **a**, Spontaneous swim (superimposed frames). **b**, Optical stimulation (circle) of *Gal4*^{s1020t}/*UAS:LiGluR* evokes a 'spontaneous swim'-like behaviour. **c**, Comparison of deflection angle traces corresponding to **a** (top, black) and **b** (bottom, magenta, bar for stimulation) (inset: 94% of responses were a swim (n = 18)). No difference in angle (P = 0.51) (**d**) or frequency (P = 0.09) (**f**), but more oscillations (P < 0.01) (**e**) in light-induced swims. Values are given + s.e.m. (n = 9). **g**, Escape elicited by a water jet (triangle) consists of sharp C-turn away from stimulus followed by a forward swim. **h**, Light-induced escape induced by stimulation of Rohon-Beard cells in *Gal4*^{s1102t}/*UAS:LiGluR* larvae. **i**, Tail deflection traces corresponding to **g** (top) and **h** (bottom) (inset: 79% of responses were an escape (n = 11)). **j–l**, No difference in (**j**) deflection angle (P = 0.13), (**k**) frequency (P = 0.42) and (**l**) number of oscillations (P = 0.41). Values are given + s.e.m. (n = 7).

Figure 2

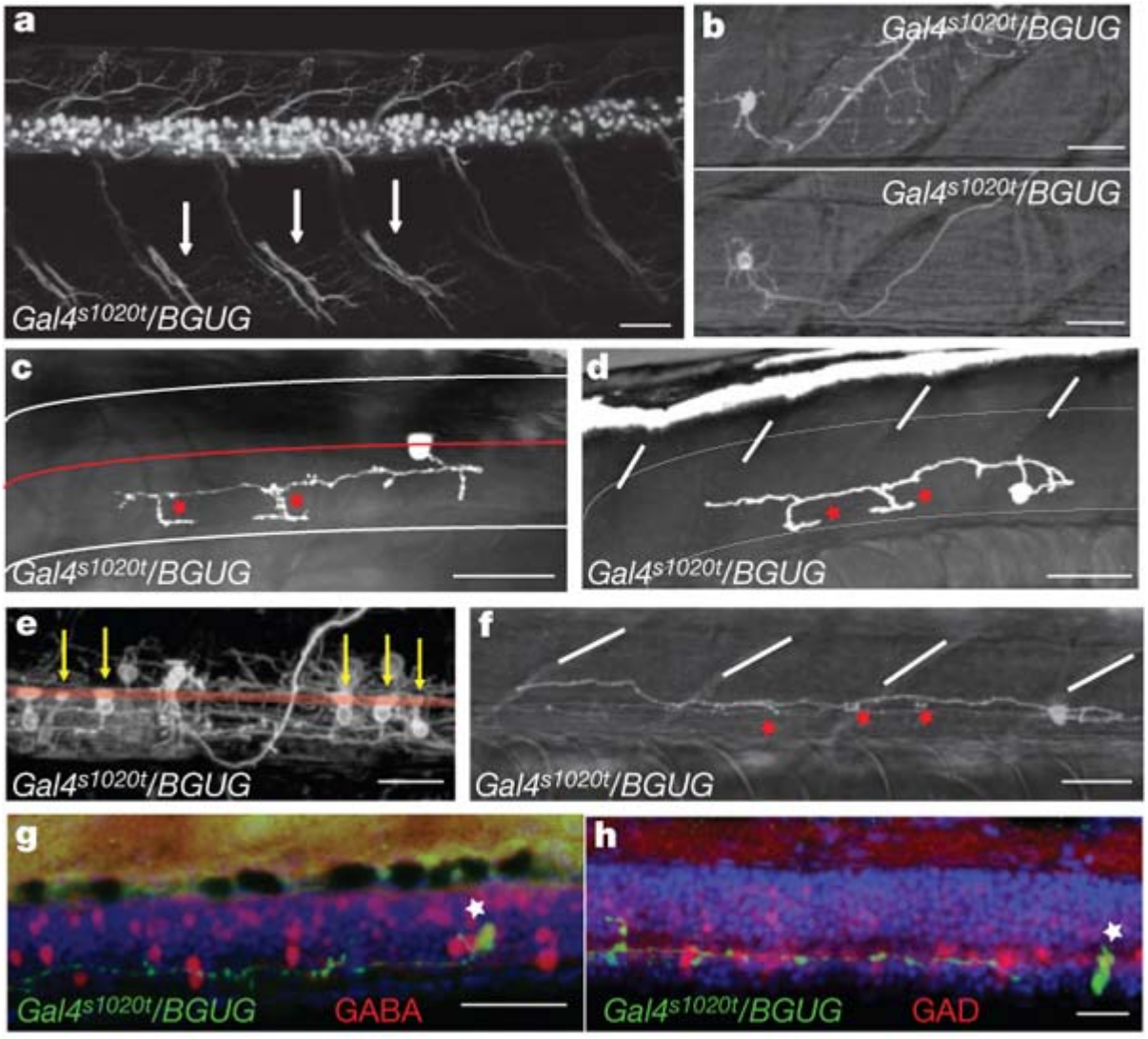
a
Gal4s1020t/BGUG
b
Gal4s1020t/BGUG
Gal4s1020t/BGUG
c
Gal4s1020t/BGUG
d
Gal4s1020t/BGUG
e
Gal4s1020t/BGUG
f
Gal4s1020t/BGUG
g
Gal4s1020t/BGUG
GABA
h
Gal4s1020t/BGUG
GAD

Figure 2: The *Gal4*^{s1020t} line drives expression in motor neurons and Kolmer–Agduhr neurons. a, Expression in ventral cells including motor neurons projecting out of cord (arrows) (lateral view). **b**–**e**, Random labelling in *Gal4*^{s1020t}/*BGUG* identifies solely two cell types: **b**, motor neurons (primary motor neurons, top; secondary motor neurons, bottom) and **c**–**f**, Kolmer–Agduhr neurons (dorsal (**c**) and lateral (**d**–**f**) views of neuron with a central ipsilateral ascending axon; segment boundaries: white lines). Note contact feet (red stars in **c** and **d**) and 'toothbrush' morphology of cilia (yellow arrows in **e**) characteristic of Kolmer–Agduhr cells. In **c**, larva is tilted to show enlarged contacts on axon (midline, red line and segment, white lines). **e**, Dense *BGUG* pattern with multiple Kolmer–Agduhr cells shows the alignment of the brush of cilia (arrows) with central canal. **f**, The ascending axon runs near the ventral edge of the spinal cord before aiming dorsally. **g**, **h**, Kolmer–Agduhr cells at 5 days post-fertilization in *Gal4*^{s1020t}/*BGUG* (green) are GABAergic neurons (anti-GAD (**g**) and anti-GABA (**h**) immunostaining in red). Scale bars, 25 μm.

Figure 3

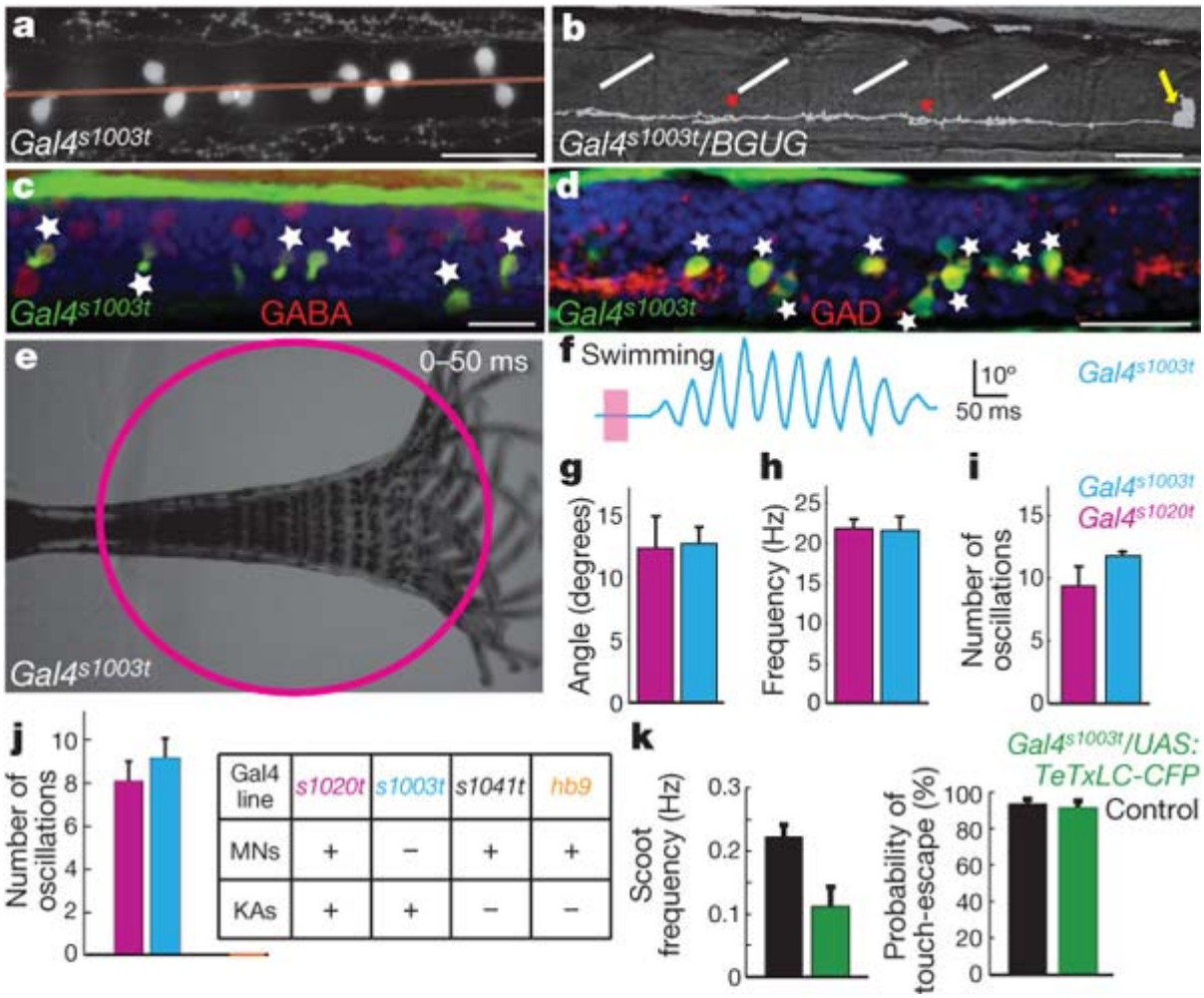
a
Gal4s1003t
b
Gal4s1003t/BGUG
c
Gal4s1003t
GABA
d
Gal4s1003t
GAD
e
0–50 ms
Gal4s1003t
f Swimming
10°
50 ms
Gal4s1003t
g
Angle (degrees)
h
Frequency (Hz)
i
Gal4s1003t
Gal4s1020t
Number of oscillations
j
Number of oscillations
Gal4 line | s1020t | s1003t | s1041t | hb9
MNs | + | – | + | +
KAs | + | + | – | –
k
Scoot frequency (Hz)
Gal4s1003t/UAS: TeTxLC-CFP
Control
Probability of touch-escape (%)

Figure 3: Optical stimulation of Kolmer–Agduhr cells of *Gal4*^{s1003t} line induces a forward swim. a, Expression in spinal cord is confined to cells close to the midline (dorsal view). **b**, Lateral view in *BGUG* shows ventral neurons with central axons forming contact feet (red stars) and toothbrush morphology (arrow). White lines are segment boundaries. **c**, **d**, These cells (green) are GABAergic (anti-GAD and anti-GABA staining in red). **e**, **f**, Optical stimulation induces a swim-like response. **e**, Superimposed images. **f**, Deflection angle trace. **g**–**i**, No difference in deflection angle (**g**), frequency (**h**) and number of oscillations (**i**) between *Gal4*^{s1003t} (blue) and *Gal4*^{s1020t} (magenta) (respectively $P = 0.85$, $P = 0.98$, $P = 0.36$); values are given + s.e.m. ($n = 9$). **j**, Side-to-side comparison of number of oscillations evoked by a 100-ms pulse of light shows that only lines expressing in Kolmer–Agduhr cells show a swim-like response whereas line with motor neurons (MNs) and no Kolmer–Agduhr cells (KAs) (*Gal4*^{s1041t}, black ; *Hb9:Gal4*, orange) do not ($n = 6$ for each line). **k**, Reduction of the spontaneous swimming frequency in *Gal4*^{s1003t}/*UAS:TeTxLC-CFP* ($P < 0.0075$) but no change in the probability of touch-response ($P = 0.45$). Values are given + s.e.m. ($n = 10$ and 12, respectively).

Figure 4

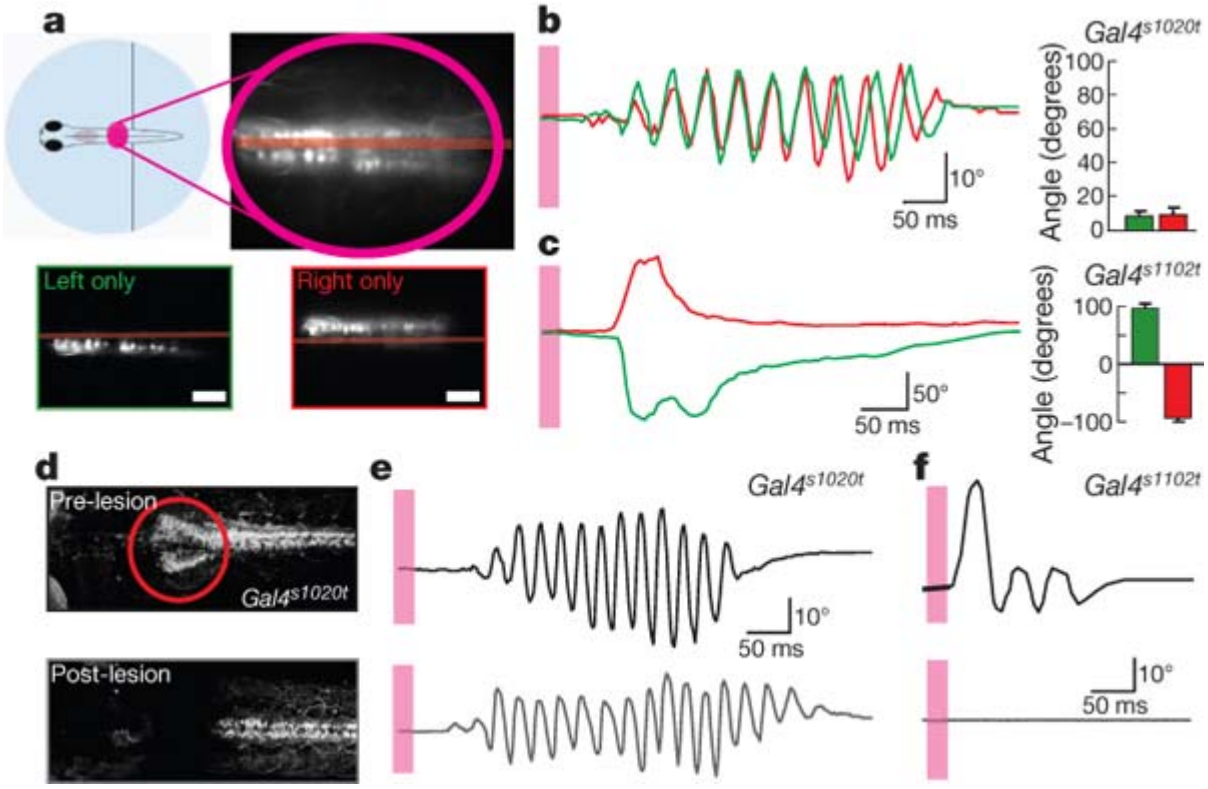

Figure 4: Dissection of the light-evoked responses in *Gal4*^{s1020t} and *Gal4*^{s1102t} by unilateral stimulation and lesion studies. a–c, Patterned illumination for stimulation. **a**, Semi-restrained *Gal4*^{s1020t} larva aimed bilaterally (cartoon and fluorescence image of Kaede expression in three segments, top) and on left or right side (bottom panels; scale bar, 25 μm). **b**, **c**, Deflection angle traces and mean values induced by left (green) and right (red) stimulation. Values are given + s.e.m. **b**, Left and right activations induce similar symmetric oscillations of the tail in *Gal4*^{s1020t} line (*n* = 5). **c**, Left and right activations induce large and opposite-directed C-bends in *Gal4*^{s1102t} (*n* = 9). **d–f**, Effect induced by section of the cerebrospinal connections. **d**, Pattern in *Gal4*^{s1020t} pre- (top) and post- (below) lesion. **e**, **f**, No reduction of the light-induced swim behaviour in *Gal4*^{s1020t} (**e**, *n* = 7) but abolition of the light-induced escape behaviour in *Gal4*^{s1102t} (**f**, *n* = 4) (pre- and post-lesion, top and bottom).

REFERENCES

1. Grillner, S. Biological pattern generation: the cellular and computational logic of networks in motion. Neuron 52, 751–766 (2006)

2. Fenaux, F. *et al.* Effects of an NMDA-receptor antagonist, MK-801, on central locomotor programming in the rabbit. Exp. Brain Res. 86, 393–401 (1991)

3. Kiehn, O. *et al.* Excitatory components of the mammalian locomotor CPG. Brain Res. Rev. 57, 56–63 (2008)

4. Luo, L., Callaway, E. M. & Svoboda, K. Genetic dissection of neural circuits. Neuron 57, 634–660 (2008)

5. Agduhr, E. in Cytology and Cellular Pathology of the Nervous System (ed. Penfield, W.) Vol. 2 535–573 (Hoeber, 1932)

6. Higashijima, S., Mandel, G. & Fetcho, J. R. Distribution of prospective glutamatergic, glycinergic, and GABAergic neurons in embryonic and larval zebrafish. J. Comp. Neurol. 480, 1–19 (2004)

7. Douglas, J. R. *et al.* The effects of intrathecal administration of excitatory amino acid agonists and antagonists on the initiation of locomotion in the adult cat. J. Neurosci. 13, 990–1000 (1993)

8. Volgraf, M. *et al.* Allosteric control of an ionotropic glutamate receptor with an optical switch. Nature Chem. Biol. 2, 47–52 (2006)

9. Gorostiza, P. *et al.* Mechanisms of photoswitch conjugation and light activation of an ionotropic glutamate receptor. Proc. Natl Acad. Sci. USA 104, 10865–10870 (2007)

10. Szobota, S. *et al.* Remote control of neuronal activity with a light-gated glutamate receptor. Neuron 54, 535–545 (2007)

11. Scott, E. K. *et al.* Targeting neural circuitry in zebrafish using GAL4 enhancer trapping. Nat. Methods 4, 323–326 (2007)

12. Budick, S. A. & O'Malley, D. M. Locomotor repertoire of the larval zebrafish: swimming, turning and prey capture. J. Exp. Biol. 203, 2565–2579 (2000)

13. Liu, K. S. & Fetcho, J. R. Laser ablations reveal functional relationships of segmental hindbrain neurons in zebrafish. Neuron 23, 325–335 (1999)

14. Shin, J., Park, H. C., Topczewska, J. M., Mawdsley, D. J. & Appel, B. Neural cell fate analysis in zebrafish using olig2 BAC transgenics. Methods Cell Sci. 25, 7–14 (2003)

15. Dale, N. *et al.* The morphology and distribution of 'Kolmer–Agduhr cells', a class of cerebrospinal-fluid-contacting neurons revealed in the frog embryo spinal cord by GABA immunocytochemistry. Proc. R. Soc. Lond. B 232, 193–203 (1987)

16. Liao, J. C. & Fetcho, J. R. Shared versus specialized glycinergic spinal interneurons in axial motor circuits of larval zebrafish. J. Neurosci. 28, 12982–12992 (2008)

17. Drapeau, P. *et al.* In vivo recording from identifiable neurons of the locomotor network in the developing zebrafish. J. Neurosci. Methods 88, 1–13 (1999)

18. Asakawa, K. *et al.* Genetic dissection of neural circuits by Tol2 transposon-mediated Gal4 gene and enhancer trapping in zebrafish. Proc. Natl Acad. Sci. USA 105, 1255–1260 (2008)

19. Gosgnach, S. *et al.* V1 spinal neurons regulate the speed of vertebrate locomotor outputs. Nature 440, 215–219 (2006)

20. McLean, D. L. *et al.* Continuous shifts in the active set of spinal interneurons during changes in locomotor speed. Nature Neurosci. 11, 1419–1429 (2008)

21. Ritter, D. A., Bhatt, D. H. & Fetcho, J. R. *In vivo* imaging of zebrafish reveals differences in the spinal networks for escape and swimming movements. J. Neurosci. 21, 8956–8965 (2001)

22. Alford, S., Sigvardt, K. A. & Williams, T. L. GABAergic control of rhythmic activity in the presence of strychnine in the lamprey spinal cord. Brain Res. 506, 303–306 (1990)

23. Brustein, E. & Drapeau, P. Serotoninergic modulation of chloride homeostasis during maturation of the locomotor network in zebrafish. J. Neurosci. 25, 10607–10616 (2005)

24. Vigh, B. & Vigh-Teichmann, I. Actual problems of the cerebrospinal fluid-contacting neurons. Microsc. Res. Tech. 41, 57–83 (1998)

25. Stoeckel, M. E. *et al.* Cerebrospinal fluid-contacting neurons in the rat spinal cord, a gamma-aminobutyric acidergic system expressing the P2X2 subunit of purinergic receptors, PSA-NCAM, and GAP-43 immunoreactivities: light and electron microscopic study. J. Comp. Neurol. 457, 159–174 (2003)

26. Furusho, M. *et al.* Involvement of the Olig2 transcription factor in cholinergic neuron development of the basal forebrain. Dev. Biol. 293, 348–357 (2006)

27. Huang, A. L. *et al.* The cells and logic for mammalian sour taste detection. Nature 442, 934–938 (2006)

28. Xiao, T. & Baier, H. Lamina-specific axonal projections in the zebrafish tectum require the type IV collagen Dragnet. Nature Neurosci. 10, 1529–1537 (2007)

29. Flanagan-Steet, H., Fox, M. A., Meyer, D. & Sanes, J. Neuromuscular synapses can form in vivo by incorporation of initially aneural postsynaptic specializations. Development 132, 4471–4481 (2005)

30. Koster, R. W. & Fraser, S. E. Tracing transgene expression in living zebrafish embryos. Dev. Biol. 233, 329–346 (2001)

31. Masahira, N. *et al.* Olig2-positive progenitors in the embryonic spinal cord give rise not only to motoneurons and oligodendrocytes, but also to a subset of astrocytes and ependymal cells. Dev. Biol. 293, 358–369 (2006)

SUPPLEMENTAL INFORMATION

Supplemental Figure 1

Supplemental Figure 1. Optical stimulation of cerebrospinal contacting neurons reveals that these cells can recruit the central pattern generator leading to locomotion in the zebrafish larva.

Supplemental Figure 2

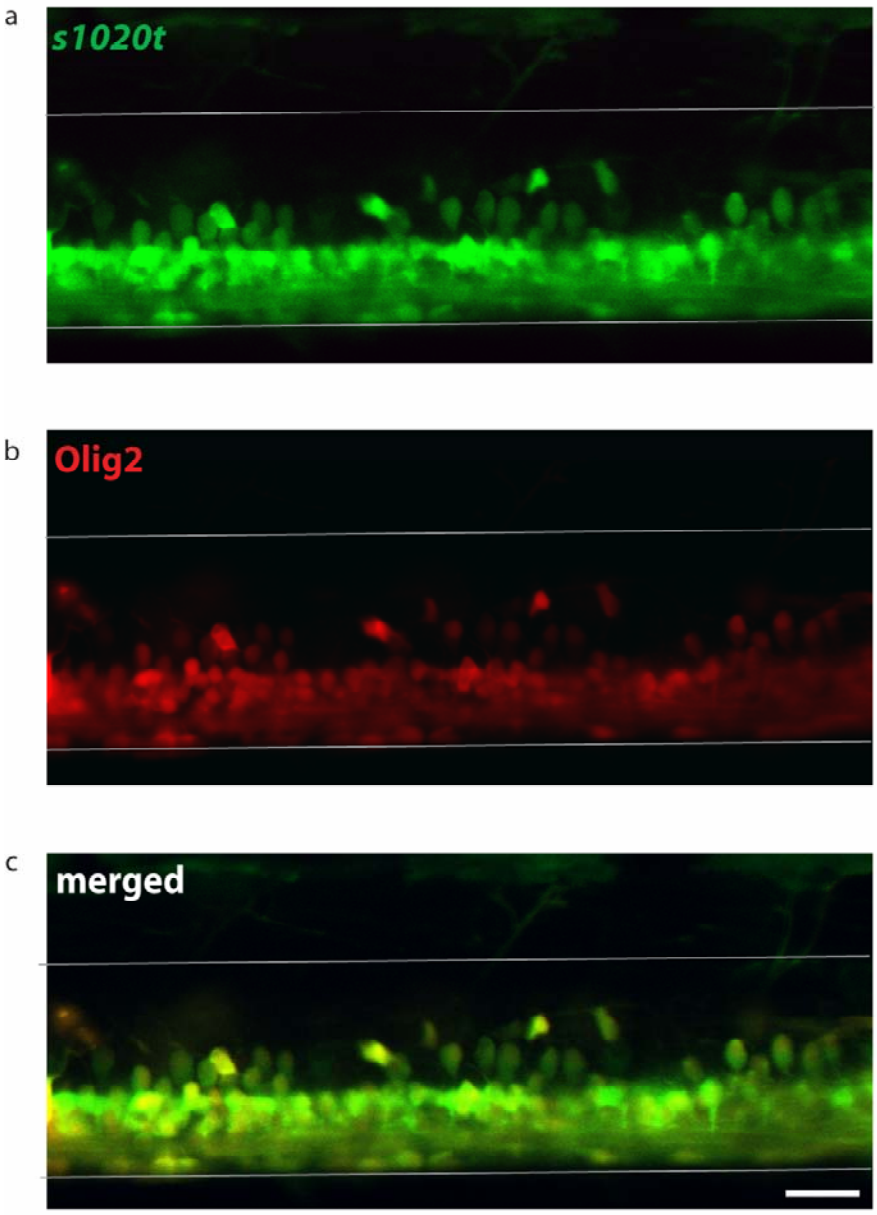

Supplemental Figure 2. The pattern of expression of Olig2 and the *Gal4s1020t* are identical. a, Expression of GFP in the UAS:GFP/*Gal4s1020t*. **b,** Expression of Olig2:DsRed. **c,** Merged image of GFP and Olig2:DsRed. Embryo was 48hours post fertilization. Scale Bar is 25μm.

Supplemental Figure 3

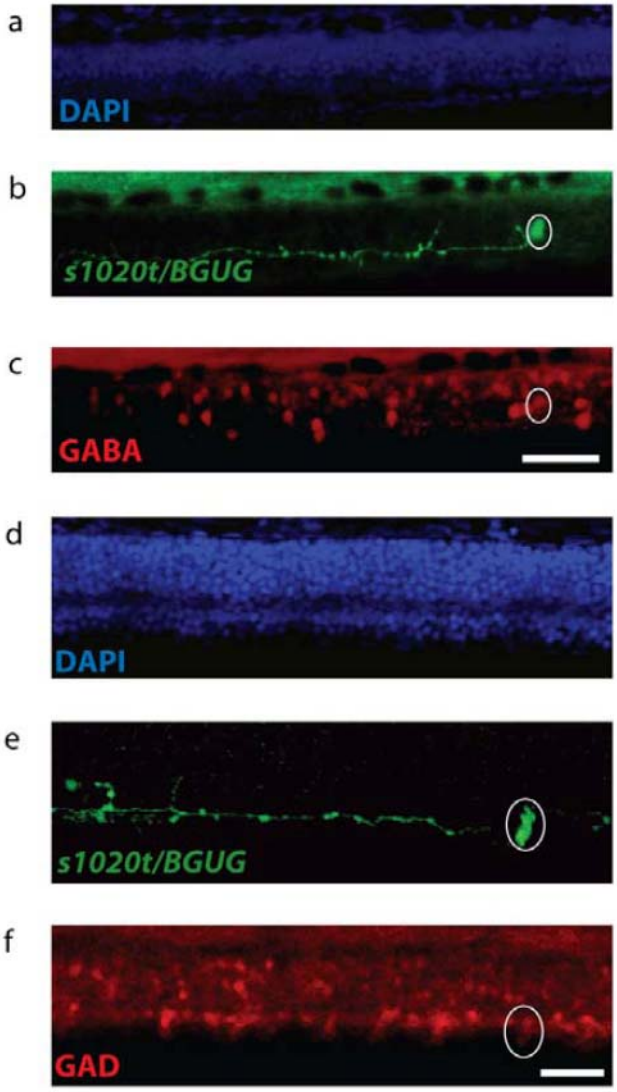

Supplemental Figure 3. KA neurons are GABAergic as shown by immunostaining for GABA and GAD65/67 in *Gal4s1020t/BGuG.* a-c, Immunostaining for GABA. **a,** Dapi image. **b,** Sparse label of a single KA neuron expressing GFP. **c,** GABA immunostaining. **d-f,** Immunostaining for GABA. **d,** Dapi image. **e,** Sparse label of a single KA neuron expressing GFP. **f,** GAD immunostaining. Scale bar is 25μm.

Supplemental Figure 4

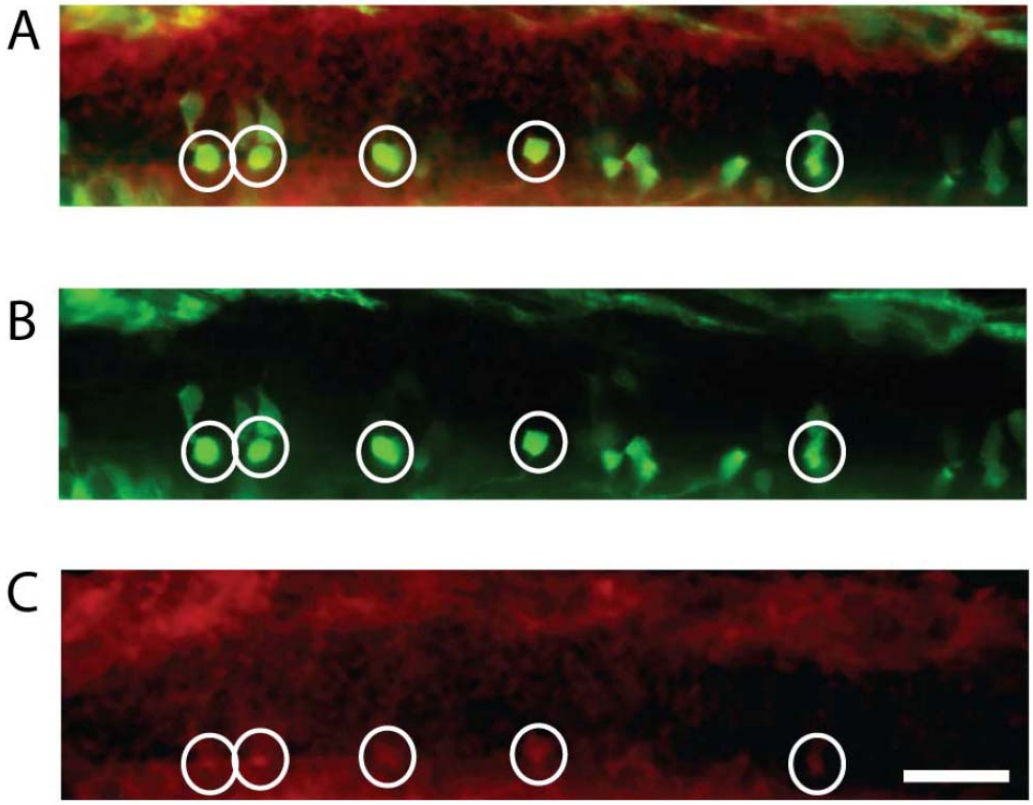

Supplemental Figure 4. KA neurons are somatostatin-positive as shown by immunostaining for somatostatin in *Gal4s1003t.* A-C) Immunostaining for somatostatin. **A,B)** Label of KA neurons expressing GFP (green). **A,C)** Somatostatin immunostaining (red). Scale bar is 25μm.

Supplemental Figure 5

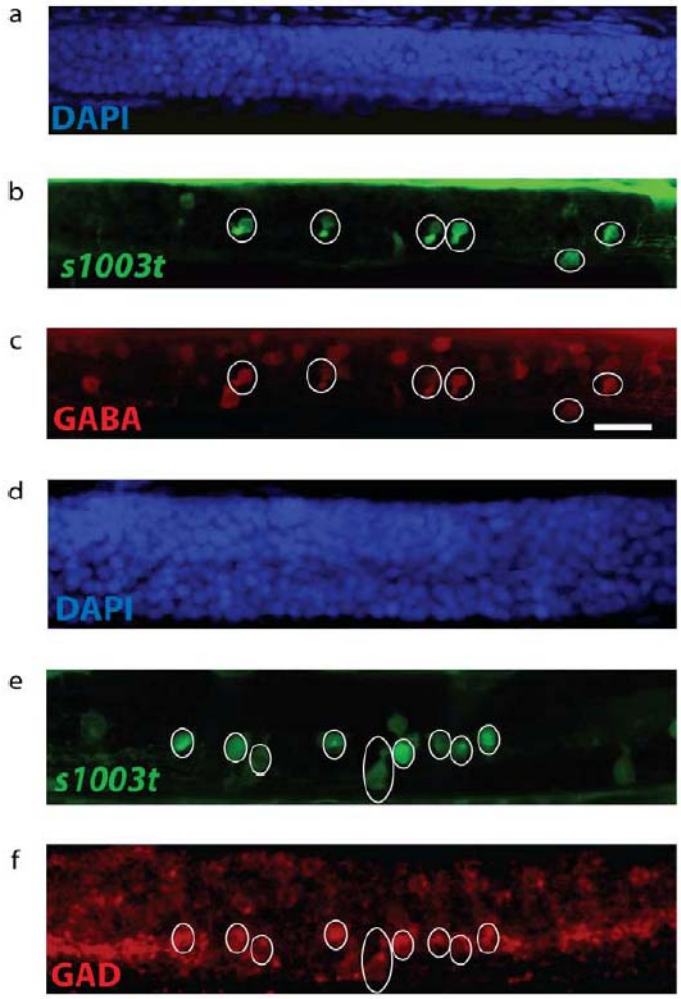

Supplemental Figure 5. KA neurons are GABAergic as shown by immunostaining for GABA and GAD65/67 in *Gal4s1003t.* a-c, Immunostaining for GABA. **a,** Dapi image. **b,** Sparse label of a single KA neuron expressing GFP. **c,** GABA immunostaining. Note on the left side of the picture, the presence of two ventrally located GABAergic positive cells which are not expressing in *Gal4s1003t* indicating that the *Gal4s1003t* line labels only a fraction of KAs. **d-f,** Immunostaining for GABA. **d,** Dapi image. **e,** Sparse label of a single KA neuron expressing GFP. **f,** GAD immunostaining. Scale bar is 25μm.

Supplemental Figure 6

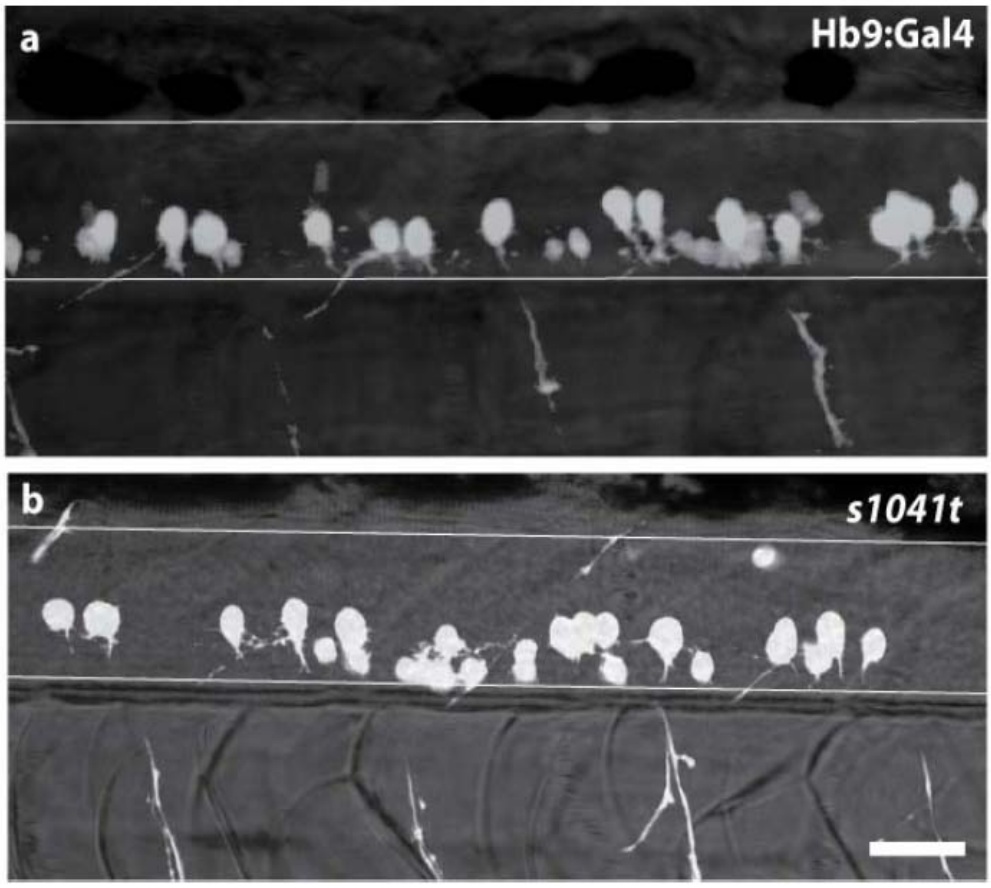

Supplemental Figure 6. Characterization of the motor lines *Gal4s1041t* and Hb9:Gal4. a, *Hb9:Gal4/UAS:Kaede*. **b,** *Gal4s1041t/UAS:Kaede.* In both lines, the Kaede pattern reveals ventral cells with projections on the muscle, assimilated to motoneurons. Lateral views, scale bar is 25µm.

Supplemental Figure 7

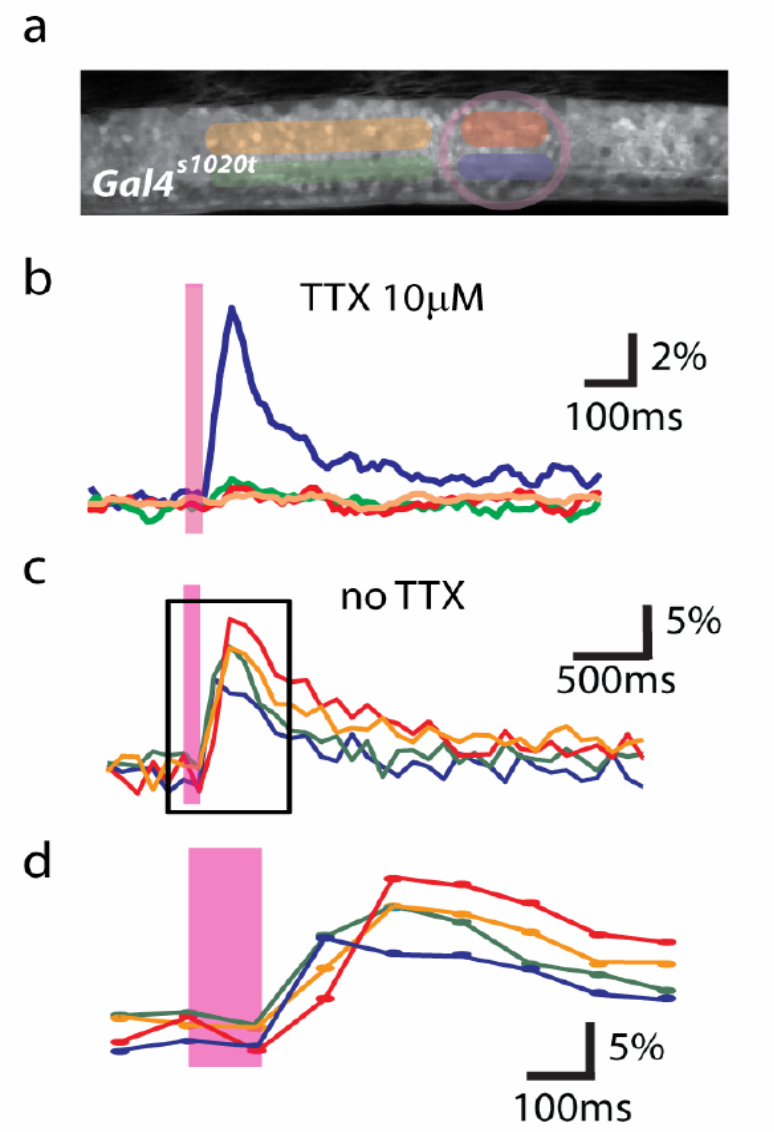

Supplemental Figure 7. Calcium imaging shows the activation of KAs following a brief pulse of UV light. a) When 10µM TTX is injected in the spinal cord, the calcium transients induced by the UV pulse shows that the ventral zones, where KA neurons are located, activates only in the region hit by UV (blue trace), but not rostrally in the ventral domain (green trace), or in the dorsal regions (red, orange traces). **b)** On the contrary, the activation propagates to the entire spinal cord when ringer only is injected. **c)** The black rectangle delimitates the region zoomed depicted in **b)**. Note that the activation start in the ventral regions where KA neurons are located. Expected oscillations at 20Hz in the calcium transients cannot be seen due to the low frequency of acquisition (10Hz).

Supplemental Figure 8

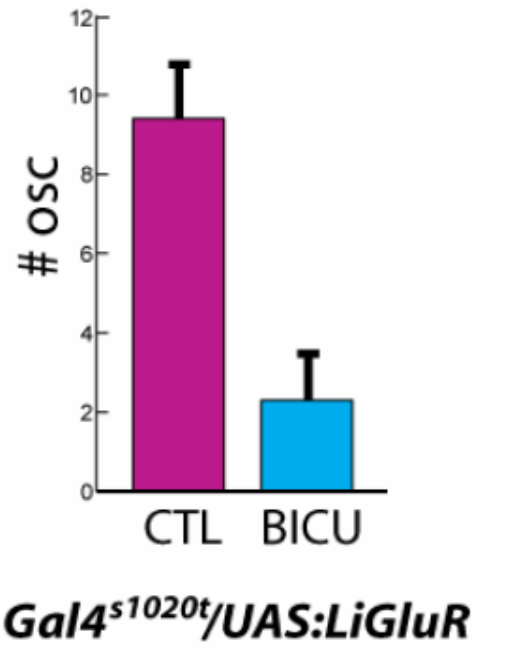

Supplemental Figure 8. GABA involved in the light-induced response of *Gal4s1020t*/UAS:LiGluR. Light-induced swimming in *Gal4s1020t*/*UAS-LiGluR* larvae is greatly reduced by injection of bicucculine 40μM, supporting the idea that KA neurons provide input to the CPG via GABAergic synapses.

Supplemental Figure 9

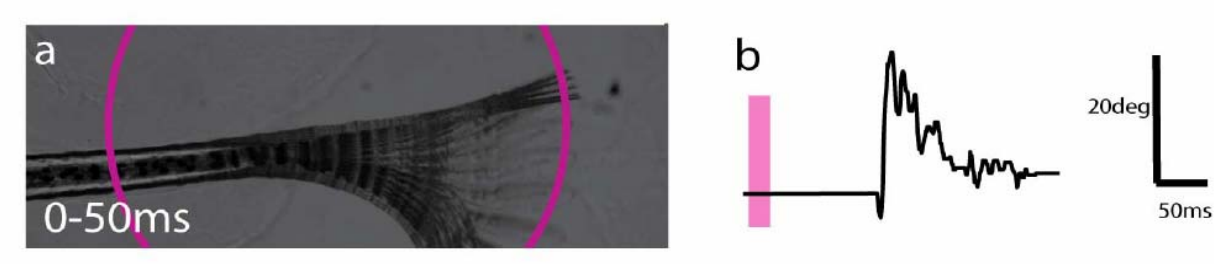

Supplemental Figure 9. Behavioural response of the line s1041t after a high power UV pulse (2-5mW/mm2) shows a large bend. a) Superimposed image of the tail motion with in the first 50ms. **b)** Deflection angle over time.

Chapter 5:

Emergence of patterned activity in the developing zebrafish spinal cord

This work has been published in the following article and is reprinted in full with permission*:*

Warp E, Agarwal G, Wyart C, Friedmann D, Oldfield CS, Conner A, Del Bene F, Arrenberg AB, Baier H, and Isacoff EY, “Emergence of patterned activity in the developing zebrafish spinal cord”, *Current Biology,* Jan , 2012.

For this work, E.W., G.A., C.W., H.B., and E.Y.I. designed the experiments and analytical approaches. E.W. performed the time lapse, heptanol, and the acute and chronic NpHR experiments. D.F. and C.S.O. contributed to data collection and analysis of the chronic NpHR experiments. E.W. and G.A. wrote the MATLAB scripts to analyze the calcium imaging movies and performed the analysis. E.W. and C.W. set up the photomanipulation system. E.W. and A.C. performed the *BGUG* imaging. F.D.B. assisted with experiment set-up, and A.B.A. made the *UAS:NpHR-mCherry* transgenic line. E.W. and E.Y.I. wrote the manuscript with feedback from the other authors.

SUMMARY

Background

Developing neural networks display spontaneous and correlated rhythmic bursts of action potentials that are essential for circuit refinement. In the spinal cord, it is poorly understood how correlated activity is acquired and how its emergence relates to the formation of the spinal central pattern generator (CPG), the circuit that mediates rhythmic behaviors like walking and swimming. It is also unknown whether early, uncorrelated activity is necessary for the formation of the coordinated CPG.

Results

Time-lapse imaging in the intact zebrafish embryo with the genetically encoded calcium indicator GCaMP3 revealed a rapid transition from slow, sporadic activity to fast, ipsilaterally correlated, and contralaterally anticorrelated activity, characteristic of the spinal CPG. Ipsilateral correlations were acquired through the coalescence of local microcircuits. Brief optical manipulation of activity with the light-driven pump halorhodopsin revealed that the transition to correlated activity was associated with a strengthening of ipsilateral connections, likely mediated by gap junctions. Contralateral antagonism increased in strength at the same time. The transition to coordinated activity was disrupted by long-term optical inhibition of sporadic activity in motoneurons and ventral longitudinal descending interneurons and resulted in more neurons exhibiting uncoordinated activity patterns at later time points.

Conclusions

These findings show that the CPG in the zebrafish spinal cord emerges directly from a sporadically active network as functional connectivity strengthens between local and then more distal neurons. These results also reveal that early, sporadic activity in a subset of ventral spinal neurons is required for the integration of maturing neurons into the coordinated CPG network.

INTRODUCTION

Spontaneous activity is common to developing networks, occurring in the embryo during periods of concentrated axonal growth and synaptogenesis [1]. A hallmark of this activity is correlated population activity. Such correlations are hypothesized to guide the development of neural circuits [2], as demonstrated in the visual system where disruption of correlated retinal waves causes abnormal circuit development in downstream targets [3]. A transition from sporadic, cell-autonomous activity to correlated rhythmic activity has been observed in brain stem [4], cortex [5], and hippocampus [6], reflecting the emergence of connectivity and suggesting that early,

sporadic activity may be necessary for the formation of more mature, correlated networks.

Early in the development of the motor system, cell-autonomous spontaneous calcium transients are observed in spinal cord neurons [7] before the maturation of the synaptic network. Later, spinal cord neurons display correlated patterns of spontaneous activity, beginning with bilaterally synchronized bursts of action potentials [[8] and [9]] that convert to alternation between the left and right sides when γ-aminobutyric acid $(GABA)_A$ and glycine receptor signaling switches during development from depolarizing to hyperpolarizing [10]. In vertebrates, manipulation of correlated spontaneous activity in the spinal cord disrupts axon guidance [11], the balance between excitatory and inhibitory synaptic strength [12], and the formation of the central pattern generator (CPG) [13], which generates oscillatory rhythms for locomotion into adulthood [14]. Though cholinergic activity has been shown to be necessary for the maturation of rhythmic alternation between the two sides of the mammalian spinal cord [13], it is unknown whether activity influences the acquisition of correlations on the same side of the cord and which cell types may mediate this activity dependence.

We investigated the emergence of correlated patterns of spontaneous activity in vivo in the developing zebrafish spinal cord locomotor system using the genetically encoded calcium indicator GCaMP3 [15] to image spontaneous activity noninvasively at single-cell resolution in identified cells. The imaging identified a remarkably rapid transition from sporadic, uncorrelated activity to rhythms characteristic of the locomotor CPG with ipsilateral correlation and contralateral alternation. Acute optical manipulation of activity revealed that the development of functional connectivity underlies the emergence of the coordinated activity. Chronic optical inhibition of activity in motoneurons and ventral longitudinal descending (VeLD) interneurons early in the transition period disrupted the integration of maturing neurons into the correlated network, suggesting that the emergence of the coordinated CPG is activity dependent.

RESULTS

Emergence of Correlated Activity

In vivo calcium imaging with genetically encoded indicators has been used successfully to image neural activity in zebrafish embryos [16] and larvae [[17] and [18]]. We employed GCaMP3 [[15] and [18]] for its high baseline fluorescence and high signal-to-noise ratio [15]. GCaMP3 and the light-gated inhibitory chloride pump halorhodopsin (NpHR) [[19] and [20]], were targeted to neurons of interest using the *UAS/Gal4* system.

Spontaneous activity in the zebrafish spinal cord is restricted to ventral neurons of the motor system [21]. We used the *Gal4s1020t* line developed in an enhancer trap screen [22] to target a subset of these spontaneously active cells (see Figure S1 available

online). We have previously characterized this line to contain primary and secondary motoneurons and Kolmer-Agduhr (KA) ascending interneurons in the spinal cord at 5 days postfertilization (dpf) [23]. At 1 dpf, single-cell imaging with *Brn3c:GAL4, UAS:mGFP* (BGUG) [22] also revealed targeting to descending interneurons (Figures S1C and S1E). The *Gal4* insert for this line is near the *olig2* gene [23], which exhibits an identical expression pattern and has been shown at 1 dpf to target motor neurons, KA cells, and VeLD interneurons, as well as bromodeoxyuridine (BrdU)-incorporating cells along the midline [24]. We therefore interpret the descending interneurons to be VeLDs.

Single-cell electrophysiological recordings have identified three key neuron types—primary motoneurons, VeLD interneurons, and IC (ipsilateral caudal) descending interneurons—to be always active during spontaneous events in the zebrafish spinal cord at 20–24 hpf [21]. In the *Gal4s1020t* line, we could image the population dynamics of spontaneous activity in primary motoneurons and VeLDs, two of the three key neuron types.

During embryonic development, zebrafish display spontaneous bursts of action potentials in the spinal cord that are associated with spontaneous contractions of the tail [[25], [26] and [21]]. We imaged spontaneous calcium activity in *UAS:GCaMP3/ Gal4s1020t* fish at 18 hpf, an hour after the onset of spontaneous behavior [25], and at 20 hpf, when electrophysiological correlation between pairs of spinal neurons has been previously observed [21], and when there is evidence for both electrical and chemical synapse formation in the zebrafish spinal cord [[26] and [21]]. Calcium imaging was performed on embryos paralyzed with ∝-bungarotoxin to eliminate spontaneous contractions, performed from a dorsal view to simultaneously observe cells on the left and right sides, and centered on somites 5 and 6. Spatial regions corresponding to single active neurons (e.g., regions outlined in Figures 1A and 1D) and intensity traces over time (e.g., time series data in Figure 1B and 1E) were extracted from movies using a semiautomated toolbox [27].

Though activity was present at 18 hpf, it was sporadic, with long-duration events (Figures 1A–1C; Movie S1) that were rarely associated with events in other ipsilateral cells and with no obvious relationship between the left and right sides of the cord. We did observe some correlation between ipsilateral cells at 18 hpf, but this was just between small subsets of nearby cells (e.g., Figure 1B, cells 1 and 2). In contrast, at 20 hpf events were shorter lasting, tightly correlated between nearly all ipsilateral cells, and organized in bursts of alternation between the left and right sides (Figures 1D–1F; Movie S2), as observed previously [16]. The left/right rhythmicity is reminiscent of activity patterns observed during swimming but is significantly slower at this early coiling stage that precedes swimming [28]. We also observed fish that exhibited near-continual alternating bursts (Figure S1F).

Time-lapse calcium imaging was used to characterize the transition between the uncorrelated and correlated network states. Calcium imaging movies of 4 min duration were taken every half hour between 17.5 and 21 hpf. To quantify changes in activity patterns, we calculated the correlation of GCaMP traces for all cell pairs in individual

movies. Pairwise correlation matrices of single-cell traces in an example fish (Figure 2A) showed little correlation at early time points, and the few cell pairs that were correlated were weakly so. With time, correlations between ipsilateral neurons became stronger, whereas neurons on opposite sides of the cord became anticorrelated.

Pooled correlation data across fish showed that ipsilateral cells went from weak to strong correlation, reaching a maximum at 20 hpf, 3 hr after the onset of spontaneous behavior [25] (Figures 2B and 2C). During this period, contralateral cells became increasingly anticorrelated (Figures 2B and 2C). By 20 hpf, rhythmic oscillations were apparent (Figures 1F and 2B, right), indicating that the components of a CPG are in place. Increases in ipsilateral correlation and decreases in event duration were detected in individual tracked cells that became active early (e.g., starting at 18 hpf, Figure S2A) as well as for cells that became active later (e.g., starting at 19.5 hpf, Figure S2B), suggesting that maturation of the circuit involves the progressive addition of cells, each of which goes from an initial state of uncorrelated slow activity to network-associated fast activity.

Ipsilateral Synchronization through Coalescence of Local Correlated Groups

Spatiotemporal maps of correlated ensembles in most fish (6/9) at early stages showed multiple nonoverlapping correlated groups on the same side of the cord (Figure 3, 18.5 hpf, left side). With time, the correlations between cells strengthened and the correlated groups increased in size, to eventually include virtually all ipsilateral cells in the field of view (Figure 3, e.g., 20 hpf; Figure S3A). Within these correlated ensembles, cells became more precisely time-locked (i.e., shorter lag times) during this early period of spontaneous activity (Figure S3B). In addition, event amplitude variability decreased during this period (Figure S3C).

In younger embryos (17.5–18.5 hpf), the distance between cells participating in a synchronous event was relatively small, (i.e., correlations were seen between small numbers of neighboring cells), whereas temporally coupled cells covered a broader spatial region in older embryos (e.g., 20–21 hpf) (Figure S3D). Conversely, temporal spread was broad at younger stages but tight at later stages as events became more accurately time-locked between ipsilateral cells (Figure S3D). Thus, ipsilateral correlation is accomplished through the coalescence of local correlated groups, which converts small events that are weakly correlated in small groups of cells into large events that occur synchronously on the entire side of the spinal cord. Although the zebrafish spinal cord develops in a rostral to caudal sequence [29], ipsilateral correlations do not emerge in a rostral to caudal pattern, at least in the region of cord that we imaged.

Increased Functional Connectivity Accompanies Emergence of Correlated Activity

Both chemical and electrical synapses have been implicated in mediating spontaneous activity in the spinal cord [9]. Paired recordings have shown that gap junctions play an

essential role in the connectivity of the embryonic zebrafish spinal cord [21]. Additionally, uncoupling gap junctions with heptanol or by intracellular acidification eliminates spontaneous activity at 19–24 hpf, whereas blockers of chemical transmission do not [26]. In older embryos (20–20.5 hpf), heptanol eliminated spontaneous activity in all but 3.7% ± 1.6% of cells (n = 11 fish; see Figure S4B for example), whereas 34.7% ± 9.9% of cells remained active in younger embryos (17.5–18 hpf, n = 13 fish; p = 0.002, unpaired Student's t test; see Figure S4A for example). Though these results could be due to off-target effects on calcium or potassium channels, they remain consistent with a model in which gap junctions are important for correlated activity at 20 hpf and younger neurons are more electrically cell autonomous.

To examine this apparent emergence of functional connectivity between ipsilateral cells, we manipulated activity in single cells or in groups of cells and examined the effect on neighboring ipsilateral cells. We used the genetically encoded light-driven chloride pump NpHR, which hyperpolarizes neurons in response to yellow light [19]. GCaMP3 and NpHR were genetically targeted to the same population of ventral spinal neurons in *Gal4s1020t/UAS:GCaMP3/UAS:NpHR-mCherry* [20] fish (Figure S5A). Spatial targeting of NpHR-activating light was accomplished using a digital micromirror device (DMD). Its spatial resolution was tested by photoconversion of the fluorescent protein Kaede, and light could be restricted to single cells (Figure S5E).

Because NpHR-activating 593nm light does not overlap with the excitation or emission spectrum of GCaMP3 [15], calcium events could be imaged simultaneously during NpHR activation. Spontaneous calcium events imaged with GCaMP3 in NpHR-expressing fish were blocked successfully by illumination of 593 nm light at 19 mW/mm^2 (Figures S5B–S5D). As seen earlier, including in other zebrafish neurons [[19] and [20]], light offset triggered rebound excitation (Figures S5C and S5D), allowing us to excite as well as inhibit with a single tool.

We observed striking differences in network responses to NpHR activation between younger and older embryos. Illumination of single cells in younger animals (18–18.5 hpf) caused robust inhibition in the illuminated cell and a rebound excitation upon light-off (Figure 4A) but had no effect on other ipsilateral cells, suggesting low connectivity, where individual cells are functionally independent. In contrast, single-cell illumination at 20–20.5 hpf did not significantly affect activity in either the illuminated cell or in other ipsilateral cells (Figure 4B). However, illumination of a group of cells in a region encompassing two hemi-somites strongly suppressed activity during illumination and evoked rebound excitation upon light-off in both the illuminated cells and nonilluminated ipsilateral neighbors (Figure 4C). Connectivity through electrical synapses can explain the ineffectiveness of NpHR single cell manipulation in the older embryo (Figure 4B), because spread to neighbors of chloride current pumped into an individual cell would reduce the efficacy of the hyperpolarization in that cell. The bidirectionality of electrical synapses can also explain why the inhibition and activation spread to nonilluminated cells in both the rostral and caudal directions (Figure 4D) even though the only spontaneously active ipsilaterally projecting interneurons—the VeLD and IC cells—both have descending axons during this period of development [[21] , [30] and [31]]. In

summary, our data suggest that increased functional connectivity underlies the emergence of ipsilateral correlation observed between 17.5 and 20 hpf (Figure 2C).

Triggered Rhythmic Oscillation with NpHR Reveals Acquisition of Contralateral Antagonism

Supraspinal activation of the spinal CPG is bilateral for forward swimming but triggers an alternating response in downstream spinal targets [[32] and [28]]. This behaviorally relevant coordinated firing relies on robust inhibitory connections between the two sides of the cord [14]. We tested whether the left and right sides of the cord were functionally antagonistic in the embryo by assessing network responses to bilateral stimulation evoked by NpHR rebound excitation that was confined to the neuronal cell types expressing in the *Gal4s1020t* line. *Gal4s1020t/ UAS:GCaMP3/UAS:NpHR-mCherry* embryos were illuminated bilaterally over a four-somite region for 15 s, a duration that reliably triggered rebound excitation at light-off (Figures S5C and S5D; Figures 5A and 5B). At 18 hpf, bilateral rebound activation triggered calcium events on the left and right sides of the cord with the initial wave of activity occurring nearly simultaneously on the two sides (Figure 5A). In contrast, at 20 hpf, the rebound excitation triggered a wave of activity first on one side and then, after a substantial delay, on the other side (Figure 5B). The firing then alternated back and forth between the two sides, similar to what was seen in spontaneous locomotor-like activity (Figure 1F and 2B, right). The delay between correlated events (two or more cells participating) on the left and right sides following light offset increased significantly between 18 and 21 hpf ($p < 10^{-3}$, paired Student's t test, n = 6 fish; Figure 5D), suggesting that contralateral antagonism is strengthened during this period.

Developmental Transition Disrupted by Inhibition of Activity

To determine the influence of uncorrelated spontaneous activity on the formation of the correlated network and the locomotor CPG, we inhibited spontaneous events for 1 hr with NpHR during the period of transition from uncorrelated to correlated activity (18 to 19 hpf), while imaging population activity with GCaMP3 (Figure 6). To prevent cumulative desensitization of NpHR during long-term activation, we applied a 500 msec pulse of blue light (410 nm) every 10 s [[33] and [19]], concurrently with yellow light using a double bandpass filter to prevent rebound stimulation with yellow light off (Figure 6A). Light was applied to the full imaged region covering both sides of the cord and approximately six somites, centered at somites 5 and 6.

Activation of NpHR from 18 to 19 hpf with yellow/blue light resulted in a reduction in the frequency of spontaneous events during the 18 to 19 hpf period in NpHR-positive fish as compared to three control groups: (1) NpHR-negative fish without yellow/blue light, (2) NpHR-negative fish with yellow/blue light, and (3) NpHR-positive fish without yellow/blue light (Figure 6B). NpHR-induced inhibition reduced activity by 66% initially (18 hpf) and by 53% by the end of the illumination period (19 hpf) compared to GCaMP only (group 1) controls (Figure 6B). An intermediate decrease in the frequency of spontaneous events was observed in NpHR-positive fish that did not receive the

yellow/blue light protocol (group 3). This effect was attributed to the fact that the 488 nm imaging light overlaps with the NpHR excitation spectrum and activates the pump by approximately 18% [19]. To eliminate potential effects of the imaging light on the frequency of spontaneous events, we imaged the population patterns only at the end of the experiment (22 hpf) for NpHR without yellow/blue light controls.

We observed a substantial reduction in pairwise ipsilateral correlation in the experimental fish (NpHR-positive fish receiving the yellow/blue light protocol) when compared to controls (Figure 6C), though the four groups did not differ at baseline at 18 hpf (ipsilateral correlation one-way analysis of variance [ANOVA], $p = 0.22$). This reduction in correlation became evident at 20.5 hpf and continued through 22 hpf (Figure 6C). Additionally, the three controls were similar at 22 hpf, indicating that neither NpHR expression alone, possible NpHR constitutive activity alone, nor yellow/blue light alone disrupts the emergence of correlated activity.

An examination of the activity in control and experimental fish showed that by 22 hpf, the experimental fish had a larger proportion of active cells with immature phenotypes (Figure 7B). As shown above (Figure 1, Figure 2 and Figure 3) and in control fish (Figure 7A), most active cells were part of an ipsilateral, correlated network in the older embryo, with a small minority of the cells showing long-duration, uncorrelated events, and usually residing more medially in the spinal cord (Figures 1D and 1E; Figure 7A, asterisks). In contrast, in experimental fish, approximately 50% of the active cells were uncorrelated, with long-duration events (Figure 7B, asterisks; Figure 7C), displaying the more immature activity pattern that we observed in our single-cell tracking (Figure S2). Associated with this perturbed pattern of activity, we found that in the experimental animals, a larger fraction of the active cells were located closer to the midline of the spinal cord (Figure 7B, asterisks; Figure 7D), where more immature cells, like BrdU-incorporating progenitor cells, have been shown to reside [24]. Groups did not differ in events kinetics (width at half maximum one-way ANOVA, $p = 0.30$) nor the location of active cells (distance to midline one-way ANOVA, $p = 0.28$) at 18 hpf before activity manipulation. The number of active cells per field of view was not significantly different between experimental and control fish (Figure S6), suggesting that the optical inhibition of activity in motoneurons and VeLDs perturbed the developmental transition by reducing the efficiency with which cells that originated at the midline joined the lateral correlated network.

DISCUSSION

Rapid Emergence of Ipsilateral Correlation

Optical measurements of spontaneous activity in genetically selected ventral spinal neurons in live zebrafish revealed a rapid transition from uncorrelated, sporadic slow activity to ipsilaterally correlated fast activity. The transition to correlated activity could be accounted for by the formation of electrical connections, which initially couple nearby

neurons into local microcircuits and then merge to include the majority of active ipsilateral neurons into a single coupled network.

Our observations in vivo are consistent with observations made previously. In *Xenopus*, cell-autonomous calcium events are seen in dissociated spinal cultures and in the isolated spinal cord, with short-duration calcium events becoming correlated between small groups of neurons later in development [7]. In isolated spinal cord of rodent [34] and chick [35], spontaneous events, which are correlated between motoneurons and interneurons, propagate between multiple spinal segments [35]. In the zebrafish spinal cord, cell-autonomous calcium events have been detected in axon-less cells of the 19–26 hpf embryo in imaging experiments but likely overlap minimally with the events we detected due to their very slow kinetics [36]. Correlated depolarizations have been observed between pairs of ventral neurons in dual-cell electrophysiological recordings in 20–24 hpf zebrafish embryos [21], which likely correspond to the correlated calcium events we observed with GCaMP. During swimming, waves of activity propagate down the ipsilateral spinal cord, resulting in nearby motoneurons being more correlated than distant ones [[14] and [28]]. A similar, though slower, rostral to caudal propagation is observed in spontaneously active motoneurons of 24 hpf zebrafish embryos [16]. We observed that nearby spinal neurons became correlated before distant neurons, suggesting that more mature rostral to caudal relationships are established as the first connections are formed between neurons.

The changes in global activity patterns that we observed were associated with a rapid strengthening of functional connectivity between ipsilateral neurons, as seen from the change in the spread of NpHR inhibition and rebound excitation to nonilluminated cells, suggesting that early activity is cell autonomous and later activity depends on network interactions. The initiation of rhythmic spontaneous events in the rodent and chick spinal cord has been shown to depend on recurrent excitation between GABA-, glycine- and glutamatergic interneurons and cholinergic motoneurons [[1] and [9]]. The ipsilateral network interactions that we observed in the zebrafish appear to be mediated via electrical synapses, as shown in previous studies [[26] and [21]], though chemical synapses may also play a role. Gap junctions also appear to play an integral role in the propagation of correlated spontaneous activity in the spinal cord of rodents [9] and chicks [37] and appear to form some of the first connection in the developing retina [38], cortex [39], and hippocampus [6].

Contralateral Antagonism Emerges Concurrently with Ipsilateral Correlation

We found that as the coupled ipsilateral network was established there also emerged a superstructure in which the spontaneous activity alternated from side to side, a fundamental characteristic of the CPG, which has been shown to involve contralateral inhibition through chemical synapses [14]. Earlier lesion studies have indicated that spontaneous activity and left/right alternation in the spinal cord of embryonic zebrafish does not rely on input from the brain [[25] and [40]], suggesting that the network mediating this rhythmic activity is endogenous to the spinal cord. Given that, among the cells expressing in our Gal4 line, only KAs and VeLDs project within the spinal cord,

and, of these, only the VeLDs are active in the first day of development; it therefore appears that the VeLDs, and neurons that they drive, can account for a minimal circuit for locomotor-like activity and behavior.

In rats and mice, spontaneous events are at first synchronized between both sides of the spinal cord and begin to alternate between sides around birth when the activation of $GABA_A$ and glycine receptors become hyperpolarizing [[8] and [9]]. We did not observe a period of synchronized spontaneous events between the left and right sides of the spinal cord in the zebrafish. Rather, the first coordinated patterns consisted of both ipsilateral correlation and contralateral alternation (Figures 2B and 2C). We observed similar patterns of alternating activity with bilateral rebound activation with NpHR. The similarity between spontaneous and NpHR rebound-evoked alternation suggests that a bilateral drive may be responsible for triggering the earliest alternating bursts of locomotor-like activity in the embryonic zebrafish.

Activity-Dependent Emergence of the CPG

Inhibition of activity for 1 hr with NpHR during the transition from sporadic to patterned activity disrupted the emergence of correlated, short duration, rhythmic activity, indicating that early activity is either instructive or permissive for the maturation of the spinal network. In the normal development of the spinal cord, our imaging revealed that cells first display long-duration, uncorrelated events before transitioning to brief, correlated activity as they establish functional connectivity with other neurons. This transition occurred in neurons that became active early (e.g., Figure S2A) and in neurons that matured and integrated into the network at a later stage (e.g., Figure S2B). Light-driven reduction of activity with NpHR reduced the overall ipsilateral correlation by reducing the fraction of cells that made the transition to brief, correlated activity. As seen in control fish experiencing normal activity, the uncorrelated cells tended to be located more medially in the spinal cord, except that in the fish whose activity had been inhibited by light, they went from being a small minority to being roughly half of the active cells (Figure 7).

These effects are striking given that the inhibition of activity is only by approximately half, it lasts for only 1 of the 3 hr of the developmental transition, and it occurs in only a subset of ventral spinal neurons: the VeLD interneurons and motoneurons (the KAs, also targeted in the *Gal4s1020t* line, have not been shown to display rhythmic spontaneous activity [21]). These observations imply that early spontaneous activity in VeLD interneurons and/or motoneurons, or in neurons that they drive, is required for the integration of less mature neurons into the correlated network and for the acquisition of normal patterns of population activity. The effect that we observe from inhibiting activity between 18 and 19 hpf was not present until 20.5 hpf, suggesting that inhibition of activity in the few cells that are active early likely alters the integration of other neurons that mature later.

Previous studies have shown that calcium fluctuations play an essential role in developmental processes such as cell migration [41], axon guidance [42], and the

expression of the membrane proteins that control cell excitability [43]. It is possible that some or all of these mechanisms underlie the effect of activity manipulation that we observe. For example, a lateral position could be required for integration into the correlated network, and blocking migration to this position could subsequently reduce the number of coupled cells. It has recently been shown that endogenous patterns of spontaneous activity are required for the proper development of coordinated patterns of activity in the motor system of an invertebrate [44]. Here we show that early uncorrelated spontaneous activity is required for the formation of coordinated motor circuits in a vertebrate.

CONCLUSION

Correlated, rhythmic spontaneous activity is a common feature of developing networks and is essential for normal circuit maturation. By applying noninvasive optical tools to image activity, we observed a rapid transition from sporadic, long-duration, uncorrelated activity to fast, correlated, and rhythmic spontaneous activity in the spinal cord of the intact developing zebrafish. Correlated activity between neurons on the same side of the cord was found to emerge through the formation of small local microcircuits and their subsequent coalescence into a single ipsilateral network, at the same time as side-to-side alternation emerged. This transition to patterned locomotor-like population activity is perturbed by optical inhibition of motoneurons and VeLD interneurons during the transition period, impeding the integration of maturing neurons into the coordinated network. These results indicate that the formation of the spinal CPG is dependent on activity that occurs before functional connectivity is robustly established in the network.

EXPERIMENTAL PROCEDURES

The following transgenic lines were used for experiments (naming according to official zebrafish nomenclature): *Et(−0.6hsp70l:Gal4-VP16)s1020t* (a.k.a. *Gal4s1020t*) [22]; *Tg(UAS-E1b:Kaede)s1999t/+* (a.k.a. *UAS:Kaede*) [22]; and *Tg(UAS:NpHR-mCherry)s1989t* (a.k.a. *UAS:NpHR)* [20], as well as *UAS:GCaMP3* [18].

Animal experiments were done under oversight by the University of California institutional review board (Animal Care and Use Committee). Imaging, photomanipulation, and analysis methods are described in the Supplemental Information.

Figure 1

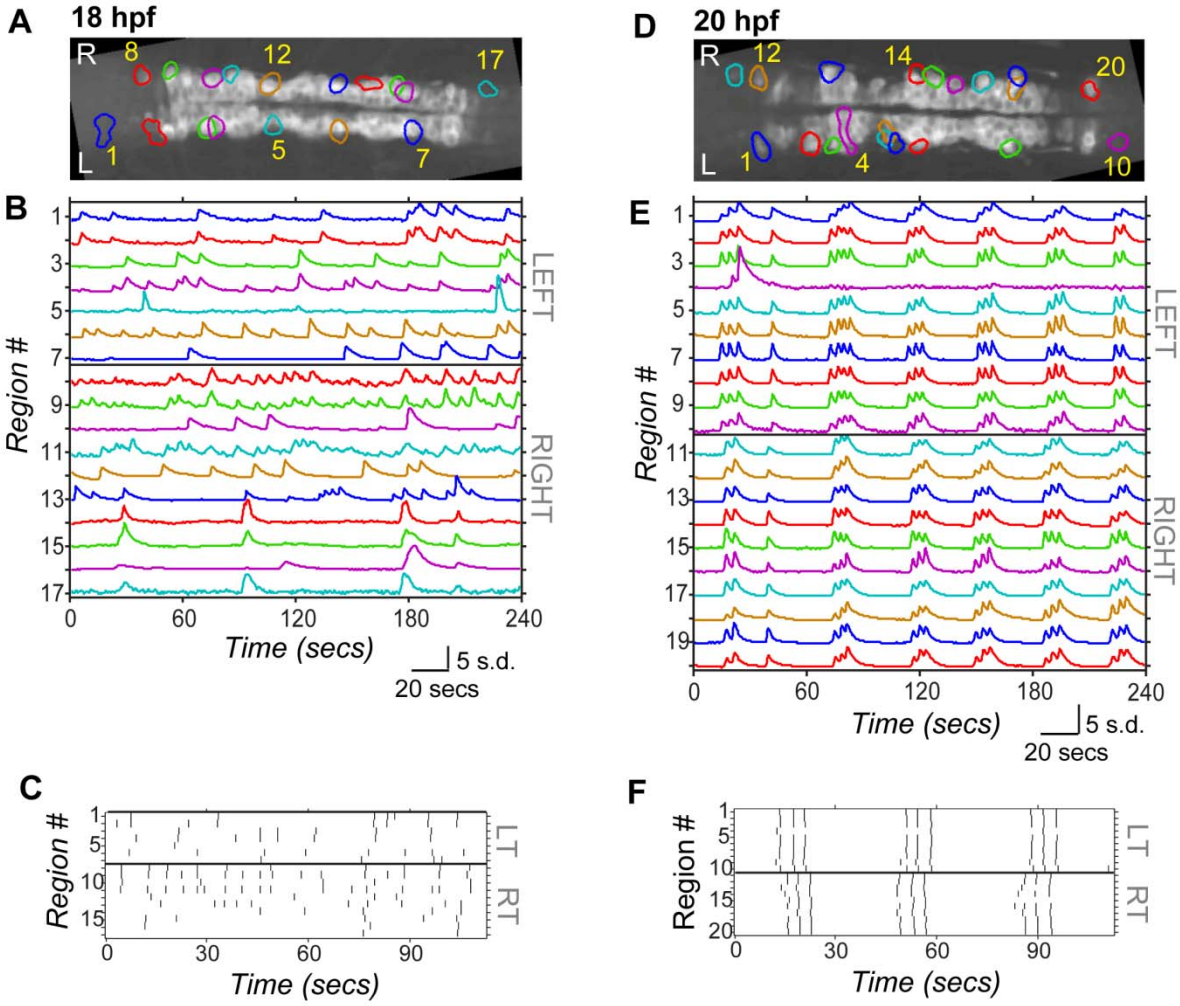

Figure 1. Spontaneous Calcium Activity in Spinal Neurons Progresses from Sporadic to Locomotor-Like During Embryonic Development. GCaMP3 activity in single neurons in one example embryo at 18 hpf (left) and 20 hpf (right). (A and D) Dorsal views of GCaMP3 baseline fluorescence with active regions circled (rostral left; imaged area somites 4–8). (B and E) Normalized intensity traces for active regions (identified on y axis) for the left and right sides of the cord, with amplitude corresponding to standard deviations (s.d.) of fluorescence away from baseline. At 18 hpf (B), ipsilateral neurons have little correlated firing, though some synchronization is observed (e.g., cells 8 and 9). At 20 hpf (E), ipsilateral neurons are tightly synchronized, with few exceptions (e.g., cell 4; note elongated shape extending to the midline). (C and F) Raster plots of detected events for subsection of data in (B) and (E). At 18 hpf (C), population activity is uncoordinated. By 20 hpf (F), ipsilateral cells are synchronized, contralateral cells alternate, and a higher order left/right bursting organization is observed. See also Figure S1.

Figure 2

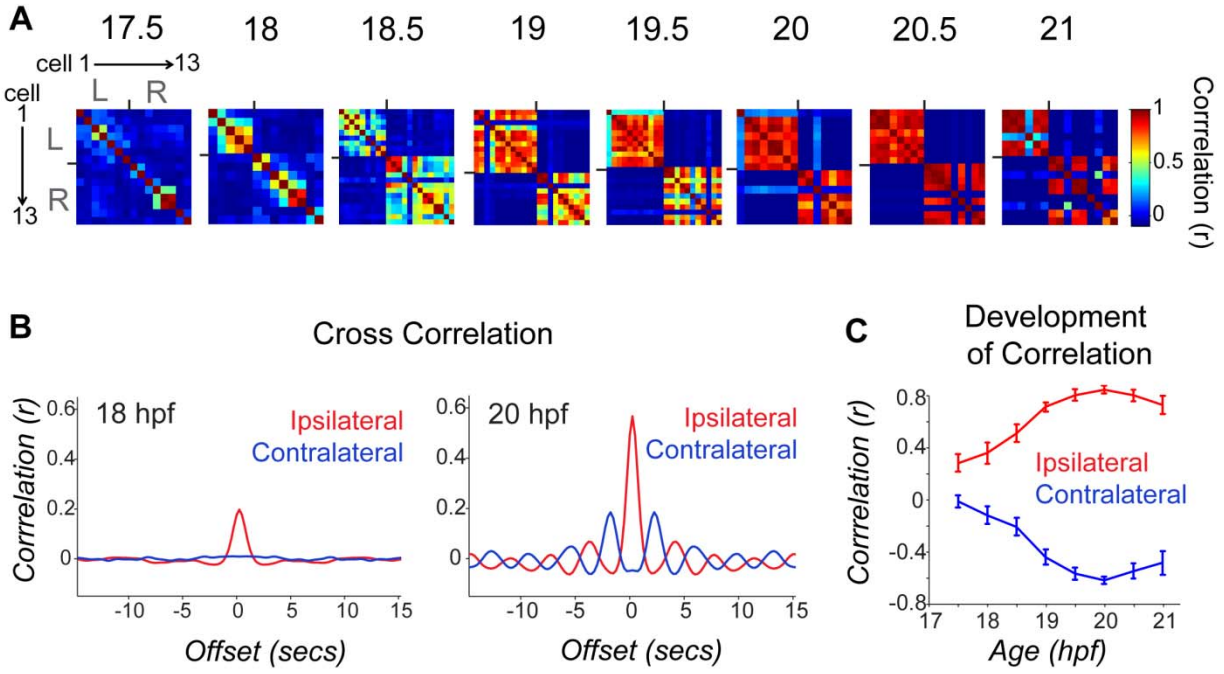

Figure 2. Pairwise Cell Relationships Progress from Independent to Ipsilaterally Correlated and Contralaterally Anticorrelated during a Short Period of Development. (A) Correlation matrices of single-cell traces through the development of an example embryo. Each pixel represents a pairwise comparison between two cells, with high correlation values in red and perfect autocorrelation along the diagonal. Cells are sorted left to right and top to bottom as shown for 17.5 hpf. Ticks mark border between left and right cord and bound a high degree of ipsilateral correlation observed at later time points. (B) Cross-correlation shows a strengthening of ipsilateral coupling between 18 and 20 hpf and acquisition of oscillatory rhythm by 20 hpf. Cross-correlation was calculated by averaging time-shifted correlation data for all ipsilateral and contralateral cell pairs in individual movies, pooled across nine different fish. (C) Average pairwise correlations for synchronous events comparing ipsilateral and contralateral cell pairs from individual time-lapse movies acquired from fish ages 17.5 to 21 hpf and pooled across fish. We observed a significant difference between ipsilateral correlations in younger versus older embryos (18 hpf, $r = 0.272 \pm 0.082$; 20 hpf, $r = 0.761 \pm 0.031$; $p < 10^{-3}$, paired Student's t test; n = 9 fish) and a significant increase in the anticorrelation of contralateral cells (18 hpf, $r = -0.207 \pm 0.067$; 20 hpf, $r = -0.710 \pm 0.028$; $p = < 10^{-3}$, paired Student's t test; n = 9 fish). n = 9 fish for 18–21 hpf; n = 4 fish at 17.5 hpf. Error bars = SEM. See also Figure S2.

Figure 3

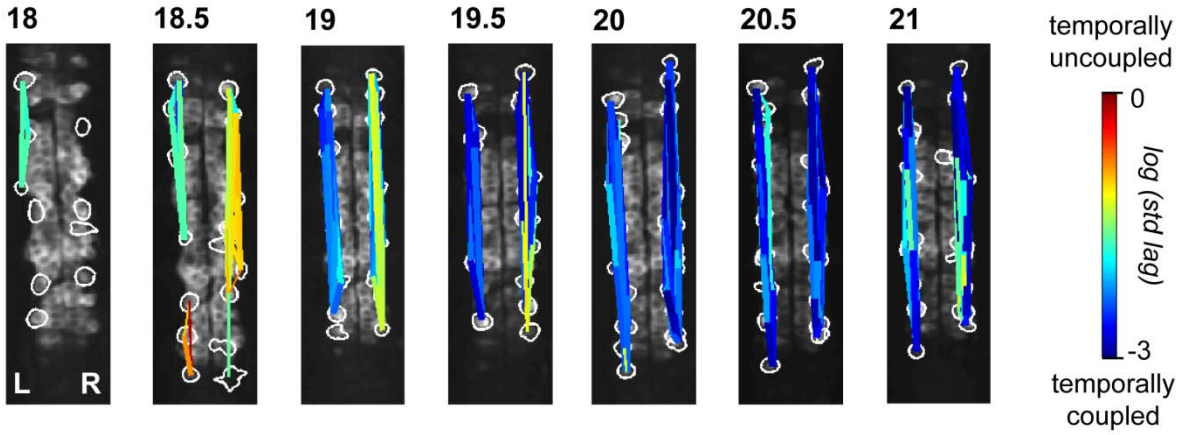

Figure 3. Ipsilateral Correlation Is Acquired through the Progressive Synchronization of Local Subgroups of Cells. Spatial maps of correlated groups in an example fish from 18 to 21 hpf show small local circuits containing a few cells at 18 and 18.5 hpf that expand into full correlation of each side at later stages. Correlations between all cell pairs were calculated and lines were drawn between cell pairs with correlations greater than 0.2, with thicker lines representing stronger correlation. Line color represents the log of the standard deviation of the lags between event start times of cell pairs and shows an overall increase in temporal precision between ipsilateral pairs as development progresses. See also Figure S3.

Figure 4

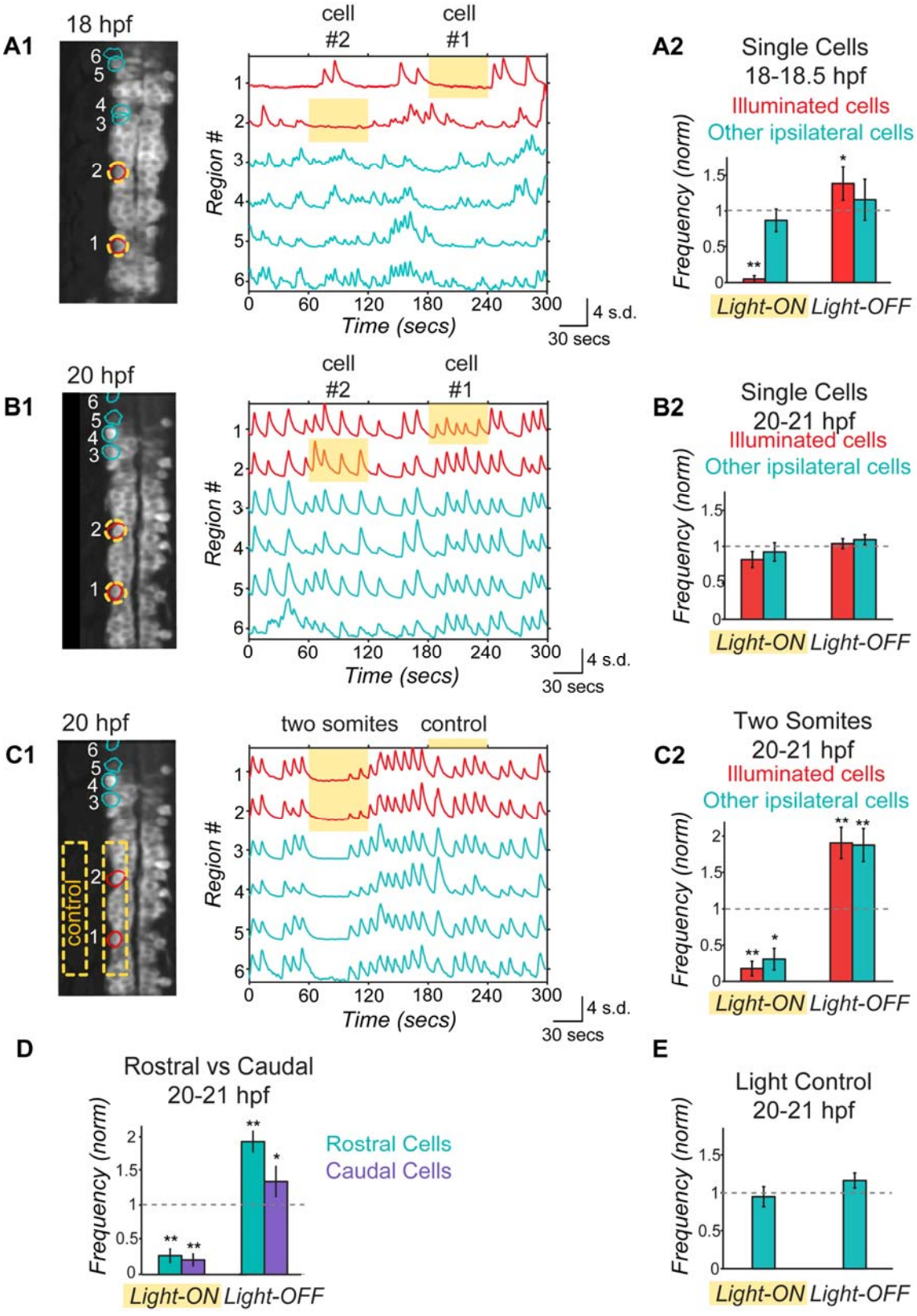
A1
18 hpf
cell #2
cell #1
Region #
Time (secs)
4 s.d.
30 secs
A2
Single Cells
18-18.5 hpf
Illuminated cells
Other ipsilateral cells
Frequency (norm)
Light-ON Light-OFF
B1
20 hpf
B2
Single Cells
20-21 hpf
C1
20 hpf
two somites
control
C2
Two Somites
20-21 hpf
D
Rostral vs Caudal
20-21 hpf
Rostral Cells
Caudal Cells
E
Light Control
20-21 hpf

Figure 4. Optical Manipulation of Targeted Network Components with NpHR Reveals Changes in Functional Connectivity between Ipsilateral Neurons during Development. (A and B) Single-cell optical manipulation of spontaneous activity with NpHR at 18 hpf (A) and 20 hpf (B). Illumination at 593 nm at 19 mW/mm^2 is targeted successively to two regions outlined in yellow (A1, left), while calcium population activity is simultaneously recorded (A1, right) in the illuminated cells (red) and in the other ipsilateral cells (teal), and here displayed as normalized traces (standard deviation, s.d.) with regions indicated on y axis. At 18 hpf, application of yellow light to a single cell (during yellow highlight bar) inhibits only the illuminated cell, while other cells remain active (A1). Pooled results (n = 6 embryos) show inhibition during light-ON and activation at light-OFF to be limited to illuminated cells (red bars) (A2). (B) At 20 hpf, single-cell illumination has no effect on activity of either the illuminated or nonilluminated cells (n = 7 embryos). (C) At 20 hpf, illumination of one side of spinal cord in region spanning two somites (yellow outline in image, left) inhibits and rebound excites both the illuminated cells and other ipsilateral cells (n = 7 embryos). (D) Reduction of activity and rebound due to NpHR activation at 20 hpf are observed in cells that are both rostral and caudal to the region illuminated. (E) Control application of light aimed to the side of the cord but within the embryo (C1) does not perturb activity (n = 7 embryos), indicating that effect on unilluminated ipsilateral cells is not due to light scattering, though we acknowledge that light scattering may have different properties in this region. Rostral end points up in fluorescence images. Significance values from paired Student's t-test are $^{*}p < 0.05$ and $^{**}p < 0.01$. See also Figures S4 and S5.

Figure 5

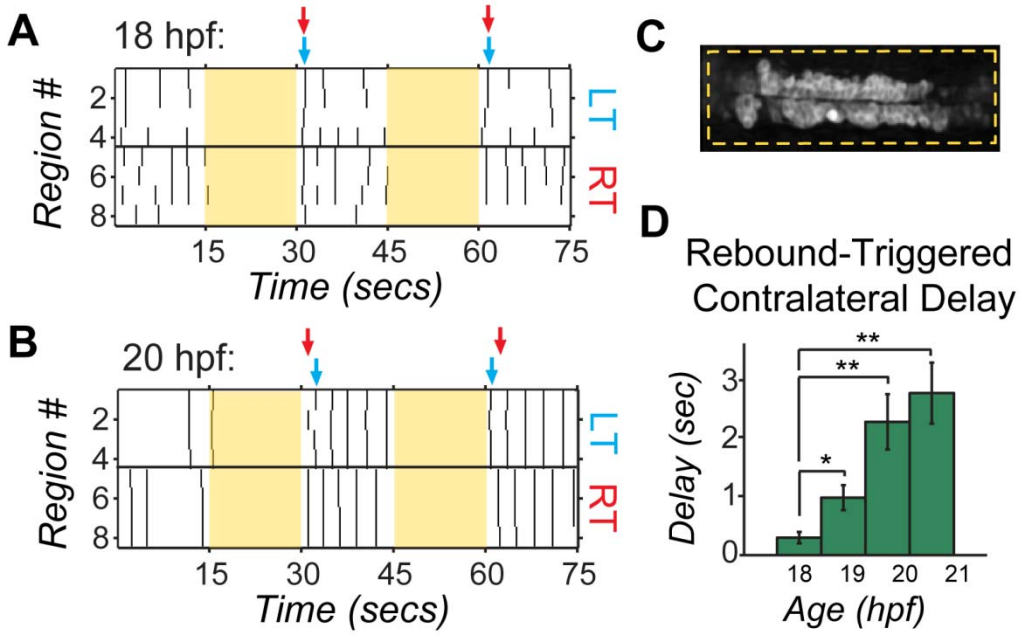

Figure 5. Bilateral Activation with NpHR Rebound Reveals Acquisition of Contralateral Antagonism during Development. Raster plots of spontaneous events of left and right cells in a single embryo at 18 hpf (A) and 20 hpf (B) during and following bilateral NpHR inhibition with 593 nm light (yellow bars) covering approximately four somites (C). (A) Bilateral activation following NpHR inhibition at 18 hpf results in near simultaneous activation of left (LT) and right (RT) cells following light offset. Arrows indicate the time when two or more cells participate in an event following light offset for one side of the cord (left side, blue; right side, red). (B) At 20 hpf, activation at light offset of bilateral illumination results in a burst of activity in which one side fires first, followed, after a delay, by firing on the other side and continuing in alternation of firing from side to side. In this example, the right side is active first in trial 1, but the left side is active first in the trial 2. (D) The delay following offset of bilateral illumination between synchronous events on the left and right sides of the cord (two or more cells participating) increases during development, suggesting an increase in left/right antagonism. n = 5 fish (four trials per fish per condition); $^{*}p < 0.05$; $^{**}p < 0.01$, paired Student's t test. See also Figure S5.

Figure 6

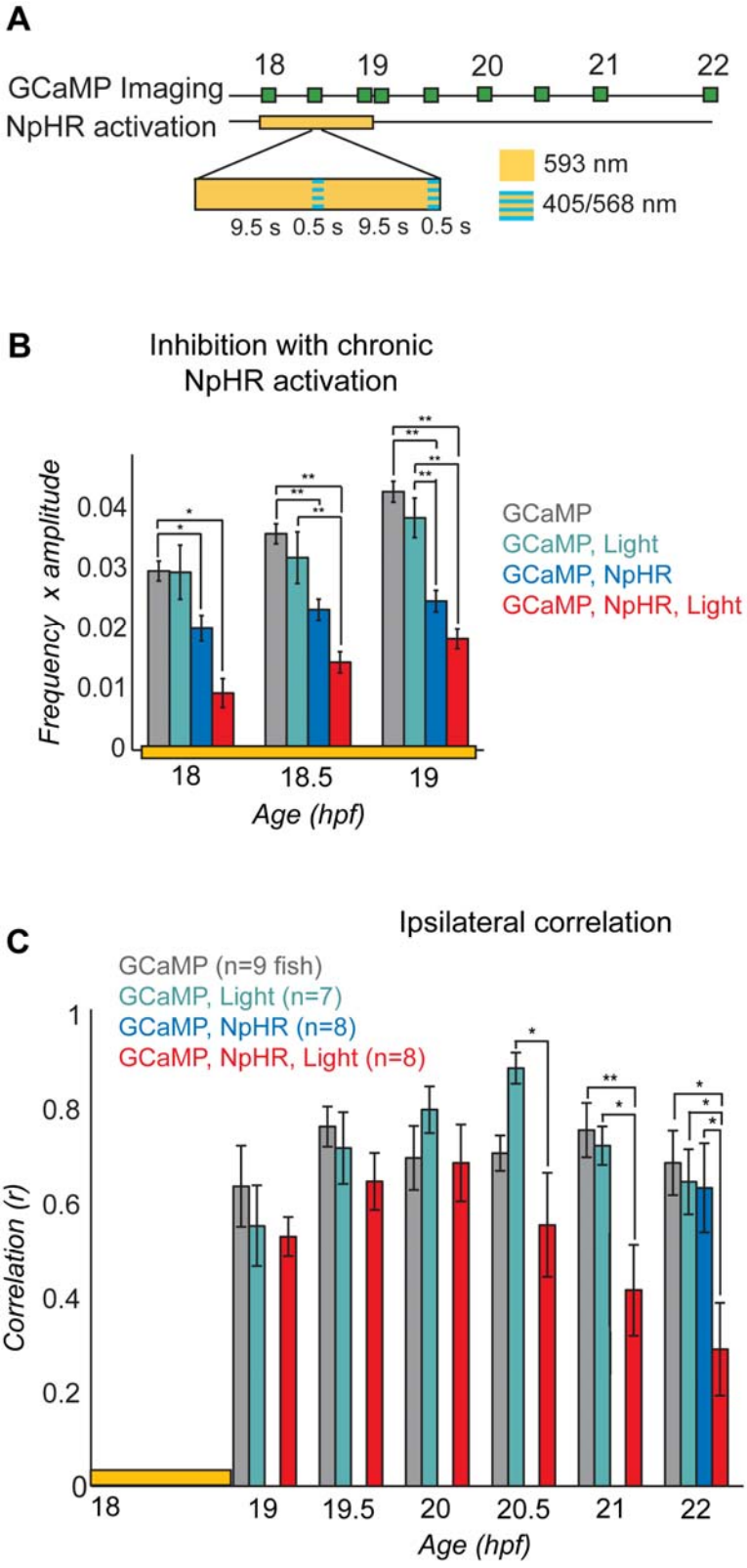
A
18
19
20
21
22
GCaMP Imaging
NpHR activation
593 nm
405/568 nm
9.5 s 0.5 s 9.5 s 0.5 s
B
Inhibition with chronic NpHR activation
Frequency x amplitude
0.04
0.03
0.02
0.01
0
18
18.5
19
Age (hpf)
GCaMP
GCaMP, Light
GCaMP, NpHR
GCaMP, NpHR, Light
C
Ipsilateral correlation
GCaMP (n=9 fish)
GCaMP, Light (n=7)
GCaMP, NpHR (n=8)
GCaMP, NpHR, Light (n=8)
Correlation (r)
1
0.8
0.6
0.4
0.2
0
18
19
19.5
20
20.5
21
22
Age (hpf)

Figure 6. Inhibition of Spontaneous Events with NpHR from 18 to 19 hpf Yields a Subsequent Decrease in Ipsilateral Correlation. (A) Experimental protocol for chronic inhibition experiments. GCaMP movies were acquired during the light manipulation (at 18, 18.5, and 19 hpf) with 488 nm light to determine the effectiveness of the light protocol and at half-hour to hour intervals thereafter (until 22 hpf) to assess subsequent changes in network dynamics. Stimulation of NpHR was performed from 18 to 19 hpf with continuous 593 nm light at 19 nW/mm^2 interspersed every 10 s with 500 msec long pulses of light simultaneously at two wavelengths: 405 nm to reduce desensitization of the NpHR and 568 nm to activate it. (B) The frequency of calcium events from 18 to 19 hpf was quantified for experimental fish expressing NpHR and receiving the yellow light protocol (GCaMP, NpHR, Light) as well as for three kinds of control fish: (1) NpHR-negative fish without yellow/blue light (GCaMP), (2) NpHR-negative fish with yellow/blue light (GCaMP, Light), and (3) NpHR-positive fish without yellow/blue light (GCaMP, NpHR). Means were calculated per cell, n = 13–385 cells per group. There was a significant effect of group at 18, 18.5, and 19 hpf (one-way ANOVA at each time point, $p < 0.05$), with greatest decreases in the experimental group (red bars; GCaMP, NpHR, Light). The reduction in activity in embryos that expressed NpHR but did not receive the light protocol can be attributed to the activation of NpHR by the 488 nm imaging light. (C) Average ipsilateral pairwise correlations measured for experimental fish (n = 8) and the three control groups (n = 7 to 9) in movies acquired after the termination of the yellow/blue light protocol reveal a decrease in correlated activity in the experimental fish (GCaMP, NpHR, Light) at later time points compared to all of the controls. There was no difference between groups at 19, 19.5, and 20 hpf (one-way ANOVA at each time point, $p > 0.05$), with significant differences at 20.5, 21, and 22 hpf (one-way ANOVA at each time point, $p < 0.05$). Note that to avoid activation of NpHR in controls without yellow/blue light protocol, GCaMP imaging in this group was only done at 22 hpf. Error bars = SEM. Asterisks in (B) and (C) mark pairwise significance from post hoc comparison with Bonferroni correction ($^{*}p < 0.05$; $^{**}p < 0.01$).

Figure 7

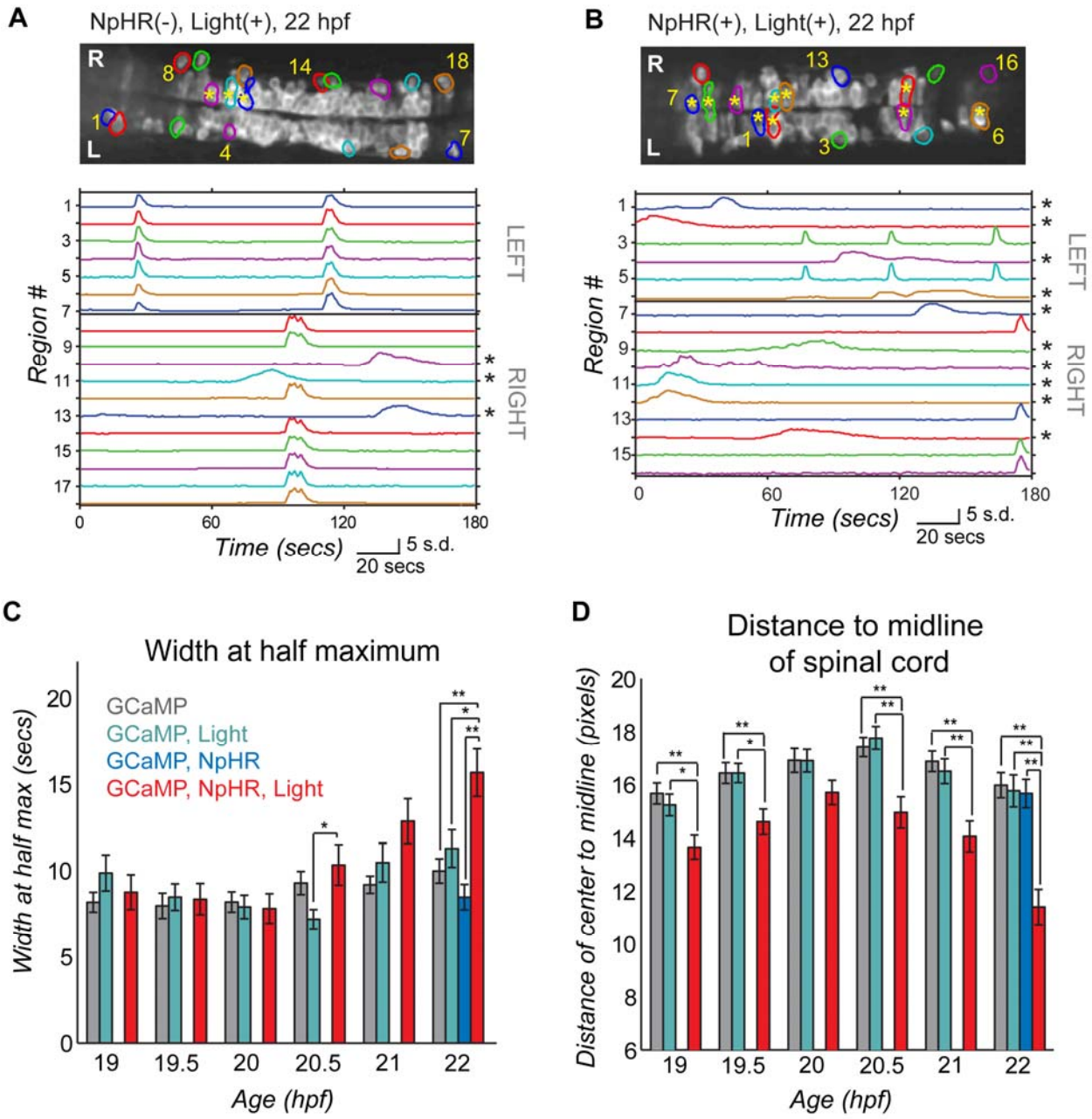
A
NpHR(-), Light(+), 22 hpf
R
L
Region #
LEFT
RIGHT
Time (secs)
5 s.d.
20 secs
B
NpHR(+), Light(+), 22 hpf
C
Width at half maximum
GCaMP
GCaMP, Light
GCaMP, NpHR
GCaMP, NpHR, Light
Width at half max (secs)
Age (hpf)
D
Distance to midline of spinal cord
Distance of center to midline (pixels)
Age (hpf)

Figure 7. Light Inhibition Decreases the Number of Cells Joining the Correlated Network. (A and B) Baseline GCaMP fluorescence images with active regions circled (top, rostral left) and associated normalized intensity traces (bottom; amplitude plots standard deviation, s.d.) in example control fish (without NpHR but illuminated with yellow/blue light protocol from 18–19 hpf) (A) and experimental fish (with NpHR and illuminated with yellow/blue light protocol from 18–19 hpf) (B) at 22 hpf. Asterisks mark cells with long-duration, uncorrelated events, which increase in number in the experimental fish (B, bottom) and can be seen to reside in the medial spinal cord (B, top). (C) Average event duration through development was quantified using width at half maximum for experimental fish expressing NpHR and receiving the yellow light protocol (GCaMP, NpHR, Light) and for the three sets of control fish: (1) lacking light and NpHR expression (GCaMP), (2) lacking NpHR expression (GCaMP, Light) or lacking light (GCaMP, NpHR). There was no difference between groups at 19, 19.5, 20, and 21 hpf (one-way ANOVA at each time point, $p > 0.05$), with significant differences at 20.5 and 22 hpf (one-way ANOVA at each time point, $p < 0.05$), when experimental fish showed increases in event duration. (D) The distance from the cell center to the midline of the cord for active cells is reduced significantly in the experimental (GCaMP, NpHR, Light) fish compared to the three controls at all ages tested except for 20 hpf (one-way ANOVA at each time point, $p < 0.05$). In (C) and (D), means were calculated per cell (72–137 cells per group). Error bars = SEM. Asterisks in (C) and (D) mark pairwise significance from post hoc comparison with Bonferroni correction ($^{*}p < 0.05$; $^{**}p < 0.01$). See also Figure S6.

REFERENCES

1. Blankenship, A.G. & Feller, M.B. Mechanisms underlying spontaneous patterned activity in developing neural circuits. *Nat. Rev. Neurosci* 11, 18-29 (2010).

2. Spitzer, N.C. Coincidence detection enhances appropriate wiring of the nervous system. *Proc. Natl. Acad. Sci. U.S.A* 101, 5311-5312 (2004).

3. Torborg, C.L. & Feller, M.B. Spontaneous patterned retinal activity and the refinement of retinal projections. *Prog. Neurobiol* 76, 213-235 (2005).

4. Gust, J., Wright, J.J., Pratt, E.B. & Bosma, M.M. Development of synchronized activity of cranial motor neurons in the segmented embryonic mouse hindbrain. *J. Physiol. (Lond.)* 550, 123-133 (2003).

5. Corlew, R., Bosma, M.M. & Moody, W.J. Spontaneous, synchronous electrical activity in neonatal mouse cortical neurones. *J. Physiol. (Lond.)* 560, 377-390 (2004).
6. Crépel, V. *et al.* A parturition-associated nonsynaptic coherent activity pattern in the developing hippocampus. *Neuron* 54, 105-120 (2007).

7. Gu, X., Olson, E.C. & Spitzer, N.C. Spontaneous neuronal calcium spikes and waves during early differentiation. *J. Neurosci* 14, 6325-6335 (1994).

8. Nakayama, K., Nishimaru, H. & Kudo, N. Basis of changes in left-right coordination of rhythmic motor activity during development in the rat spinal cord. *J. Neurosci* 22, 10388-10398 (2002).

9. Hanson, M.G. & Landmesser, L.T. Characterization of the circuits that generate spontaneous episodes of activity in the early embryonic mouse spinal cord. *J. Neurosci* 23, 587-600 (2003).

10. Delpy, A., Allain, A.-E., Meyrand, P. & Branchereau, P. NKCC1 cotransporter inactivation underlies embryonic development of chloride-mediated inhibition in mouse spinal motoneuron. *J. Physiol. (Lond.)* 586, 1059-1075 (2008).

11. Hanson, M.G., Milner, L.D. & Landmesser, L.T. Spontaneous rhythmic activity in early chick spinal cord influences distinct motor axon pathfinding decisions. *Brain Res Rev* 57, 77-85 (2008).

12. Gonzalez-Islas, C. & Wenner, P. Spontaneous network activity in the embryonic spinal cord regulates AMPAergic and GABAergic synaptic strength. *Neuron* 49, 563-575 (2006).

13. Myers, C.P. *et al.* Cholinergic input is required during embryonic development to mediate proper assembly of spinal locomotor circuits. *Neuron* 46, 37-49 (2005).

14. Grillner, S. Biological pattern generation: the cellular and computational logic of networks in motion. *Neuron* 52, 751-766 (2006).

15. Tian, L. *et al.* Imaging neural activity in worms, flies and mice with improved GCaMP calcium indicators. *Nat. Methods* 6, 875-881 (2009).

16. Muto, A. *et al.* Genetic visualization with an improved GCaMP calcium indicator reveals spatiotemporal activation of the spinal motor neurons in zebrafish. *Proc. Natl. Acad. Sci. U.S.A* 108, 5425-5430 (2011).

17. Higashijima, S.-ichi, Masino, M.A., Mandel, G. & Fetcho, J.R. Imaging neuronal activity during zebrafish behavior with a genetically encoded calcium indicator. *J. Neurophysiol* 90, 3986-3997 (2003).

18. Del Bene, F. *et al.* Filtering of Visual Information in the Tectum by an Identified Neural Circuit. *Science* 330, 669-673 (2010).

19. Zhang, F. *et al.* Multimodal fast optical interrogation of neural circuitry. *Nature* 446, 633-639 (2007).

20. Arrenberg, A.B., Del Bene, F. & Baier, H. Optical control of zebrafish behavior with halorhodopsin. *Proc. Natl. Acad. Sci. U.S.A* 106, 17968-17973 (2009).

21. Saint-Amant, L. & Drapeau, P. Synchronization of an embryonic network of identified spinal interneurons solely by electrical coupling. *Neuron* 31, 1035-1046 (2001).

22. Scott, E.K. *et al.* Targeting neural circuitry in zebrafish using GAL4 enhancer trapping. *Nat. Methods* 4, 323-326 (2007).

23. Wyart, C. *et al.* Optogenetic dissection of a behavioural module in the vertebrate spinal cord. *Nature* 461, 407-410 (2009).

24. Park, H.-C., Shin, J. & Appel, B. Spatial and temporal regulation of ventral spinal cord precursor specification by Hedgehog signaling. *Development* 131, 5959-5969 (2004).

25. Saint-Amant, L. & Drapeau, P. Time course of the development of motor behaviors in the zebrafish embryo. *J. Neurobiol* 37, 622-632 (1998).

26. Saint-Amant, L. & Drapeau, P. Motoneuron activity patterns related to the earliest behavior of the zebrafish embryo. *J. Neurosci* 20, 3964-3972 (2000).

27. Mukamel, E.A., Nimmerjahn, A. & Schnitzer, M.J. Automated analysis of cellular signals from large-scale calcium imaging data. *Neuron* 63, 747-760 (2009).

28. Masino, M.A. & Fetcho, J.R. Fictive swimming motor patterns in wild type and mutant larval zebrafish. *J. Neurophysiol* 93, 3177-3188 (2005).

29. Kimmel, C.B., Ballard, W.W., Kimmel, S.R., Ullmann, B. & Schilling, T.F. Stages of embryonic development of the zebrafish. *Dev. Dyn* 203, 253-310 (1995).

30. Bernhardt, R.R., Chitnis, A.B., Lindamer, L. & Kuwada, J.Y. Identification of spinal neurons in the embryonic and larval zebrafish. *J. Comp. Neurol* 302, 603-616 (1990).

31. Kuwada, J.Y. & Bernhardt, R.R. Axonal outgrowth by identified neurons in the spinal cord of zebrafish embryos. *Exp. Neurol* 109, 29-34 (1990).

32. Deliagina, T.G., Zelenin, P.V. & Orlovsky, G.N. Encoding and decoding of reticulospinal commands. *Brain Res. Brain Res. Rev* 40, 166-177 (2002).

33. Hegemann, P., Oesterhelt, D. & Bamberg, E. The transport activity of the light-driven chloride pump halorhodopsin is regulated by green and blue light. *Biochimica et Biophysica Acta (BBA) - Biomembranes* 819, 195-205 (1985).

34. Ren, J. & Greer, J.J. Ontogeny of rhythmic motor patterns generated in the embryonic rat spinal cord. *J. Neurophysiol* 89, 1187-1195 (2003).

35. O'Donovan, M., Ho, S. & Yee, W. Calcium imaging of rhythmic network activity in the developing spinal cord of the chick embryo. *J. Neurosci* 14, 6354-6369 (1994).

36. Ashworth, R. & Bolsover, S.R. Spontaneous activity-independent intracellular calcium signals in the developing spinal cord of the zebrafish embryo. *Brain Res. Dev. Brain Res* 139, 131-137 (2002).

37. Milner, L.D. & Landmesser, L.T. Cholinergic and GABAergic inputs drive patterned spontaneous motoneuron activity before target contact. *J. Neurosci* 19, 3007-3022 (1999).

38. Syed, M.M., Lee, S., Zheng, J. & Zhou, Z.J. Stage-dependent dynamics and modulation of spontaneous waves in the developing rabbit retina. *J. Physiol. (Lond.)* 560, 533-549 (2004).

39. Yuste, R., Peinado, A. & Katz, L.C. Neuronal domains in developing neocortex. *Science* 257, 665-669 (1992).

40. Downes, G.B. & Granato, M. Supraspinal input is dispensable to generate glycine-mediated locomotive behaviors in the zebrafish embryo. *J. Neurobiol* 66, 437-451 (2006).

41. Komuro, H. & Rakic, P. Intracellular Ca2+ fluctuations modulate the rate of neuronal migration. *Neuron* 17, 275-285 (1996).

42. Gu, X. & Spitzer, N.C. Distinct aspects of neuronal differentiation encoded by frequency of spontaneous Ca2+ transients. *Nature* 375, 784-787 (1995).

43. Desarmenien, M.G. & Spitzer, N.C. Role of calcium and protein kinase C in development of the delayed rectifier potassium current in Xenopus spinal neurons. *Neuron* 7, 797-805 (1991).

44. Crisp, S.J., Evers, J.F. & Bate, M. Endogenous patterns of activity are required for the maturation of a motor network. *J. Neurosci* 31, 10445-10450 (2011).

SUPPLEMENTAL INFORMATION

Supplemental Figure 1

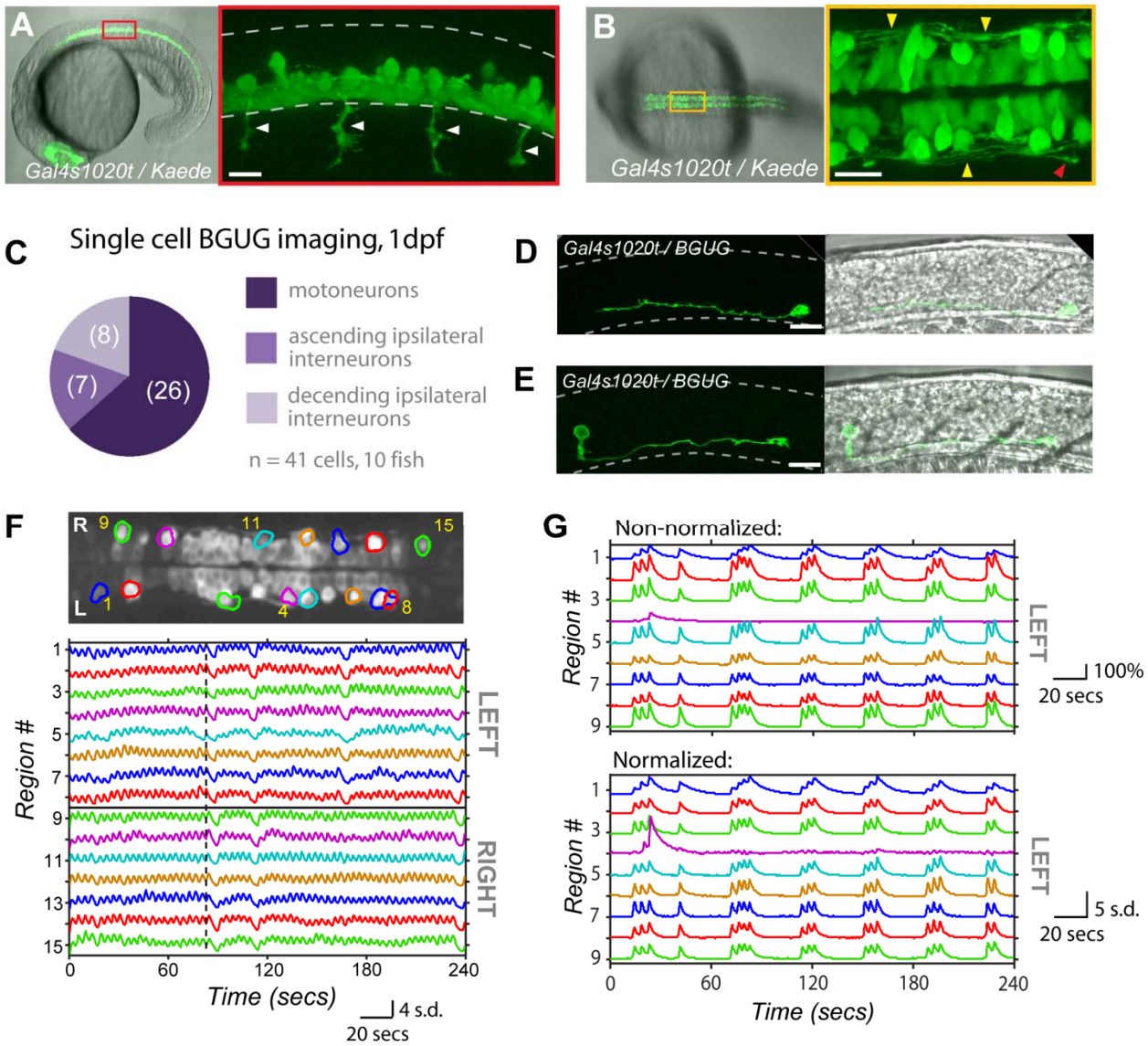

Supplemental Figure 1, related to Fig. 1. The *Gal4s1020t* line targets ventral spinal neurons of the motor system at 1 dpf which display locomotor-like patterns of activity. (A) Lateral view of *Gal4s1020t* expression pattern in a 20 hpf *Gal4s1020t*/*UAS:Kaede* embryo. (*left*) Low magnification showing entire embryo. (*right*) Zoomed view of red boxed area showing the ventral location of cell bodies and motoneuron axons (arrows) extending out of the cord. Low (B, *left*) and high magnification (*right*) dorsal views of 20 hpf *Gal4s1020t*/*UAS:Kaede* embryo show lateral processes (yellow arrows) with a descending growth cone in view (red arrow). (C-E) Using the BGUG transgenic line[1], we stochastically expressed GFP in 1-10% of the *Gal4s1020t* population to identify the morphology of cells targeted at 1 dpf. As at 5 dpf[2], GFP expression at 1 dpf was found in motoneurons (63%), whose axons can be seen in A (arrows), and ascending ipsilateral interneurons, presumed to be KA interneurons, (17%), an example of which can be seen in (D) at 1 dpf. We also found expression in descending ipsilateral interneurons, presumed to be VeLDs (20%), an example of which (E) shows their characteristic large cell body located in the middle of the cord along the dorsal/ventral axis in a 1 dpf embryo. (F) GCaMP3 activity in an example embryo at 20.5 hpf. (*top*) Dorsal view of GCaMP3 baseline fluorescence with active regions circled (rostral left; imaged area somites 4-8). (*bottom*) Normalized intensity traces for active regions (identified on the y-axis) for the left and right sides of the cord. This fish shows very short periods of correlated quiescence between the left and right sides, with long sustained bursts alternating between the left and right sides. Dotted vertical line emphasizes alternation, passing through event peaks for left-sided cells and troughs for the right. (G) Shows nine cells from Fig. 1 before normalization (*top*), where traces are plotted as $\Delta F/F$ (%), and after normalization by zscore (*bottom*), where traces are plotted as standard deviation (s.d.) for comparison. Scale bar=20 μm for B, D, E and F. Dotted lines in A, C and D outline approximate border of spinal cord. Rostral to left.

Supplemental Figure 2

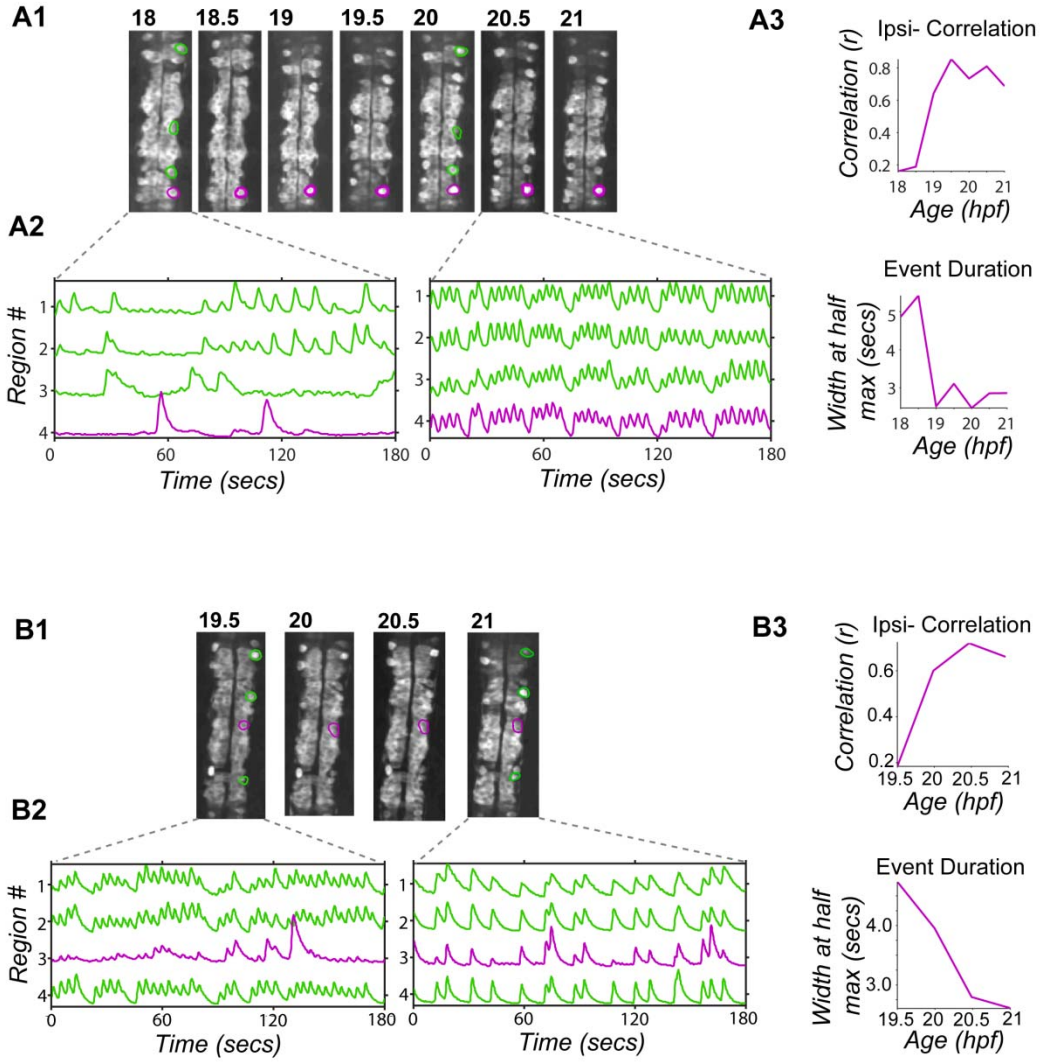

Supplemental Figure 2, related to Fig. 2. Early and late onset neurons show increases in correlation and decreases in event duration through development. Single cells with detected activity onset at 18 hpf (A) and 19.5 hpf (B) tracked through consecutive time lapse movies until 21 hpf. (*1*) Baseline GCaMP3 fluorescence with tracked cells (purple) and other active ipsilateral cells (green) circled. (*2*) Normalized intensity traces (plotted as standard deviation) for tracked cells (purple) and other active ipsilateral cells (green) showing uncorrelated activity at early time points and correlated activity at later time points. (*3*) Correlation of tracked cells versus other ipsilateral cells increased through development for both example cells, as seen in the pooled population data (Fig. 2C). Event duration was calculated as the width at half maximum for the fitted event kernel and decreased for both examples. Rostral, up.

Supplemental Figure 3

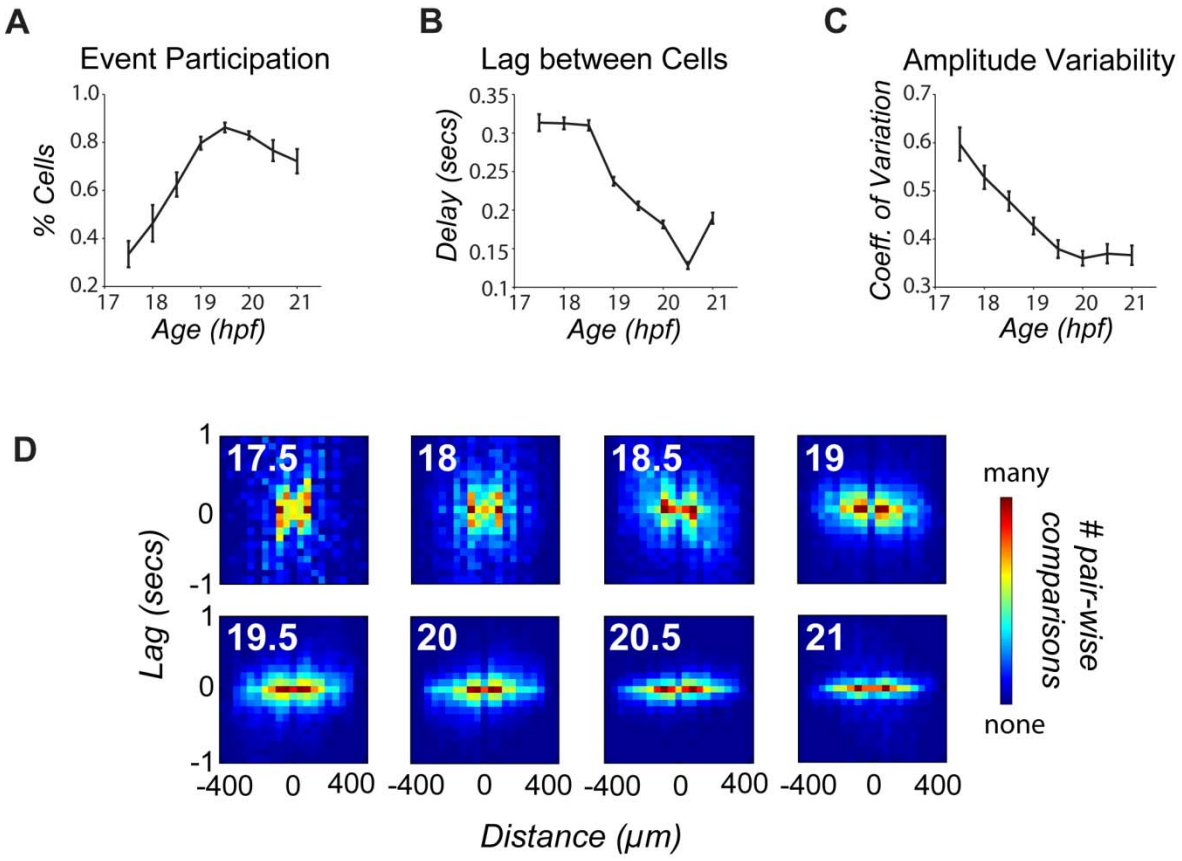

Supplemental Figure 3, related to Fig. 3. Synchronized groups contain more cells and are more accurately time-locked at later stages in development. (A) The percentage of active ipsilateral cells in the field of view participating in a synchronous event (defined as having a calcium event within 1 second of an event peak, see *Experimental Procedures*) increases until 19.5 hpf and was significantly different between 18 and 20 hpf (18 hpf, 46 ± 7.6%; 20 hpf, 83 ± 1.7%; P = 0.002, paired Student's *t* test; n = 9 fish). (B) For cells participating in synchronous events, the temporal lag between event start times between cells decreases until 20.5 hpf, with significant differences between 18 and 20 hpf (18 hpf, 0.31 ± 0.15 sec, n = 385 events; 20 hpf, 0.18 ± 0.09 sec, n = 360 events; $P < 10^{-10}$, unpaired Student's *t* test). (C) The variability of amplitude, calculated as the coefficient of variation within events from a given cell, decreases from 17.5 to 20 hpf, and was significantly different between 18 and 20 hpf (18 hpf, coefficient of variation = 0.528 ± 0.024, n = 121 cells; 20 hpf, coefficient of variation = 0.360 ± 0.015, n = 189 cells, $P < 10^{-8}$, unpaired Student's *t* test). (D) Two-dimensional histograms plotting the relative rostral-caudal pair-wise distance between cells in correlated groups against the temporal lag between the same cells (n = 9 fish for 18-21 hpf; n = 4 fish at 17.5 hpf). Individual pixels represent the number of cell pairs (with high values in red) that were part of a correlated group and had a given distance between them (x-axis) and temporal lag (y-axis). Correlated groups were defined as two or more cells having pair-wise correlation coefficients greater than 0.5. Histogram data was normalized within each age group and ranged from zero to between 36 and 878 pair-wise comparisons. Error bars=s.e.m.

Supplemental Figure 4

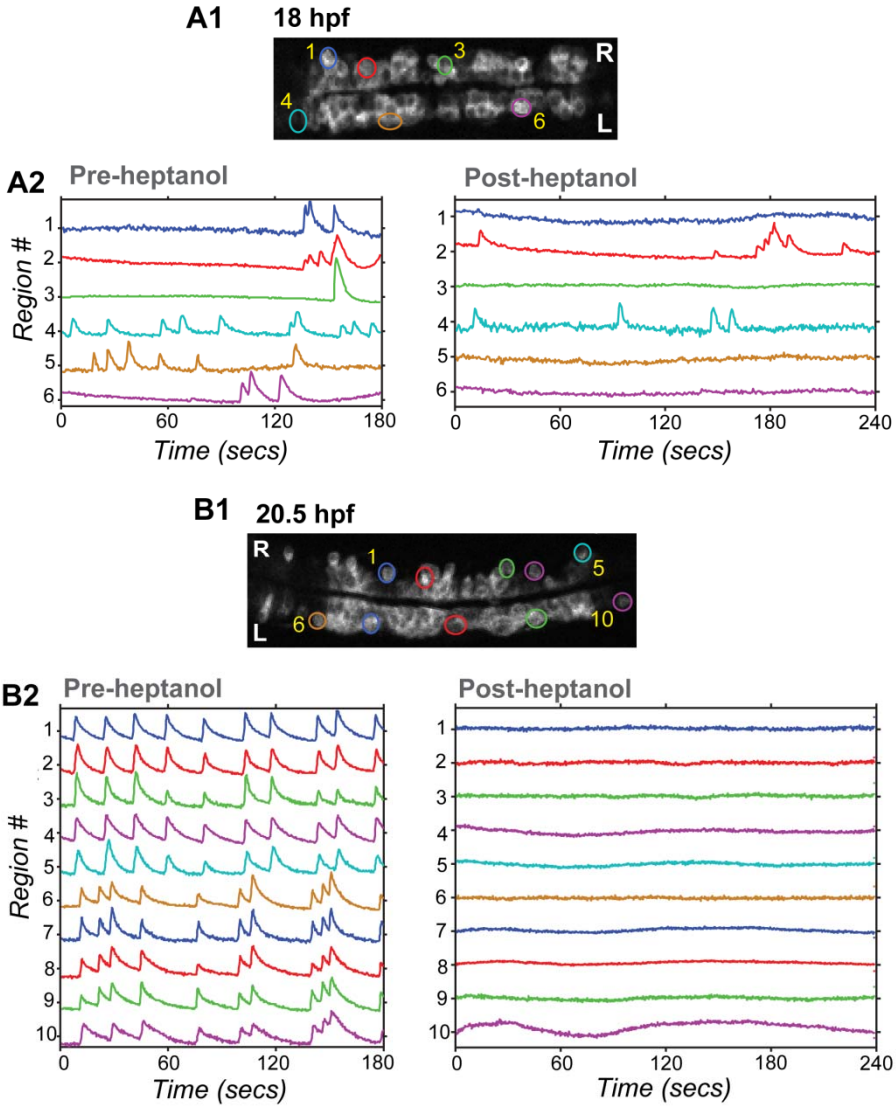

Supplemental Figure 4, related to Fig. 4. Gap junction blocker heptanol has little effect on substantial fraction of cells in younger embryos, but profoundly blocks activity in older embryos. GCaMP3 population activity before and after heptanol treatment in an 18 (A) and 20.5 (B) hpf embryo. (1) Baseline GCaMP3 fluorescence images with cells active in pre-heptanol movies circled. (2) GCaMP3 intensity traces ($\Delta F/F$) for these regions before (*left*) and after (*right*) 2mM heptanol treatment shows that some cells remained spontaneously active during gap junction block in the younger embryo (A2; cells 2 and 4), but no cells were active after heptanol treatment in the older embryo (B2).

Supplemental Figure 5

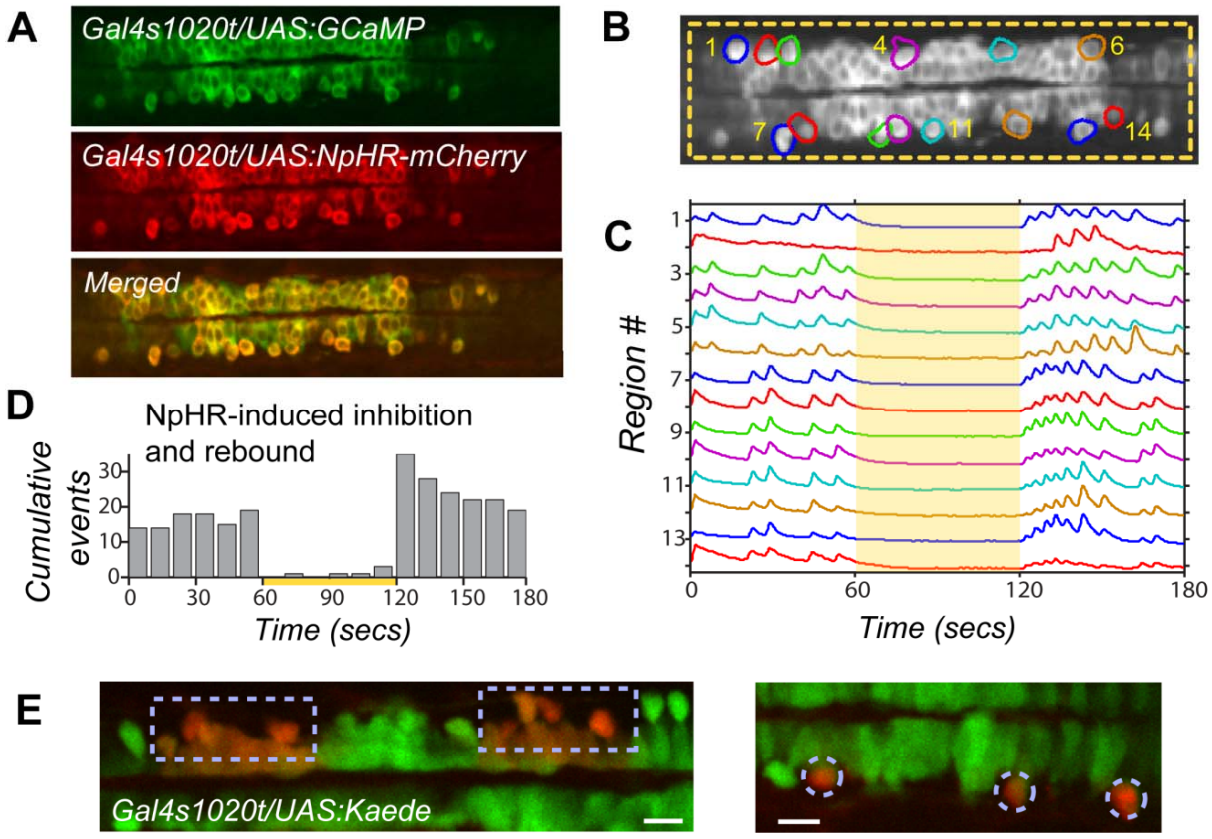

Supplemental Figure 5, related to Figs. 4 and 5. Activation of the light-driven chloride pump Halorhodopsin robustly inhibits spontaneous events and causes rebound excitation. (A) *Gal4s1020t/ UAS:GCaMP3/ UAS:NpHR-mCherry* fish express GCaMP3 and NpHR in the same spinal neurons. (B) Full field illumination (yellow dashed box) with 19mW/mm^2 593nm light is targeted to NpHR-expressing spinal neurons while simultaneously imaging population activity with GCaMP3. (C) Spontaneous events in active regions, plotted as standard deviation, are eliminated during application of yellow light (yellow bar) in a 19 hpf fish. (D) Tallied events across several fish (n=6) shows effective inhibition when yellow light is on (yellow bar) and there is an increase in activity above baseline at light offset. (E) Accurate light targeting with the digital micro-mirror device is confirmed with the restricted photo-conversion of Kaede. Illumination with blue light (380nm) switches the fluorescence emission of Kaede from green to red[22]. Cells within illuminated region (boxed areas on left, single cells circled on right) convert to red while adjacent cells remain green. Though the wavelength used for NpHR activation is longer (593nm) and may scatter a little differently, we used a similar light power (15.2mW/mm^2 for Kaede; 19mW/mm^2 for NpHR) and exposure time (1 min). Scale bars=20μm.

Supplemental Figure 6

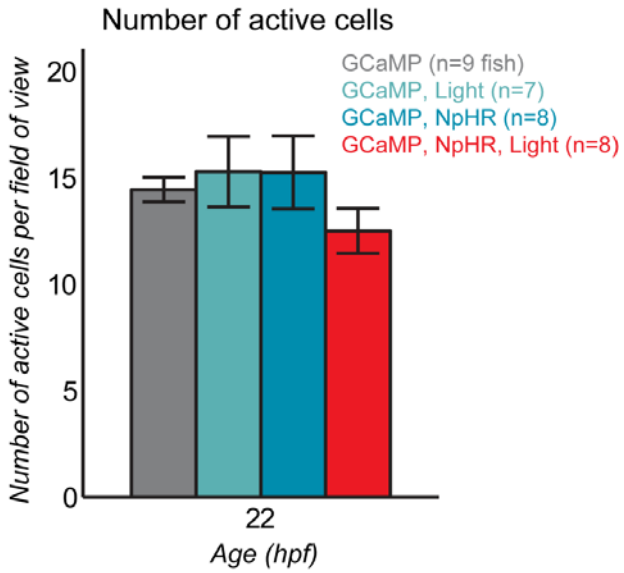

Supplemental Figure 6, related to Fig. 7. Experimental fish expressing NpHR and receiving one hour light manipulation have the same number of spontaneously active cells as control groups. The total number of active cells in the field of view during a 3 minute movies was tallied for experimental fish (GCaMP, NpHR, Light) and the three control groups: i) NpHR-negative fish without yellow/blue light (GCaMP), ii) NpHR-negative fish with yellow/blue light (GCaMP, Light), and iii) NpHR-positive fish without yellow/blue light (GCaMP, NpHR). There was no significant difference between the four groups at 22 hpf (one-way ANOVA, P=0.40), though we did see a slight reduction in the number of cells in GCaMP, NpHR, Light fish. This reduction could be accounted for by the relatively lower frequency of long duration, uncorrelated events, making cells with these events less probable to detect. Bars=s.e.m.

Supplemental Experimental Procedures

Embryo Preparation and GCaMP imaging

Embryos of the Tubingen genetic background were raised in E3 embryo medium at 28.5ºC until 60% epiboly, and at 25ºC thereafter to delay development for experimentation. GCaMP positive progeny of *UAS:GCaMP3* and *Gal4s1020t* fish were mounted in 1.4% agar and paralyzed with injections of 750µg/ml ∝-bungarotoxin (Invitrogen) into the tail once before imaging (at 17-17.5 hpf). Embryos were aged by somite counting and were in a 28.5ºC heated chamber for time-lapse experiments (including NpHR rebound experiments, Fig. 5) so that they could develop at a normal rate. NpHR functional connectivity experiments (Fig. 4, 5) were performed at room temperature. Morphology images of *UAS:Kaede/ Gal4s1020t* fish were taken on a Zeiss 510 Meta confocal microscope. Functional imaging was performed on a 3i Marianas system (Intelligent Imaging Innovations) with a spinning disk confocal (Yokagawa) mounted on a Zeiss microscope and using a 488nm laser and 20x water-immersion objective (numerical aperture = 1.0). For time-lapse experiments, 4 minute movies were acquired every half hour at 4 Hz. Imaging was acquired at 2 Hz for all NpHR experiments to reduce potential activation of NpHR by imaging light.

Photomanipulation of activity

Photostimulation of NpHR and Kaede was accomplished through a digital micro-mirror device (DMD) illumination system (Photonic Instruments) coupled to the imaging microscope. Activating light was provided by a Xenon lamp (Sutter Instruments) filtered to 573-613nm and was 19mW/mm^2 at the sample. Spatial and temporal control of the yellow light was achieved through integration software (Intelligent Imaging Innovations). NpHR experiments were performed on *UAS:NpHR-mCherry/ UAS:GCaMP3/ Gal4s1020t* fish displaying both red and green fluorescence. For functional connectivity experiments (Fig. 4), the experimental protocol consisted of 1 minute NpHR activation with yellow light to the targeted region (e.g. single cell, two somite section or two somite-sized light control off of cord) followed by 1 minute of rest while calcium activity was simultaneously imaged at 2 Hz. Experimental epochs were preceded and followed by 2 minute baseline periods for frequency normalization of individual cells. Single cell manipulations were restricted to CaP primary motoneurons for consistency. For bilateral rebound excitation experiments (Fig. 5), light was applied in 15 second intervals with 15 seconds of rest in between and repeated four times per embryo per time point. For chronic manipulation of activity (Fig. 6A), 9.5 seconds of 19mW/mm^2 593 nm light alternated with 500 msec of yellow/blue light using a double bandpass filter for 410 nm and 568 nm to provide continuous yellow light illumination and pulses of blue light for re-sensitization of NpHR. GCaMP3 movies were taken during light manipulation to test effectiveness of inhibition.

Analysis of calcium imaging movies

All analysis for time-lapse and NpHR experiments was performed using Matlab (Mathworks).

ROI and time course extraction: Drift during image acquisition was corrected using the DIPimage package (www.diplib.org) for all time-lapse and NpHR movies. The CellSort

toolbox[3] was used to automatically detect active cell bodies, identified as contiguous pixel islands, each with a distinctive time course of response. ROIs that were redundant (i.e. corresponding to the same cell) were manually merged; ROIs corresponding to axons or moving cells were manually removed. Traces plotted in Figs. 1, 4 and 7 and Supplemental Figs. 1F, 2 and 5 were normalized by taking the zscore of the $\Delta F/F$ values (plots display these standard deviation values) to best visualize the event contours in all cells. All other traces shown are $\Delta F/F$. See *Supplemental Fig. 1G* for a comparison of traces pre- and post-normalization.

Event detection and characterization: Each intensity trace was scanned for instances when the rise in fluorescence over a 1-second interval exceeded an empirically determined threshold. The resulting estimated timing and amplitudes of the events were used to initialize a parameterized model of the trace, which was subsequently refined using a nonlinear, least-squares fitting algorithm (*lsqnonlin*, Matlab). The model consisted of three components: a cubic spline that accounted for any slow drifts in baseline; a double exponential kernel to match each cell's unique, stereotyped calcium transient (e.g. Fig. 1B, E); and the timing and amplitude of each event detected as described above. The convergence of the resulting fits was manually verified. Events were identified as spurious if the estimated magnitude was exceeded by its confidence interval. The amplitudes and timings of all remaining events encoded the time course of a cell's activity (e.g. Fig 1C, F) and were used for all subsequent analysis.

Characterization of synchronous events: To identify time-coupled events in a given movie, binary traces encoding the occurrence of events in all cells were filtered with a 2-second wide Gaussian window and summed. Peaks in the resulting trace that exceeded an empirically-determined threshold were marked as "synchronous" events. Cells were identified as participating in an event when they were active within 1 second of a peak (in other words, synchrony allowed for a little temporal jitter between cells). For these time-coupled cells, lag times between when a particular cell was active and the event peak were determined. The response amplitudes of *n* cells during *m* population events (0 if a cell was inactive during the event) were compiled into an *n* x *m* matrix. This was used to calculate an *n* x *n* correlation matrix, resulting in correlations across events (Figs. 2C, 3, 6C and for *Supplemental Figs. 2 and 3*). In contrast, the correlations presented in Fig. 2A, B were calculated for the entire activity trace, using the idealized traces filtered with a 1-second wide Gaussian. To identify correlated ensembles of cells within a network for Fig. 3 and *Supplemental Fig. 3*, cell pairs were marked as belonging to the same group if their correlation across synchronous events was greater than 0.2 for Fig. 3 or 0.5 for *Supplemental Fig. 3*. Separate groups were then identified using the *components* function within the Matlab mesh partitioning toolbox[4].

NpHR experiments: For the analysis of NpHR functional connectivity experiments, frequency in the first 30 seconds after yellow light on- and off was compared to average frequency for pre- and post-experiment baseline epochs in paired Student's *t* tests. For NpHR rebound bilateral excitation experiments, synchronous events were determined as described above and left/right lag was determined by calculating the temporal difference between the first synchronous event (two or more cells) on the left versus the

right side of the cord after light offset. Ipsilateral correlation for Fig. 6C was calculated as in Fig. 2C.

Statistical analysis: For chronic Halorhodopsin experiments, the effect of group (GCaMP, GCaMP/Light, GCaMP/NpHR, and GCaMP,NpHR,Light) on frequency x amplitude (Fig. 6B), mean correlation (Fig. 6C), mean event width (Fig. 7C), mean cell distance to midline (Fig. 7D), and number of active cells (*Supplemental Fig. 6*) was tested with one-way ANOVAs at each time point. Time points with significant effects of group ($p<0.05$) were further analyzed with a post-hoc comparison test with Bonferroni correction (at alpha = 0.05 and 0.01) to identify which group pairs were significantly different from one another. For all other analyses, statistical significance between mean data was calculated using the unpaired and paired two-tailed Student's *t* test.

Supplemental References

1. Scott, E.K. *et al.* (2007) Targeting neural circuitry in zebrafish using GAL4 enhancer trapping. *Nat. Methods*, 4:323-326.

2. Wyart, C. et al. (2009) Optogenetic dissection of a behavioural module in the vertebrate spinal cord. *Nature,* 461:407-410.

3. Mukamel, E.A., Nimmerjahn, A. & Schnitzer, M.J. (2009) Automated analysis of cellular signals from large-scale calcium imaging data. *Neuron,* 63:747-760.

4. Gilbert, J., Miller, G. & Shang-Hua Teng. (1995) Geometric mesh partitioning: implementation and experiments. *Parallel Processing Symposium, 1995. Proceedings., 9th International* 418-427.